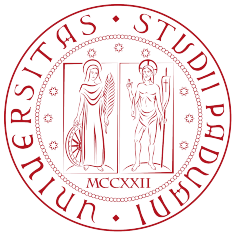

Università degli studi di Padova

Dipartimento di Fisica e Astronomia "Galileo Galilei"
Master Degree in Astrophysics and Cosmology

Final Dissertation

Modeling the pulsating emission for ULXs

Candidate:
Silvia Conforti
Matricola 2023858

Thesis supervisor:
Prof. Roberto Turolla

Thesis co-supervisor:
Dott. Roberto Taverna

Academic Year 2021-2022

To that little girl of twelve years old

Abstract

Ultra-luminous X-ray sources, aka ULXs, are off-nuclear, extragalactic sources that shine in the X-rays with luminosities of $L_X \geq 10^{39}\mathrm{erg\,s^{-1}}$. The huge energy output together with the X-ray variability suggest that ULXs are binary systems with a donor star transferring mass onto a compact object. ULXs luminosities far exceed the Eddington limit for a stellar-mass object, provided that the emission is assumed to be isotropic. This led to believe that these sources may host a black hole: either intermediate-mass black holes (IMBHs), or, if some degree of anisotropy is present in the emitted radiation, stellar-mass black holes (SMBHs). In 2014, observational evidences were found for pulsations in an ULX, revealing the existence of a new class of objects, dubbed Pulsating ULXs or PULXSs. Pulsations clearly point towards a the presence of a neutron star. The discovery of PULXs made the issue of how a super-Eddington flux may be produced even more irksome, since NS masses should not exceed ~ 2 solar masses. While invoking anisotropic emission is still an option, a further explanation may be provided by the presence of strong magnetic fields ($B \sim 10^{14}$G). In this thesis we discuss an emission model for PULXs, based on the effects of strong magnetic fields, which can account for their high luminosities. We focus on the modeling of the accretion disk and the accretion column close to the surface of the neutron star. The starting point is the commonly accepted picture according to which the accretion disk is truncated far from the star, due to the interaction between the disk itself and the magnetic field, and matter is then transported inwards along the field lines towards the poles, where a radiative shock and an accretion column are formed. Here the effects of the strong magnetic field on the electron scattering cross section starts to become important. In this thesis we built up on such a model, producing synthetic spectra and pulse profiles. A preliminary comparison with the observations of two PULXs show that indeed some observed features, like the increase of the pulsed fraction with energy, are indeed reproduced by the model.

ACKNOWLEDGEMENTS

I would like to express my gratitude to my supervisor Prof. Roberto Turolla, and to my co-supervisor Dr. Roberto Taverna, for their assistance at every stage of the thesis, through their detailed comments and suggestions.

CONTENTS

LIST OF FIGURES

INTRODUCTION

ULXs are ultra-luminous X-ray sources discovered for the first time in the 80s, by the Einstein X-ray Observatory, in external galaxies. One of the most distinctive features for these sources is the high X-ray luminosity, which can reach values of $L \sim 10^{41}$erg s^{-1}, far exceeding the Eddington limit for a solar mass object.

From an observational standpoint, ULXs are characterized by: an higher occurrence in star-forming galaxies [Swartz et al.(2004)], a sort of cut-off in the spectra for energies in the 2-10 keV range, suggesting a two-component spectral model (blackbody emission from an accretion disk, and a power-law probably due to a corona), and spectral variability at different epochs.

At the beginning the hypotheses on their nature were various [Kaaret et al.(2001)], since their luminosities were such that they resulted to be too bright with respect to some classes of X-ray sources, and too weak for others. However, the large amount of energy emitted, and the variability in the X-rays luminosity, led to believe that they are binary systems composed by an evolved star (donor star) which transfers material onto a compact object. X-ray binaries fall into three categories, according to the type of compact object they host: those containing a white dwarf (WD), a neutron star (NS), and a black hole (BH). Assuming isotropic emission, and hydrostatic equilibrium, the maximum luminosity of a star (Eddington luminosity) depends on the mass, so white dwarfs and neutron stars were excluded as possible powerhouse for these sources, since their mass cannot exceed $\sim 1.4 M_\odot$ for WDs and $\sim 2 M_\odot$ for NSs.

For some time it was believed that ULXs are powered by black holes of intermediate mass (IMBHs) with masses larger than $100 M_\odot$ [Makishima et al.(2000)]. In fact, the maximum X-ray luminosity which is possible for this class of objects exceeds by some orders of magnitude the observed one, and accretion proceeds at a sub-Eddington rate. Besides, It was also proposed that ULXs may contain a stellar mass BH (SMBH). If this would be the case, however, accretion should proceed at a super-Eddington rate and emission has to be beamed to match the observed luminosity ([Fabrika & Mescheryakov(2001)], [King et al.(2001)], [Poutanen et al.(2007)]).

This picture was soon revolutionized when in 2014 pulsations were discovered in the emission of an ULX in the M82 galaxy, M82 X-2 [Bachetti et al.(2014)]. Given this observation, the most reliable hypothesis in order to explain pulsations was that indeed ULXs could be powered by even neutron stars. The discovery of the first pulsating ULX was soon followed by many others ([Fürst et al.(2016)], [Israel et al.(2017)], [Castillo et al.(2020)], [Carpano et al.(2018)],

[Sathyaprakash et al.(2019)]). It was then clear that ULXs with not negligible pulsations should be part of a stand-alone sub-class of sources, that were dubbed as pulsating ultra-luminous X-ray sources (PULXs).

Despite the fact the association of PULXs with neutron stars appears quite straightforward, explaining how neutron stars can emit such a huge amount of energy remains an open problem, given their low Eddington luminosity.

In 1976, even before the discovery of PULXs, Basko & Sunyaev presented a model for accretion onto magnetized neutron stars, including for the first time the formation of an accretion column on the magnetic poles of the star [Basko & Sunyaev(1976)]. This model for the column was somewhat simplistic, and did not take into account the effects of the magnetic field. Later on, Lyubarskii & Sunyaev, in 1988, discussed again the same but better investigating the shape and properties of the column [Lyubarskii & Syunyaev(1988)]. Actually, the most updated model ([Mushtukov et al.(2015)], [Brice et al.(2021)], includes the description of all the accretion processes around a neutron star, starting from the formation of the disk, up to the formation of a radiative shock and an accretion column above the star surface, considering also the effects of the strong NS magnetic field on such a column. The model predicts that the magnetic field is able to drastically reduce the opacities inside the accretion column for photons polarized perpendicularly to the magnetic field direction, increasing in this way the flux of radiation escaping from the sides of the column. Such a scenario could indeed justify the large observed luminosities from these sources.

In the present work we illustrate a simplified model (based on those discussed in the literature) to reproduce the X-ray emission in PULXs, in terms of thermal emission from the accretion disk and the accretion envelope, which is shaped like a torus limited by the magnetic field lines extending up to the magnetospheric radius. To this aim, we set up two different numerical codes. This in order to calculate the flux of photons arriving from the part in view of the system as a function of both the photon energy and the star rotational phase, so that to construct spectra and light curves in different energy bands. Finally, our numerical results have been confronted with observational data for the PULXs, to check the operation of the codes and probe if the model can be applied to real cases.

We start by introducing the physics of the accretion process around compact objects in chapter 1; then we present the observational properties of ULXs, with particular attention to the discovery of the six PULXs in chapter 2; in chapter 3 we describe the basics theoretical concepts of the accretion onto neutron stars; in chapter 4 we describe the codes; numerical results are presented in chapter 5; we finally present our conclusions in chapter 6.

CHAPTER

ONE

BASICS OF ACCRETION ONTO COMPACT OBJECTS

Some of the most interesting sources in the Universe are those which emit in the X-rays. There are several types of X-ray sources, for example black holes in AGN (active galactic nuclei), supernova remnants, galaxy clusters, compact objects in binary systems: white dwarfs, neutron stars and black holes, and also isolated compact objects (like some NSs and WDs). In particular, for binary systems powered by compact objects, with luminosities higher than 10^{39} erg s^{-1}, we talk about ULXs, instead, for those which present a periodic emission PULXs . Their common peculiarity is, in fact, the very high luminosity in the X-rays, which can exceed values typical for a $10M_{\odot}$ black hole. This is possible thanks to the accretion process around such sources. This thesis focuses primarily on pulsating ULXs, those powered by neutron stars. Thus, we will start to discuss accretion in binary systems, focusing then on accretion onto magnetized neutron stars.

1.1 Accretion mechanism

As already mentioned, ULXs (and PULXs) are X-ray sources powered by accretion onto a compact object in a binary system, due to the transfer of matter from an evolved massive companion, the *donor star*, towards the accretor, the compact object itself.

There exist two circumstances in which there could be transfer of matter between the two components at a certain evolutionary stage:

1. when the donor star may increase in radius to the point at which the gravitational pull of the companion can remove the external layers of its envelope. This first scenario is called *Roche lobe overflow*.

2. when the donor star starts to eject much of its mass in the form of a stellar wind, and part of this material can be captured gravitationally by the companion. This is the case of *stellar wind accretion*.

Between the two scenarios, we will discuss better the first, since it is the most efficient.

1.1.1 Roche lobe overflow in binary systems

Let us consider a test particle that moves in the gravitational field of a binary system, composed by the donor star with mass M_2, and the compact one with mass M_1 (the gas particle belongs to the donor star), both the masses rotate around the center of mass. Since the distances inside the system are greater than the dimensions of bodies, they can be treated as point-like masses.

This is basically a three body problem, known properly as *Roche problem*. To solve it and understand the transfer mechanism, we start from the Euler equation for the test mass; it is convenient to do so in a frame which is co-rotating with the two stars and centered in the center of mass. The Euler equation would be the following:

$$\frac{\partial \vec{v}}{\partial t} + (\vec{v} \cdot \vec{\nabla})\vec{v} = -\frac{\vec{\nabla} P}{\rho} - 2\vec{\omega} \times \vec{v} - \vec{\omega} \times (\vec{\omega} \times \vec{r}) - \vec{\nabla}\phi_G \tag{1.1}$$

The left hand side term of the (1.1) is the total derivative of the velocity (dv/dt), on the right hand side there are: the pressure gradient, the Coriolis term, the Centrifugal term, and finally the gradient of the gravitational potential of the system. The terms for the Coriolis and the Centrifugal force, which are fictitious forces, are there since we are doing calculations in a frame that co-rotate with the system.

Since the centrifugal force admits a potential, we can first define that, and then a unique potential as follows:

$$\phi_C = -\frac{1}{2}(\vec{\omega} \times \vec{r})^2 \tag{1.2}$$

$$\phi_R = \phi_G + \phi_C \tag{1.3}$$

where ϕ_C and ϕ_G are the centrifugal and gravitational potentials, respectively. ϕ_R is called *Roche potential*. The locus of points in which that potential is constant is called *equipotential surface*, and it is the surface on which the gravitational force excerted by the two masses (M_1 and M_2), on the test mass, is balanced by the centrifugal force (see figure 1.1). The points in which holds $\vec{\nabla}\phi_R = 0$ are called *Lagrange points*.

In order to understand how the mass transfer is triggered, one can take a star which is evolving slowly (M_2), so that its surface can be seen to be at rest, in first approximation. Let us now consider the Euler equation for a particle on the star surface, taking into account that for the previous assumption the Coriolis term is null:

$$0 = -\frac{1}{\rho}\vec{\nabla} P - \vec{\nabla}\phi_R, \tag{1.4}$$

then considering also the fact that the surface of the star is defined by the condition

$$\vec{\nabla} P = 0, \tag{1.5}$$

and substituting this last into the (1.4), the star surface turns out to be an equipotential surface.

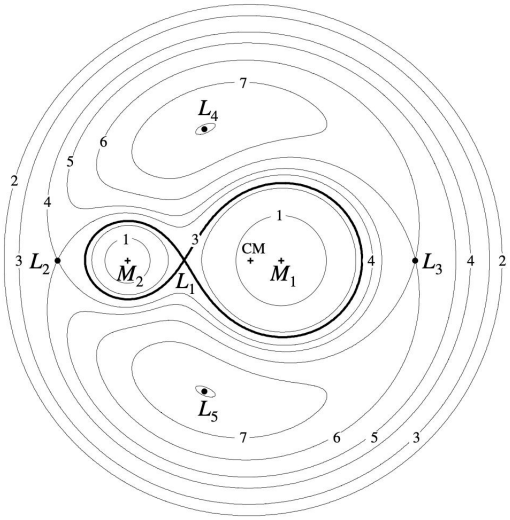

(a)

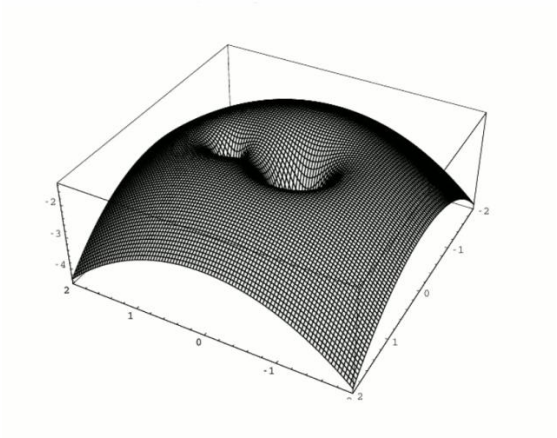

(b)

Figure 1.1: Equipotential surfaces. The panel (a) represents the projections of the equipotential surfaces of the Roche potential on the plane orthogonal to ω (angular velocity of the test mass), for a binary system with mass ratio $q = M_2/M_1 = 0.25$. Points L_1, L_2, L_3, L_4 and L_5 are called the *Lagrange* points, defined by $\vec{\nabla}\phi_R = 0$. The point L_1 is known as the seddle point, it is the intersection between the *Roche* lobes of the two stars and it is crossed by matter in motion from the donor towards the accretor. In the (b) panel the potential wells of the system. [Frank et al.(2002)]

This means that until the surface of the donor star is smaller than its Roche lobe, then there is no tendency for material to be pulled off from the star because of the gravitational attraction of the other. The binary system is said to be detached and mass transfer could proceed only via the wind mechanism.

Supposing that for some reason, possibly stellar evolution, the donor star swells up so that its surface fills its Roche lobe. Since part of the envelope is in contact with the inner Lagrange point (L1) (see figure 1.1), any perturbation of this material will push it into the Roche lobe of the companion. Such perturbations are always present, due to, for instance, pressure forces. A system like this is called semi-detached, and it will transfer mass from the donor to the compact star very efficiently, as long as the Roche lobe of the massive star is filled.

1.1.2 Accretion disk

Once matter has passed through the Lagrange point L_1, in order to preserve its initial orbital angular momentum, it orbits around the compact objects, forming a disk, called accretion disk [Hartle(2003)]. Now, the velocity of gas particles can be decomposed into two components: radial component ($v_\parallel$), and tangential component ($v_\perp$).

Their values would be roughly:

$$v_\parallel \approx c_s = \sqrt{\frac{\partial P}{\partial \rho}} = \sqrt{\frac{k_B T}{\mu m_p}} \approx 10\sqrt{\frac{T}{10^4 K}}\text{km/s} \tag{1.6}$$

$$v_\perp \sim b_1 \omega \approx 100 \left(\frac{M_1}{M_\odot}\right)^{1/3} (1+q)^{1/3} \left(\frac{P}{1d}\right)^{-1/3} \text{km/s} \tag{1.7}$$

where μ is the mean molecular weight, ω is the angular velocity of the test particles, and b_1, in the equation (1.7), is given by $b_1 \approx a(0.5 - 0.227 \log q)$, a is the semi-major axis of particles' orbits, and q is the mass ratio M_2/M_1. By orders of magnitudes we conclude that $v_\perp \gg v_\parallel$. Thus, the disk which is forming, is composed by a collection of rings, on which particles move with velocity $v_\perp$ (neglecting the radial motion, so $v_\parallel$).

Particles, orbiting around the central star, are efficiently heated, because of dissipative mechanisms, up to a temperature of the order $kT_{disk}n \sim 0.5$keV. As a consequence, they start to radiate, losing energy. For a certain value of the specific orbital angular momentum l (angular momentum per unit of mass), the energy, ϵ, per unit of mass of a gas particle would depend only on the eccentricity e:

$$\epsilon = -\frac{(GM)^2(1-e^2)}{2l^2} \tag{1.8}$$

where G is the gravitational constant, and M the mass of the compact object. From equation (1.8) it can be seen that the minimum energy is the one with zero eccentricity ($e = 0$), which means that the associated orbit is a circular one. Thus, after having crossed the Lagrange point L_1, particles lose energy orbiting in the disk, up to reach the minimum energy required for a stable orbit, and so becoming circular.

While the circularization of the orbits is due to the emission of energy, the reduction of their dimensions is due to the loss of angular momentum because of viscous forces. These reduce the semi-major axis of the particles' orbits, moving them closer to the central star. The time needed to radiate energy and make the orbit circular is called t_{rad}, and it is related to the azimuthal velocity ($v_\perp$), while the time needed by viscous forces to transport angular momentum, towards the outer regions of the disk, is defined as t_{visc}, and it is related to the radial velocity ($v_\parallel$). Since $t_{visc} \ll t_{rad}$, and since the time is inversely proportional to the velocity, turns out that the azimuthal velocity is much higher then the radial one (as already seen in equations (1.6) and (1.7)). This explains why the radial motion (controlled by viscous forces) of gas particles is significantly slower than the orbital one, and the disk, as mentioned earlier, instead of a visible spiral, looks like an ensemble of rings. Particles' orbit, in fact, after have been reduced, because of angular momentum losses, become instantly circular.

The inward motion on nearly circular orbits continues up to a certain distance from the object, beyond which matter falls rapidly onto the compact object. More precisely, in case of a black hole, the rapid fall of particles starts after passing through the ISCO (innermost stable circular orbit), falling then inside the horizon.

In the case of neutron stars, the inner region of the disk is destroyed by their strong magnetic fields ($\sim 10^{12} - 10^{13}$G), and the accretion flow is channeled towards the magnetic poles, proceeding through column accretion. For black holes, instead, column accretion of this kind cannot occur, bacause of the lack of an intrinsic magnetic field [Frank et al.(2002)]. Another case, although less frequent, is when the magnetic field of the neutron star is too weak to truncate the disc, and the matter accretes towards the surface of the star, until it reaches a boundary layer, of a certain radial extend "d" just outside the surface of the accretor. Here it is decelerated from its keplerian angular velocity $\Omega_K(R_* + d)$ to the angular velocity of the neutron star $\Omega_*(R_*)$ (where R_* is the star radius).

1.2 Propeller effect

In the previous sections we have just introduced the accretion around a neutron star, without specifying when and if accretion is possible. There are various possible ways of interaction between neutron stars and matter. Let us consider a NS of mass M, radius R, spin period P, magnetic field B, and moving with velocity V relative to an ambient medium of number density n. In order to understand when and how accretion is possible around the NS, let us introduce three main characteristic lengths:

The **accretion radius**, r_{acc}, defines the region where the dynamics of the gas particles are dominated by the gravitational field of the NS, and it is given by

$$r_{acc} = \frac{2GM}{v^2} \sim 3 \times 10^{14} m v_{10}^{-2} \text{cm} \tag{1.9}$$

where $v_{10} = (V^2 + C_s^2)^{1/2}/(10\text{kms}^{-1})$, C_s is the sound speed of the gas particles and it is $\sim$ 10kms^{-1} [Treves et al.(2000)], and $m = M/M_\odot$. The equation (1.9) is derived in the framework of the Hoyle-Bondi theory of accretion, and,

although the estimate is an approximation, it is sufficient to understand the point for the following calculations.

The **Alfvén radius**, r_A, is the boundary within which the dynamics of the infalling material is dominated by the NS magnetic field. In spherical symmetry approximation:

$$r_A = \left(\frac{B^2 R^6}{\sqrt{2GM}\dot{M}}\right)^{2/7} \sim 2 \times 10^{10} B_{12}^{4/7} \dot{M}_{11}^{-2/7} R_6^{12/7} m^{-1/7} \text{cm} \tag{1.10}$$

where $\dot{M}$ is defined as the mass accretion rate (amount of mass which accretes per unit of time), $\dot{M}_{11} = \dot{M}/(10^{11}\text{gs}^{-1})$, $R_6 = R/(10^6\text{cm})$, and $B_{12} = B/(10^{12}\text{G})$ [Treves et al.(2000)]. A more detailed derivation of the Alfvén radius can be found in the next section.

The **corotation radius**, r_{cor}, is the distance at which the Keplerian velocity of gas particles equates the angular velocity of the NS:

$$r_{cor} = \left(\frac{GMP^2}{4\pi^2}\right)^{1/3} \sim 2 \times 10^8 m^{1/3} P^{2/3} \text{cm} \tag{1.11}$$

Studying accretion onto NSs, it should be taken into account that accretion could be prevented due to the momentum outflow produced by the NS magnetosphere co-rotating with the star itself. It can be shown that accretion do not occur if:

First, the Alfvén radius is larger than the accretion radius [Treves et al.(2000)], $r_A > r_{acc}$, in that case the system is in the so-called *georotator* stage.

Second, at the accretion radius the gravitational energy density of the incoming material

$$U_G = \frac{GMm_p n}{r} \sim 6.5 \times 10^{-13} \dot{M}_{11} r_{14}^{-5/2} \text{ergs cm}^{-3} \tag{1.12}$$

must be greater than the energy density, U_B, of the relativistic momentum outflow, produced by the rotating magnetic field B. The expression for the magnetic energy density, in the case of a dipolar field is

$$U_B = \left(\frac{B^2}{8\pi}\right)\left(\frac{R^6}{r_c^6}\right)\left(\frac{r_c^2}{r^2}\right) \sim 7.5 \times 10^{-9} B_{12}^2 P^{-4} R_6 r_{14}^{-2} \text{ergs cm}^{-3} \tag{1.13}$$

where $r_{14} = r/(10^{14}\text{cm})$ and $r_c = cP/2\pi$ is the light cylinder radius (c is the speed of light). This condition is met only if the period of the NS is larger than a certain value, the critical period P_{crit}, such that

$$P \geq P_{crit} \sim 10 B_{12}^{1/2} \dot{M}_{11}^{-1/4} (r_A)_{14} R_6^{3/2} m^{-1/8} \text{s}. \tag{1.14}$$

Thus, if $P < P_{crit}$, no accretion occurs and the NS is in the *ejector* phase; the duration of such phase could also exceed the NS lifetime ($\sim 10^7$yr). However, since the neutron star should slow down at the magnetic dipole rate, its spin period can increase and exceed the critical one, starting to accrete material.

After the increase of P, the material continues undisturbed until the Alfvén radius, where the NS magnetic energy density is balanced by the matter bulk kinetic energy density. Here, the corotating magnetosphere will prevent further

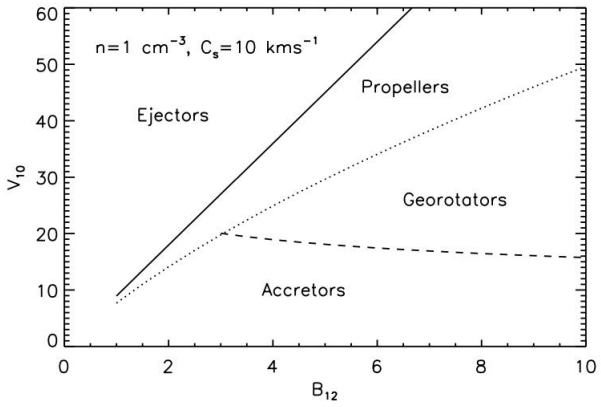

Figure 1.2: Different stages for an old neutron star as a function of the star velocity (in units of 10km s^{-1}), and magnetic field (in units of 10^{12}G) [Treves et al.(2000)].

accretion of matter, unless the gravitational acceleration is higher than the centrifugal pull [Treves et al.(2000)]:

$$\frac{GM}{r_A^2} \geq \left(\frac{2\pi}{P}\right)^2 r_A. \tag{1.15}$$

Also this third condition can be translated into a constraint on the period:

$$P \geq P_A \sim 10^3 B_{12}^{6/7} \dot{M}_{11}^{-1/2} m^{-1/2} \mathrm{s}. \tag{1.16}$$

If the period is shorter than P_A, then we would have an accumulation of matter at the Alfvén radius and the system remains in the *propeller* phase. The propeller effect, is a severe problem, since P_A is quite large, and so difficult to exceed. But there are two effects which can play an important role in the spin-down of the NS, making possible the accretion: the decay of the B field, and the torque exerted by the accreting material on the star itself.

Finally, if also the last condition is fulfilled, matter continues its motion towards the NS surface, and this becomes an *accretor*. In the figure 1.2 all these four possible stages are shown.

1.3 Accretion disk for magnetized NSs

Let us assume that the neutron star is in the accretor phase, and the magnetic field is strong enough to truncate the accretion disk. Since the interaction between the star magnetic field and the accretion disk is exceedingly complex in general, for the sake of simplicity here we consider the simple case in which the stellar magnetic field disrupts the accretion flow in the inner regions of the disk.

For a dipole magnetic field, the intensity of B is roughly

$$B \sim \frac{\mu}{r^3}, \tag{1.17}$$

where r is the radial distance from the star with radius R_*, $\mu = B_* R_*^3$ is the magnetic moment, which is constant once specified the surface field strength B_*. We can define the magnetic pressure:

$$P_{mag} = \left[\frac{4\pi}{\mu_0}\right] \frac{B^2}{8\pi} = \left[\frac{4\pi}{\mu_0}\right] \frac{\mu^2}{8\pi r^6} \tag{1.18}$$

as the matter approaches the stellar surface, the effects of such pressure increase, due to the dependence on r^{-6}. This magnetic pressure starts to control the matter flow truncating the infall at a radius r_A, thus exceeding the ram pressure of the matter. The ram pressure term is given by ρv^2, where ρ is the density, v is close to the free-fall value $v_{ff} = (2GM/r)^{1/2}$, giving $|\rho v|$ in term of the mass accretion rate $\dot{M}$:

$$\dot{M} = 4\pi r^2 |\rho v| \rightarrow |\rho v| = \frac{\dot{M}}{4\pi r^2}. \tag{1.19}$$

Setting $P_{mag}(r_A) = \rho v^2|_{r_A}$ we find:

$$\left[\frac{4\pi}{\mu_0}\right] \frac{\mu^2}{8\pi r_A^6} = \frac{(2GM)^{1/2}\dot{M}}{4\pi r_A^{5/2}}, \tag{1.20}$$

from equation (1.20) we can express r_A as

$$r_A = 5.1 \times 10^8 \dot{M}_{16}^{-2/7} m_1^{-1/7} \mu_{30}^{4/7} \text{cm}, \tag{1.21}$$

or, if we replace $\dot{M}$ in terms of the accretion luminosity ($L_{acc} = GM\dot{M}/R$), since it is more directly related to observational quantities

$$r_A = 2.9 \times 10^8 m_1^{1/7} R_6^{-2/7} L_{37}^{-2/7} \mu_{30}^{4/7} \text{cm}, \tag{1.22}$$

with the parameters in units of typical values for a neutron star.

Both estimates, (1.21) and (1.22), are kind of rough, but, since P_{mag} is a step function of radius ($\sim r^{-6}$), they can be accepted as a first-order approximation. As already mentioned, the distance r_A is called Alfvén radius, and within it we expect that the magnetic pressure dominates the dynamics of gas particles, which start to move along magnetic field lines, towards the magnetic poles of the star (figure 1.3).

When accretion is controlled by the magnetic field of the source, it gives rise to a simple and recognizable observational signature, due to the fact that the accretion flow is funneled only onto a small fraction of the total stellar surface (figure 1.3).

In figure 1.3, at the point A, particles leaves the disk following the field lines. In polar coordinates, using a system whose origin is at the center of the star, with the z axis directed along the magnetic one, and having assumed a dipole magnetic field, the equation for the field lines is approximately: $r = C \sin\theta^2$, where C is a constant, and θ the magnetic colatitude. At A, $r = r_A$ (R_M in the figure) and $\theta = \alpha$ (where α is the magnetic colatitude at the Alfvèn radius), so $C = r_A / \sin\alpha^2$. The same field line will then cross the stellar surface at $r = R_*$ at a magnetic colatitude β given by

$$\sin^2\beta = \frac{R_*}{C} = \left(\frac{R_*}{r_A}\right) \sin^2\alpha. \tag{1.23}$$

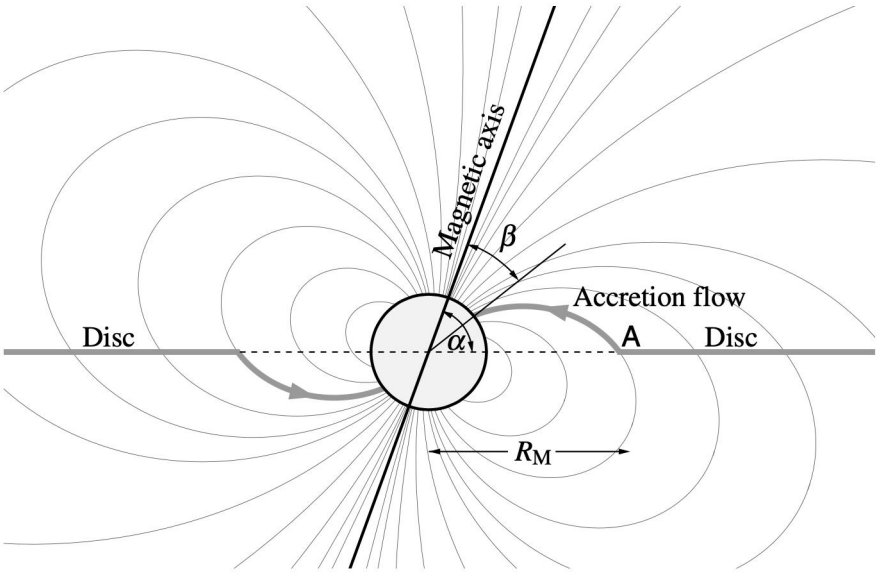

Figure 1.3: Schematic illustration of accretion onto a NS from a surrounding accretion disk. The curved lines are the magnetic field lines, and the disk is truncated at the Alvén radius (point A), where particles are then funneled onto the magnetic poles.[Frank et al.(2002)]

Neglecting possible effects due to plasma instabilities, accretion cannot take place for colatitudes larger than β, since the field lines that will cross the disk plane for distances lower than the Alfvén radius, would collect a little amount of matter. Thus the accretion will be concentrated only within the region with angular amplitude β.

The area of an accreting polecup is a fraction

$$f_{disk} \sim \frac{\pi R_*^2 \sin^2 \beta}{4\pi R_*^2} \cong \frac{R_* \sin^2 \alpha}{4 r_A} \tag{1.24}$$

of the total stellar surface, with accretion that can take place also on the opposite pole. The estimate of f_{disk} is subjected to many uncertainties because of the complicated role of plasma instabilities.Nevertheless, its value would be always smaller than unity.

We can conclude saying that, in case of interaction between the accretion disk and the magnetic field of the NS, matter do not accrete all over the surface of the star, but instead, just inside a small region, of area f_{disk}, where an accretion column can be formed (as we will see in Chapter 3).

1.4 Efficiency of accretion onto compact objects

The extraction of gravitational potential energy from material which is accreting onto a massive object is known to be the main source of electromagnetic

emission in several types of binary systems, e.g. it is believed to provide the power supply in active galactic nuclei (AGN) and quasars. Thus, accretion onto compact objects is a natural and powerful mechanism for producing high-energy radiation.

1.4.1 Energy emitted through accretion

Let us consider a body of mass M and radius R, the gravitational potential energy released by the accretion of a mass m, initially very far from the object, and arriving on on its surface would be:

$$\Delta E_{acc} = \frac{GMm}{R} \tag{1.25}$$

Taking typical values of R and M for neutron stars, $R \sim 10$km and $M \sim M_{\odot}$, then ΔE_{acc} will be about 10^{20}ergs per accreted gram. This energy is supposed to be emitted mainly in the form of electromagnetic radiation (in fact, the rest of the energy can be also transformed into kinetic energy, in relativistic jets of particles). The amount of energy released can be then compared to the energy extracted from a mass m by nuclear fusion reactions (the highest energy release is obtained for hydrogen burning) in stellar nucleosynthesis. The latter gives an amount of energy which is around $1/20$ of the accretion one [Frank et al.(2002)].

From equation (1.25) it is clear that, the energy emitted through accretion is strongly dependent on the *compactness* of the accreting object, i.e. on the ratio M/R: the higher the ratio, the larger the efficiency. Hence, for black holes and neutron stars accretion can be much more efficient than nuclear burning.

A consequence of equation (1.25) is that fixing the value of the compactness, luminosity will depend only on the mass accretion rate $\dot{M}$. In particular, when the luminosity becomes quite high, it can halt the accretion itself, since the radiation pressure, exerted on accreting particles, would be so strong that their accretion onto the surface of the object is inhibited. This leads to the definition of a maximum luminosity, given a certain M/R ratio.

1.4.2 Eddington luminosity

For the sake of simplicity, let us consider a steady, spherically symmetric configuration with mainly fully ionized hydrogen accreting onto a compact object. Under these circumstances the radiation will exert a force onto particles (electrons and protons) and we can fairly assume it is generated by Thomson scattering. In addition, since Thomson differential cross-section is inversely proportional to the square of the mass of the particle, scattering onto protons can be neglected with respect to free electrons (since the mass of the proton is about ~ 2000 times that of the electron).

Defining as S the radiant energy flux $L/4\pi r^2$ ergs^{-1}cm^{-2}, the outward radial force exerted on each electron equals the rate at which it absorbs momentum, $\sigma_T S/c$ (where $\sigma_T = 6.7 \times 10^{-25}$cm^2 is the Thomson scattering cross section). As the electrons move outward, they drag with them protons, because of Coulomb interaction. So radiation pushes out electron-proton pairs against the total gravitational force, which acts on each pair at a radial distance r from the centre:

$$\frac{GM(m_p + m_e)}{r^2} \cong \frac{GMm_p}{r^2}. \tag{1.26}$$

The net inward force on an electron-proton pair is:

$$\left(GMm_p - \frac{L\sigma_T}{4\pi c}\right)\frac{1}{r^2} \tag{1.27}$$

and we call Eddington luminosity that value of L at which the force (1.27) vanishes:

$$L_{Edd} = \frac{4\pi GMm_p c}{\sigma_T} \cong 1.3 \times 10^{38}\left(\frac{M}{M_\odot}\right) \text{ erg s}^{-1}. \tag{1.28}$$

This value for L is the maximum one to avoid the inhibition of the accretion due to radiation pressure. In fact, as stated before, at high values of the luminosity the outward radiation pressure would exceed the inward gravitational attraction and accretion will be halted.
It is important to stress that this value for L_{Edd} has been derived making some assumptions:

1. **steady and spherically symmetric accretion flow (Bondi flow)**, if the accretion occurs only over a fraction f of the entire surface of the object the accretion luminosity associated would be fL_{Edd}. If the geometry is even more complicated, the equation (1.28) gives a crude estimate;

2. **accreting material made mainly by hydrogen**, which is almost always a good approximation, in a great number of cases;

3. **fully ionized hydrogen**;

4. **Thomson scattering limit**, it is quite always a good hypothesis.

Despite these technicalities, the Eddington limit is of great practical importance and for accretion-powered objects it implies a limit on the steady accretion rate $\dot{M}$.

Maximum accretion rate

The value of this maximum luminosity over which accretion is halted puts constraints on the mass accretion rate $\dot{M}$, and we can obtain this maximum value for $\dot{M}$ ($\dot{M}_{Edd}$). Starting from equation (1.31), dividing and multiplying by c^2 on the right hand side, one can rewrite:

$$L_{acc} = \eta \dot{M} c^2, \tag{1.29}$$

where the parameter $\eta = GM/Rc^2$ is called the efficiency of the accretion process. Equating this to the Eddington luminosity (1.28), we derive an expression for the limiting value of $\dot{M}$:

$$\eta \dot{M} c^2 = \frac{4\pi GMm_p c}{\sigma_T} \longrightarrow \dot{M}_{Edd} = \frac{L_{Edd}}{\eta c^2}. \tag{1.30}$$

Taking now the example in which all the kinetic energy of inafalling matter is transformed into radiation at the stellar surface, then from equation (1.25) the accretion luminosity is:

$$L_{acc} = \frac{GM\dot{M}}{R} \tag{1.31}$$

$$L_{acc} = 1.3 \times 10^{36} \dot{M}_{16} \left(\frac{M}{M_\odot}\right) \left(\frac{R}{10\text{km}}\right)^{-1} \text{erg s}^{-1} \tag{1.32}$$

where L_{acc} in the (1.32) has been expressed in terms of typical values for neutron stars. If we compare this equation with equation (1.28), we obtain that the mass accretion rate, $\dot{M}_{16}$ (where $\dot{M}_{16}$ means that is normalized with respect to the value 10^{16} gs^{-1}), is limited by a value of $\sim 10^2$gs^{-1}.

Thus, if the previous assumptions made to compute the Eddington luminosity hold, the mass accretion rate must be less than 10^{18}gs^{-1}, for a neutron star.

Efficiency of the accretion process

At this point it is useful to estimate the efficiency of the accretion process, starting from the specific energy of the gas at the inner radius of the disk, R_{in}. This is the star radius in the case of a neutron star and the ISCO in the case of a black hole.
The specific energy at R_{in} is:

$$\epsilon(R_{in}) = -\frac{GM}{R_{in}} + \frac{1}{2}v_K^2 = -\frac{1}{2}\frac{GM}{R_{in}} \tag{1.33}$$

where $v_K = \sqrt{GM/R_{in}}$ is the Keplerian velocity. The variation of ϵ in the accretion process can be computed assuming that matter starts accreting from an infinite distance from the object, since the external radius of the disk is much longer than the inner one, $R_{ex} \gg R_{in}$. Thus:

$$\Delta\epsilon = \epsilon_{\text{inf}} - \epsilon(R_{in}) = \frac{1}{2}\frac{GM}{R_{in}}. \tag{1.34}$$

Therefore the luminosity of the disk will be:

$$L_{disc} = \frac{1}{2}\frac{GM}{R_{in}}\dot{M}c^2 \tag{1.35}$$

which is exactly half of the accretion luminosity:

$$L_{acc} = \frac{GM}{R}\dot{M}c^2. \tag{1.36}$$

CHAPTER

TWO

ULTRA-LUMINOUS X-RAY SOURCES

Ultra-luminous X-ray sources (ULXs) are among the most peculiar extragalactic objects, with X-ray luminosities $L_X \geq 10^{39}$ erg s^{-1} (as stated above). They often dominate the total X-ray emission of their host galaxy. They are generally too bright to be low-mass X-ray binaries (LMXBs), for which $L_X \leq 10^{37}$ erg s^{-1}, and too dim when compared to active galactic nuclei (AGNs), for which $L_X \geq 10^{41}$ erg s^{-1}, with their position being off-centre in their host galaxy. Their properties have been largely explored, their spectra are well described by a two component model (disk plus a corona), and show a characteristic cut-off between 2 and 10 keV. Some ULXs also present spectral time variability, while others exhibit coherent pulsations in their signals, leading to the discovery of pulsating ULXs (PULXs).

2.1 The discovery of ULXs

The first observation of ULXs dates back to the 80s, when the Einstein X-ray Observatory revealed the existence of 16 of these objects ([Long et al.(1983)]; [Helfand(1984)]; [Fabbiano(1989)]). Soon, the ROSAT satellite extended their number to nearly 100 ([Roberts & Warwick(2000)]; [Colbert & Ptak(2002)]). Yet these object are rare, with an occurrence of only 1-2 per galaxy from pointed X-ray observations ([Colbert et al.(2004)]; [Kilgard et al.(2002)];[Colbert & Ptak(2002)]; [Foschini et al.(2002)];[Humphrey et al.(2003)]; [Irwin et al.(2003)]), and perhaps occurring much less frequently in the local Universe as a whole. At the time of the first detection there were several uncertainties about the nature of such objects: it was thought that ULXs could represent the high-luminosity end of a continuous distribution of conventional X-ray sources such as supernovae and X-ray binaries ([Grimm et al.(2003)Grimm, Gilfanov, & Sunyaev]), or that they could involve new types of objects such as intermediate mass black holes (IMBHs) ([Colbert & Mushotzky(1999)]; [Makishima et al.(2000)]; [Colbert & Ptak(2002)]; [Van Der Marel(2004)]), beamed sources ([King et al.(2001)]; [Georganopoulos et al.(2002)]; [Körding et al.(2002)]) and hypernovae ([Wang(1999)]). Part of the reason why ULXs were, as a class, poorly understood is that past X-

ray observatories lack of the combination of high angular resolution and moderate spectral resolution, needed to adequately characterize discrete X-ray sources in nearby galaxies [Swartz et al.(2004)]. One of the main consequences was that ULXs were difficult to distinguish from other nearby X-ray sources and from diffuse emission in the field. Subsequently, thanks to the remarkable advancements in the field of high-energy instrumentation, through missions like *Chandra X-ray Observatory* and *XMM-Newton* (X-ray Multi-Mirror Mission-Newton), it was possible to reveal many more details on ULXs, such as their location, X-ray luminosities, spectral and timing properties. In the case of Chandra, for instance, we have both a moderate spectral resolution and the best spatial resolution achieved as yet in X-ray telescopes available. For this reason it was also possible to further extend the list of ULXs up to 154, in 82 galaxies.

2.2 ULXs phenomenology

2.2.1 Principal evidences

ULXs are non-nuclear objects found in external galaxies that seem very luminous assuming isotropic emission [Kaaret et al.(2001)]. They are thought to be X-ray binaries powered by accretion onto a compact object, with a luminosity which exceeds the Eddington one for stellar mass black holes (SMBHs).

X-ray binary systems are classified as ultraluminous one according to whether their luminosity exceeds some threshold value. This can be: 10^{39} erg s^{-1}, which is convenient in centimeter-gram-second units and it tends to be used for population studies as it produces larger samples, or 3×10^{39} erg s^{-1}, which closely corresponds to the Eddington luminosity for a $20M_{\odot}$ black hole.

2.2.2 X-ray luminosity functions

The number of X-ray binaries in external galaxies has been investigated through the X-ray luminosity function (XLF), for both star-forming galaxies and old elliptical ones. As it can be seen in Figure 2.1, the XLF for star-forming galaxies has a break at luminosities of $\sim 10^{40}$ erg s^{-1} ([Swartz et al.(2011)], [Mineo et al.(2012)]), while for elliptical galaxies the break is at $\sim 10^{38}$ erg s^{-1} ([Gilfanov(2004)], [Kim & Fabbiano(2010)]). These XLFs have been plotted assuming isotropic luminosity; if we take into account also the beaming, then the breaks would occur at values higher than the physical luminosity expected. Thus, the break showed in the elliptical XLF could correspond to the Eddington luminosity for neutron stars, suggesting, in those galaxies, the presence of few black hole binaries (BHBs). However, the break in the star-forming XLF corresponds to objects 20 times more massive than NSs, and since neutron star binaries are estimated to be 10–50 times more numerous than BHBs, the lack of the break at NS Eddington luminosity in the star-forming XLF puts doubts on whether the break is related to the Eddington luminosity.

For sources with luminosity above $L_X > 2 \times 10^{40}$ erg s^{-1} (above the break) may be defined a new class of objects: hyperluminous X-ray source (HLX) [Matsumoto et al. (2003)]. These could be the best candidate for intermediate mass black holes (IMBHs). From XLFs predictions, there should be at most one HLX within 100Mpc [Swartz et al.(2011)].

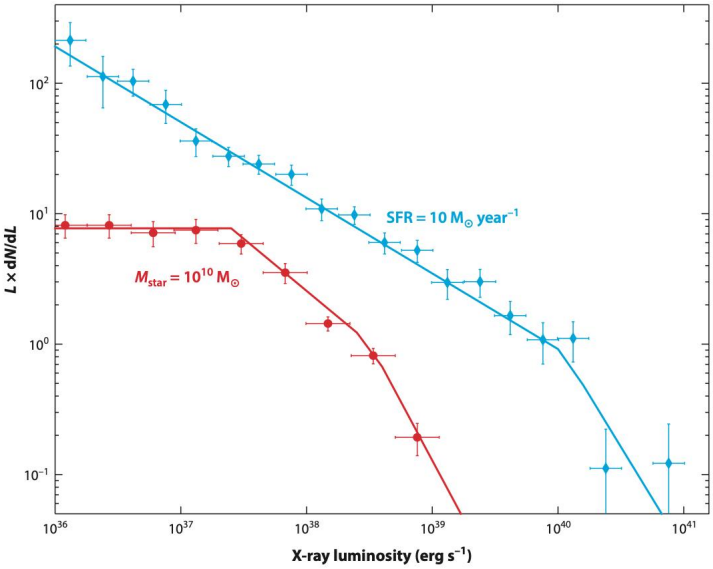

Figure 2.1: X-ray luminosity functions for star-forming galaxies (cyan), i.e. with a star formation rate (SFR) of $10 M_{\odot}$ year^{-1}, and for old elliptical galaxies (red) with stellar masses of $10^{10} M_{\odot}$.

From XLFs was also possible to see that the X-ray binary population of a galaxy is correlated with: its star-formation rate (SFR), if it is a star-forming galaxy, and stellar mass, if it is an elliptical one [Colbert et al.(2004)]. Dominance of the former suggests that their ULX population is young, with ages around tens of Myr, instead, dominance of the latter suggests that their ULX population is old with ages of Gyr.

2.2.3 Galactic X-ray Binaries

The main X-ray binary population that was examined to understand ULXs characteristics was the Galactic black hole X-ray binaries population (GBHBs). But what came out from that study was that ULXs show several differences with respect to GBHBs. First of all, GBHBs exhibit significant variability, with the X-ray flux that, in some cases, can vary up to factors greater than 10^7 [Remillard & McClintock(2006)]; most of them have low-mass companion stars and are transient objects, usually in a quiescent state; and flare to high luminosities, sometimes close to the Eddington limit for weeks to months. Diversely, most ULXs are persistent for years or decades, and the variability of ULXs is much lower than that of GBHBs. In fact, in elliptical galaxies, ULXs typically show low levels of variability [Feng & Kaaret(2006)], while those in star-forming galaxies are variable by factors that at most reach 10 [Feng & Kaaret(2009)]. Variability by large factors, above 100, is uncommon, but seen in some ULXs (e.g. [Bachetti et al.(2014)]).

Moving on the spectra, GBHBs spectra in the X-rays are widely modeled as the sum of two components: a multicolor disk blackbody (DBB), which probably arise from the accretion disk, and a power law or Comptonization component,

which is probably due to a corona. In addition, if the disk component fairly represents a standard thin accretion disk, which extends towards the innermost stable circular orbit (ISCO) of the black hole, then the inner radius of the disk should be constant, and exists a particular relation between the bolometric disk luminosity, L_d, and the disk inner temperature, T_{in}: $L_d \propto T_{in}^4$. This is accurately demonstrated in the thermal state of GBHBs [Gierliński & Done(2004)].

Although the spectra of ULXs are often compared with those of GBHBs, it should be noted that observational data for GBHBs has mainly been obtained by instrument designed for Galactic science. These present a limited sensitivity below 3 keV, while a large collecting area at energies up to $\sim$ 25 keV. For ULXs, instead, spectra have generally been obtained by observatories more specifically designed for extragalactic science, with CCD detectors and focusing optics, operating in the $\sim$ 0.5–10 keV regime.

2.2.4 X-ray spectra

The first view of ULX spectra emerged from the *Advanced Satellite for Cosmology and Astrophysics* (ASCA), in the 1990s [Colbert & Mushotzky(1999)]. From those data came out that several ULX spectra seem to be dominated by a single spectral component convex in shape, and well represented by accretion disk models. These disks turn out to be both hotter ($kT_{in} \approx 1.1 - 1.8$ keV) and more luminous than those for GBHBs. To explain such properties, it was suggested [Makishima et al.(2000)] that this was a consequence of the fact that ULXs host large stellar-mass black holes, with masses up to $\sim 100 M_{\odot}$, and with a such fast rotation that the disk is forced to move close to the black hole, being heated up. Some ULXs also show in their spectra a power-law component, and from this it was noted that a strongly Comptonized disk spectrum provides a good physical explanation [Kubota et al.(2002)]. But from deeper observations with a better resolution (Chandra and XMM-Newton), soon it became clear that single-component models, power laws or simple accretion disk models (standard multicolor DBB), are not sufficient to fit the spectra. In fact, the spectra required the inclusion of a second component or of a more complex single-component models.

More importantly, high quality XMM-Newton data revealed that the hard emission is not properly a power law; it shows a knee-like feature in the 2–10 keV band ([Feng & Kaaret(2005)], [Roberts et al.(2005)]). This feature has been highlighted by NuSTAR (Nuclear Spectroscopic Telescope Array) observations, and, thanks to its extended hard bandpass, it was showed that such curvature extends above 10 keV (figure 2.2) [Bachetti et al.(2013)]. This knee-like feature is well described by a break at energies of 2–7 keV [Gladstone et al.(2009)], while in GBHBs the same break is at energies typically $\sim$ 60 keV or above [McClintock & Remillard(2006)]. Thus, the classical GBHB X-ray spectral model cannot be applied to ULXs, and the cool component seems not to be interpreted as a disk for IMBHs, accreting at a sub-Eddington rate.

The luminosity at which the two-component spectra are seen, the majority of times, is above 3×10^{39} erg s^{-1}. This could represent a super-Eddington ultraluminous (UL) state.

From the physics of such sources, the best two-component model was that with DBB and a Comptonized corona. The disk temperature is cool, kT_{in} $\sim$ 0.1–0.3keV, and the corona appear cool and thick with $kT_e \sim$ 1–2keV and

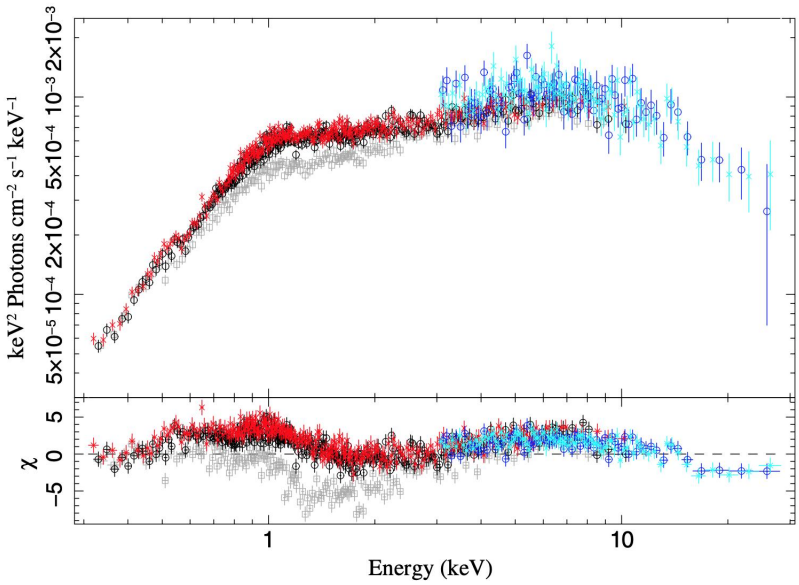

Figure 2.2: EPIC-pn and NuSTAR unfolded spectrum of NGC 1313 X-1 during two observations. Black and red points are EPIC-pn data, and blue and cyan FPMA data. Circles indicate the first observation, crosses indicate the second. The spectrum shows a soft excess and a cutoff, as observed in this source when in its low-flux state [Bachetti et al.(2013)].

$\tau > 6$. This in contrast with GBHBs spectra, where, instead, the corona is hot and thin, and with electron temperature $kT_e \sim 100$ keV, and optical depth $\tau \leq 1$. From these fits arose the suggestion that the inner accretion disks of ULXs are surrounded by an optically thick corona, which leaves visible, as the soft excess, only the outer regions of the disk. This scenario was exploited in a model used by [Gladstone et al.(2009)] to recover temperatures of the, just mentioned, accretion disk of $\sim$ 1keV in most cases, consistent with stellar-mass black holes.

2.2.5 Spectral variability

Another important characteristic emerged from analysis on ULXs' spectra, is that some ULXs show different specrtra in different epochs [Kubota et al.(2001)]. The best way to analyse that time variability is through X-ray color analyses. The study of this variability showed contrasting results in the relation of disk X-ray luminosity to temperature. For instance, for ULXs that could be fitted with single-component disk-like spectra holds a positive disk luminosity versus temperature evolution [Kajava & Poutanen(2009)], as seen from GBHBs, while an opposite trend (disk luminosity decreases with temperature) holds in models used to fit the NGC 1313 X-2 specrum (see figure 2.3) [Feng & Kaaret(2007a)]. This trend was obtained from studies on the evolution of disk luminosity and temperature in the (cool) DBB, plus power-law model. The fact that the disk luminosity decreases with temperature is in strong contrast to the $L \propto T^4$ re-

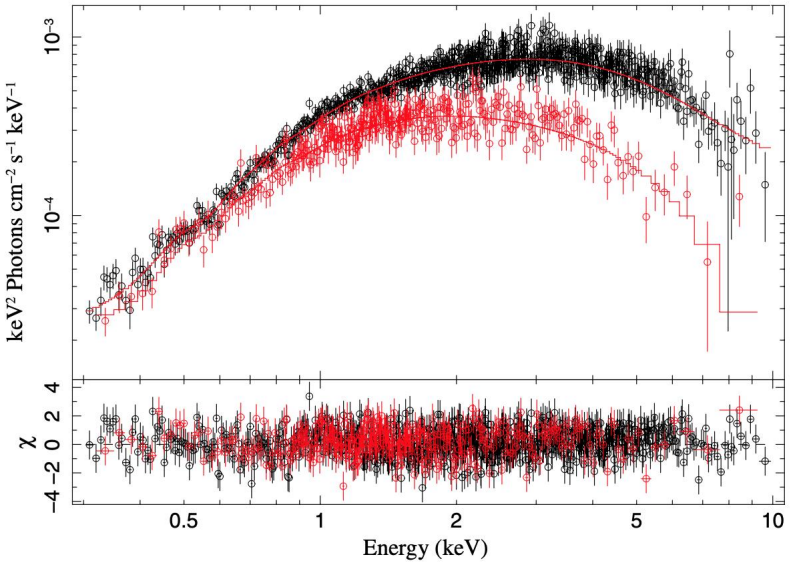

Figure 2.3: XMM-Newton unfolded spectra of NGC 1313 X-2 during two observations. Black points are EPIC-pn data and red points are EPIC-MOS1 data [Bachetti et al.(2013)].

lation expected for an accretion disk with a fixed inner radius. From a more detailed study [Kajava & Poutanen(2009)], on a large sample of ULXs, that relation turned out to be $L \propto T^{-3.5}$. However, this result was contested by [Miller et al.(2013)], since in some ULXs was found a luminosity-temperature relation, for disks in soft component, close to the predicted one (for standard disks): $L \propto T^4$. At the same time, the cooling of the soft component with increased luminosity is strongly confirmed in supersoft ULXs (SSULXs) [Urquhart & Soria(2016)], in which the soft component is much more clearly visible, due to the weakness of the hard one.

2.3 ULXs powered by IMBHs and SMBHs

As previously mentioned, since ULX luminosities are typically higher than the Eddington limit for SMBHs ($\sim 10^{39} ergs^{-1}$), one of the first hypothesis was that ULXs are powered by IMBHs, black holes with masses larger than 100 $M_\odot$ and up to $10^3 M_\odot$. In fact, taking into account that the Eddington luminosity depends directly on the mass of the source, values of the order of 0.1-0.01L_{Edd} can be easily reached for this class of objects. In that case accretion proceeds at a sub-Eddington rate. This accretion regime is typical for Galactic black hole binaries (GBHBs), as seen above, so the IMBH model might implies that ULXs are massive GBHBs. But after the first high-quality observations from Chandra and XMM-Newton it became clear that spectra of ULXs differ from those observed in GBHBs ([Stobbart et al.(2006)],[Gladstone et al.(2009)],[Atapin(2018)]).

Furthermore, different observational evidences have been obtained against the IMBHs hypothesis. According to Makishima et al. (2000)[Makishima et al.(2000)],

the IMBH X-ray spectrum should consists of a bright soft thermal component (blackbody) with a characteristic temperature of 1 keV and a hard tail. From analysis on a sample of 154 ULXs candidates [Swartz et al.(2004)] no match was found. Moreover, IMBHs can also display soft/hard spectral transitions, as predicted by Kalogera et al. (2004) [Kalogera et al.(2004)], this is a consequence of a thermal-viscous disk instability. None of these transitions were found in the observations of the same ULXs sample.

Moreover, it is believed that IMBHs form from individual population III stars (the first stellar population, the massive one), thus their distribution should be all across the host galaxy, and in all galaxy types ([Madau & Rees(2001)]). In particular, an higher occurrence is expected in elliptical galaxies, in which are present numerous globular clusters, thus dense stellar environments in which such sources could have been formed. In addition, the ULXs spatial distribution should be that of the halo stars, contrary to the distribution of weaker sources, which are mainly distributed across the disk and the bulge of the galaxies (such as spirals) ([Swartz et al.(2004)]). From the same previous sample of 154 sources, ULXs, instead, show the same distribution of the weaker sources, and the occurrence of ULXs in cluster-rich elliptical galaxies is no greater than that for spirals.

Although the SMBHs have masses too small, compared to those of IMBHs, in order to explain such high X-ray luminosities, they still remain a valid hypothesis if (with or without beaming) the accretion of material proceeds at super-Eddington rate ([Fabrika & Mescheryakov(2001)],[King et al.(2001)], [Poutanen et al.(2007)]). In this case, ULXs can be compared to the Galactic superaccretor SS 433 ([Fabrika(1997)], [Fabrika(2006)]). In such system the compact object accretes material from an evolved A-type supergiant, through the Roche-lobe mechanism (see subsection 1.1.1). Showing also strong optically-thick outflow and semi-relativistic baryonic jets [Fabrika(2006)]. Its apparent X-ray luminosity is about 10^{36}erg s^{-1}, but probably this is due to its high inclination, if visible in a face-on configuration the luminosity may be even higher, and it might look like as an ULX [Fabrika & Mescheryakov(2001)].

2.4 Discovery of ULXs powered by Neutron Stars

Through the X-ray timing it was possible to identify neutron star accretors. Although X-ray timing is a powerful technique, it also requires a large number of photons, and extensive monitoring campaigns. As a consequence, it has been possible to obtain an high signal-to-noise power spectra, and to do extensive monitoring campaigns only for few ULXs.

2.4.1 NuSTAR J095551+6940.8

In 2014 the NuSTAR high energy X-ray mission observed the galaxy M82 [Harrison et al.(2013)], located at 3.6 Mpc from the Milky Way, between January 23 and March 26, due to a follow-up campaign of the supernova SN2014J. In the galaxy disk can be found several ULXs, the most luminous are: M82 X-1 [Kaaret et al.(2001)], with a maximum luminosity $L_X(0.3-10keV) \sim 10^{41}$ergs^{-1}, and M82 X-2 (figure 2.4), a transient source, with maximum lumi-

nosity $L_X(0.3-10keV) \sim 1.8 \times 10^{40}$ erg s^{-1}. Since the separation between the two is of 5", they could only be distinguished by Chandra [Bachetti et al.(2014)].

In the region in which are located these two sources, were found for the first time, through NuSTAR observations, coherent pulsations. These showed an average period of 1.37 s, and a 2.5 day sinusoidal modulation. Such signal was identified as NuSTAR J095551+6940.8. In the same epoch, thus during the detection of such pulsations, Chandra observed M82, and only two sources in the Chandra image, the previously mentioned M82 X-1 and M82 X-2, were sufficiently luminous to be the counterpart of NuSTAR J095551+6940.8, and then, after further investigations, the centroid of the pulsed emission turn out to be consistent with the location of M82 X-2. Soon after, M82 X-2 was identified as a neutron star (NS), accreting from a stellar companion via Roche lobe overflow (subsection 1.1.1). The last intuition is a consequence of the highly circular orbit, which suggests the action of strong tidal torques, combined with the high luminosity.

NuSTAR J095551+6940.8 exhibited a luminosity $L_X(0.5-30keV) \sim 10^{40}$ erg s^{-1}. From a theoretical point of view, such X-ray luminosity can be achieved with the presence of strong magnetic fields and for the particular geometry of the accretion channel. A deeper discussion of the emission model will be addressed in the central part of this thesis.

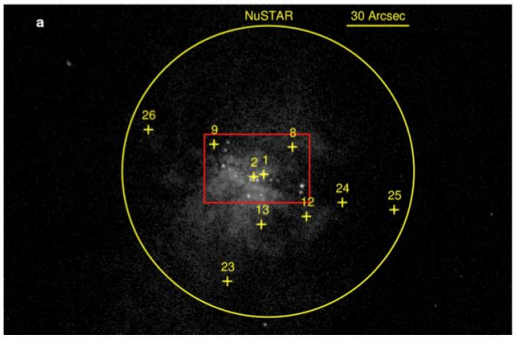

Figure 2.4: Chandra image of the central region of M82. The yellow circle shows the 70" radius region used to extract NuSTAR fluxes. Within this region 24 discrete X-ray point sources were identified [Bachetti et al.(2014)].

After the discovery of this PULX, several other sources were revealed by other surveys.

2.4.2 NGC 7793 P13

Fürst et al. (2016) [Fürst et al.(2016)] reported on the detection of coherent pulsations from the ultraluminous X-ray source NGC 7793 P13. XMM-Newton and NuSTAR were the first, in 2016 in broadband X-ray observations, to detect NGC 7793 P13 sinusoidal pulsations, with a period of ∼0.42 s. They also found pulsations in archival XMM-Newton data taken in 2013 and 2014. From this

discovery turned out that the compact object (NGC 7793 P13) is a neutron star, showing a maximum luminosity of $\sim 10^{40}$ erg s^{-1}, this once one has assumed isotropy emission. Such luminosity is well above the Eddington limit for an accretor with mass of $1.4M_{\odot}$, as a consequence NGC 7793 P13 became the second ULX known to be powered by an accreting neutron star.

2.4.3 NGC 5907 ULX1

Israel et al. (2017) [Israel et al.(2017)] carried out a search for new X-ray pulsating sources, taking data from the archival of the European Photon Imaging Camera (EPIC) ([Strüder et al.(2001)], [Turner et al.(2001)]). This search was made thanks to the project "Exploring the X-ray Transient and variable Sky", which had as goal that of characterizing the variability of X-ray sources observed with the XMM–Newton satellite.

A coherent signal in the X-rays was found, between July 9 and 10 in 2014, in the spiral galaxy NGC 5907, which is located at 17.1 Mpc from the Milky Way ([Tully et al.(2013)]). From the Fourier power spectrum of the 0.2–12 keV light curve of the source, they detect a peak in the emission at the frequency of $\sim$0.88 Hz, and with a period of $\sim$ 1.137s.

Through a more complete search, they managed to detect the same signal also in earlier observations, made with XMM–Newton in February 2003 (measuring a period of $\sim$ 1.428s), and with NuSTAR ([Harrison et al.(2013)]) in July 2014 (with a period of $\sim$ 1.136s). Leading to the confirmation of the presence of a PULX, NGC 5907 ULX. The luminosity measured with Swift, Chandra, XMM–Newton, and NuSTAR exhibits a pronounced variability, its bolometric luminosity ranging between $(2.6 \pm 0.3)\times10^{40}$erg s^{-1} and $(2.2 \pm 0.3)\times10^{41}$erg s^{-1}.

2.4.4 NGC 300 ULX1

Carpano et al. (2018) [Carpano et al.(2018)] discovered an intense periodic signal in the X-rays, which presented a period of 31.6 s and a rapid spin up, confirming in this way that the object was a neutron star.

The observation targeted the galaxy NGC 300, it is located in the group of the Sculptor, at a distance of 1.88 Mpc [Gieren et al.(2005)], and it is seen in a face-on configuration. The X-ray sources which populate that galaxy have been already studied with missions like ROSAT [Read & Pietsch(2001)], and XMM-Newton [Carpano et al.(2005)].

Before the discovery of NGC 300 ULX1, the brightest X-ray source detected was the Wolf–Rayet/black hole X-ray binary NGC 300 X-1, which showed a luminosity of $\sim 2 \times 10^{38}$erg s^{-1} [Carpano et al.(2007)]. But in May 2010, in the optical energy band, appeared a new brighter source, which was, at the beginning, classified as a supernova (SN 2010da) [Monard(2010)]. The unabsorbed luminosity of the source was obtained by Swift XRT, with the values of 6×10^{38}erg s^{-1} [Immler et al.(2010)], and later on also by Chandra ACIS-I, with a value of $\sim 2\times10^{37}$ erg s^{-1} in the 0.3–10 keV energy range [Binder et al.(2011)].

It was concluded that the system was a high-mass X-ray binary (HMXB) system in outburst, additional observations were made by Chandra in 2014 [Binder et al.(2016)], highlighting the variation of the luminosity by a factor of ~ 10, going from $\sim 4\times10^{36}$ ergs^{-1} to $\sim 4\times10^{37}$erg s^{-1}. A better interpretation

of the nature of the source was done using spectroscopic and photometric data, in the ultraviolet to infrared energy range. This allowed to say that the source is, in reality, a supergiant B[e] HMXB ([Lau et al.(2016)], [Villar et al.(2016)]).

2.4.5 NGC 1313 X-2

Sathyaprakash et al. (2019) [Sathyaprakash et al.(2019)] revealed a weak pulsation from the archetypal ultra-luminous X-ray source NGC 1313 X-2, such pulsations showed a period of ∼1.5 s and a pulsed fraction of ∼ 5%. The PULX is located in the outer regions of the barred spiral galaxy NGC 1313, and it is one of the historical, best-studied ULXs in terms of both its X-ray properties ([Feng & Kaaret(2007b)], [Pintore & Zampieri(2012)]) and its optical counterpart and environment [Grisé et al.(2008)]. The source is probably seen with a low inclination angle ([Sutton et al.(2013)], [Middleton et al.(2015)]), and this is suggested by the lack of radial velocity variations in the optical spectrum [Roberts et al.(2011)], and of flux variability. Although this view does not allow to record intense pulsations, it provides, however, to have a direct view of the central areas of the accretion flow.

2.4.6 M51 ULX-7

Rodríguez Castillo et al. (2020) [Castillo et al.(2020)] discovered an ultra-luminous X-ray source in the suburb of the M51 galaxy, at a distance of 8.6 Mpc: M51 ULX-7, which presented 2.8 s pulsations in the X-ray emission, with a pulse sinusoidal shape. That discovery was done during an observation of 78ks, within the XMM-Newton Large Program UNSEeN. M51 ULX-7 is generally observed with an X-ray luminosity between 10^{39} and 10^{40}erg s^{-1} (in the energy range of 0.3–10 keV). The X-ray source presents an orbit of 2 days, a NS mass of 1.4M$_\odot$, and a lower limit for the companion mass of $8M_\odot$, which classify the system of this PULX as an high-mass X-ray binary.

CHAPTER

THREE

ACCRETION ONTO MAGNETIZED NEUTRON STARS

The main purpose of this thesis is to present the current scenarios for accretion onto magnetized NSs with the main goal to understand if and under which circumstances a super-Eddington luminosity can be produced. Indeed, as it will be seen later on, the luminosity overcomes the Eddington one.

The very first investigation of whether a strongly magnetized neutron star could be capable of emitting above its Eddington limit, was presented by Basko & Sunyaev (1976) [Basko & Sunyaev(1976)]. Their model, however, was primarily focused on the effects of the presence of an accretion column and a radiative shock, neglecting the contribution of the strong magnetic field (e.g. in the reduction of plasma opacities). Thus the maximum luminosity that they found was increased only by a factor of few above the limit.

After this first attempt, Lyubarskii & Syunyaev (1988) [Lyubarskii & Syunyaev(1988)] extended the last model calculating the structure of the region below the shock in two dimensions, providing the basis for the more recent models.

As anticipated in the previous chapters, the accretion in this case is far from being spherical, due to the presence of a strong magnetic field, thus matter accretes only onto a small fraction of the total star surface.

3.1 Accretion onto NS magnetic poles

Defining the accretion column structure of a neutron star is not an easy task, because the basic physical processes involved are not well understood. In particular, in this case, we have to deal with very extreme physical conditions on the stellar surface, such as: supersonic free-fall velocities $\sim c/2$, magnetic field of the order $\sim 10^{13}$G, and luminosities $\sim L_{Edd}$.

In early times, for instance, it was unclear if the accretion column was an "hollow" or a "filled" cylinder. Moreover, it is far from established when or if a shock occurs, what kind it is and what is the exact process which forms it. The main reason for such doubts is that the deflection mean free path λ_d of plasma particles coming from the disk (i.e. the distance traveled by particles before

being deflected through interactions with particles on the neutron star surface) is very large, even larger than the star radius:

$$\lambda_d \geq 5 \times 10^9 \text{cm} \gg \text{R}_* \cong 10^6 \text{cm}, \tag{3.1}$$

for protons with free-fall energies. Thus a collisional shock is not possible. However, this does not mean that another kind of shock cannot form. For example, a region of discontinuity, with thickness much smaller than deflection mean free path might form, producing a *collisionless* shock.

The collisionless shock physics is not well understood, and because of our ignorance of how such shocks work, we do not know the conditions for their formation. So, in general, for accretion onto neutron stars, one should take into account both types of accretion: with and without shock. An additional complication is given by the fact that for modest accretion rates the radiation pressure due to the accretion luminosity will become important Furthermore, problems come out also from the fact that accretion takes place in a highly magnetized environment, so each physical process must be described accordingly.

It does not come as a surprise that a detailed treatment of the radiative transfer problem has been given only for simple geometries, while models for the column structure simplify it. The main purpose is to combine all these effects, in order to predict the observational data.

3.2 Basko & Sunyaev model

As originally introduced, the first model for accretion onto a magneticed NS was that of Basko & Sunyaev (1976)[Basko & Sunyaev(1976)], it is based on the assumption that, outside the Alfvén surface (where we can neglect the influence of the stellar magnetic field on the accreting material) accretion can proceed in two cases: spherically-symmetric radial infall, and disk accretion. The best choice would be the second, since it is the results of the Roche lobe overflow (chapter 1), a scenario needed in order to have large mass transfer rates in binary systems.

At the Alfvén radius (r_A) the pressure of magnetic field (a dipole field) destroys the disk. It is assumed that at this distance the plasma continues to accrete following the magnetic field lines of the star, falling towards the magnetic poles. Because of the low resistivity, the depth to which the plasma penetrates into the dipole field is small compared to the Alfvén radius and, as a consequence, the accretion flow near the surface of the compact object will be similar to a thin wall of a funnel.

At the stellar surface the cross-section of the accretion channel is a thin annular arc having the radius $a_0 \sim 0.1R$, where R is the star radius, the length $l_0 \sim a_0$, and the thickness $d_0 \ll a_0$. Numerically speaking $l_0 \approx 2 \times 10^5$cm, $d_0 = 5 \times 10^3$cm, which corresponds to a penetration depth $\approx 0.1 r_A$ at the Alfvén radius.

If, instead, we consider a spherically-symmetric infall, then matter will occupy the whole cavity of the funnel. This case, despite the different accretion column geometry, can be described by the same solution of the previous one (thin accretion wall), changing only the values of some parameters (see figure

3.1).

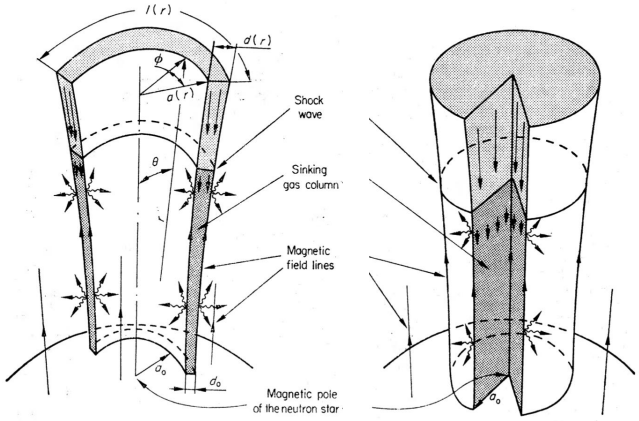

(a) (b)

Figure 3.1: Accretion flow geometries. Panel (a) shows the case in which material accretes inside narrow walls of magnetic funnel, $d_0 \ll a_0$. Panel (b) shows the second possibility, in which material fills the whole cavity of the funnel. The basic case adopted is that described in panel (a) [Basko & Sunyaev(1976)].

The hypothesis that the accreting plasma is frozen in the magnetic field can be invalid, and one can imagine a situation where the plasma falls into a narrow axisymmetric funnel and does not contain any external magnetic field, which would be the case with the already discussed solid accretion funnel. However, an external magnetic field should always be present in a column of sinking gas, as the sinking gas locally releases its gravitational energy. This energy is then carried by radiative diffusion towards the side walls of the column. At this point the resultant transversal radiation pressure gradient is balanced by the opposing magnetic pressure gradient:

$$P_m = \frac{B^2}{8\pi}. \tag{3.2}$$

Thus, considering the above argument, from now on the hollow axisymmetric channel scenario is assumed. The interior of the funnel contains only radiation with a constant energy density, without any matter or magnetic field. In any case, this is just a particular case of the one depicted in the figure 3.1a.

The model distinguish two main cases for the accretion process above the neutron star surface. The one with *low accretion rates* and the other with *high accretion rates*.

3.2.1 Low accretion rates

First, Basko & Sunyaev define the quantity:

$$L_t \equiv \dot{M}\frac{GM}{R} \tag{3.3}$$

which is equivalent to the mass accretion rate $\dot{M}$.
If L_t is smaller than L^*, defined as

$$L^* = 2\frac{l_0 cGM}{R^2\kappa} = 4 \cdot 10^{36} \left(\frac{\sigma_T}{\sigma_s}\right) \left(\frac{l_0}{2 \cdot 10^5 cm}\right) \left(\frac{R}{10^6 cm}\right)^{-1} \left(\frac{M}{M_\odot}\right) \text{ergs}^{-1}, \tag{3.4}$$

where σ_s is the scattering cross-section, one can distinguish two zones in the accretion column:

(i) free-fall zone, which extends almost down to the neutron star surface. Here the radiation density is $u = 0$ and the gas velocity $v(r) = -(2GM/r)^{1/2}$.

(ii) shock zone, has a height of the same order of magnitude as d_0 (if in the case of a solid axisymmentric channel, of the same order of a_0), much lower than R; this region contains a radiation field of density $u \sim \rho(R)v^2(R)$.

Basically what happens is that the infalling material loses part of its kinetic energy while crossing the shock zone: the escaping photons slow down the infalling electrons through scattering, and electrons, in turn, slow down protons through Coulomb interaction. When radiation pressure dominates an extended shock structure develops, and this recalls the structure already discussed.

The fraction of the lost kinetic energy in the shock decreases with decreasing L_t, in other words the velocity v_0 of the gas at the bottom of the accretion column vanishes at $L_t = L^*$.

The luminosity L^* has a precise physical meaning; when L_t equals L^* a radiative shock arises above the neutron star surface, at a height of the order of d_0 (or a_0 for a solid accretion funnel), and this is the distance at which the infalling matter is stopped by the emergent radiation.

In other words, in the case of a low accretion rate, the total energy flux vanishes at the stellar surface, as the kinetic energy flux of the infalling material is completely balanced by the energy flux of the emerging radiation.

3.2.2 High accretion rates

If $L_t \gg L^*$, all the kinetic energy of the infalling gas is lost in the radiative shock, being converted into radiation. Simultaneously, when $L_t \gg L^*$, the transverse optical depth τ_t becomes much greater than unity, and consequently just a small fraction of the accretion energy can be radiated by the shock zone side walls. From this, Basko & Sunyaev concluded that the shock rises above the stellar surface as L_t increases, and below the shock a large sinking zone appears. Here, the gas velocity is small while the radiative energy density is high; the gas slowly decelerates releasing its gravitational energy and emitting it laterally. Nevertheless, in this case there is no force other than gravity that could balance the radiative pressure gradient, so the luminosity L_X could not exceed the Eddington one.

The total amount of energy L_X radiated per unit time by the sides of the gas column increases with L_t. However, can be achieved a sort of saturation condition when $L_t \sim L^{**}$ (where L^{**} is the maximum X-ray luminosity). At this point the rise of the shock stops, and the X-ray luminosity L_X reaches its peak value: $\sim (2-4)L^{**}$. The maximum luminosity turns out to be

$$L^{**} = 2\frac{l_0 cGM}{d_0\kappa} = \frac{l_0}{2\pi d_0} L_{Edd} = 3 \cdot 10^{38} \left(\frac{l_0/d_0}{40}\right) \left(\frac{\sigma_T}{\sigma_s}\right) \left(\frac{M}{M_\odot}\right) ergs^{-1}. \tag{3.5}$$

It is clear from the equation (3.4) that L^{**} is sensitive to the geometry of the accretion column. In the case of a solid axisymmetric funnel $L^{**} = 1/4 L_{Edd}$. Thus one can see how the maximum luminosity, in the model of Basko & Sunyaev, exceeds the Eddington limit just by a factor of a few.

3.2.3 Reduction of opacity

Still from equation (3.4), it is clear that the limiting luminosity L^{**} is inversely proportional to the opacity $\kappa = \sigma_s/m_p$. This means that any mechanism that allows for a reduction of the scattering cross-section, with respect to the Thomson one, will increase the maximum luminosity achievable by an accreting neutron star. Two possibilities have been proposed in this respect.

In case of a strong magnetic field, the scattering cross-section for X-mode photon decreases at frequencies $\nu \ll \nu_B = eB/2\pi m_e c$, since $\sigma_s \approx (\nu/\nu_B)^2 \sigma_T$. In any case, this effect becomes important only in case of a magnetic field strength of $B \geq 10^{14}$G. In fact, the main part of the X-ray flux is emitted from the base of the accretion column, where the internal temperature for $L_X \sim L^{**}$ is $T_{in} \sim (3B^2/8\pi a)^{1/4}$ ($a = 7.56 \times 10^{-15} erg\ cm^{-3}\ K^{-4}$) and so:

$$\left(\frac{\nu}{\nu_B}\right)^2 \simeq \left(\frac{kT_{in}}{h\nu_B}\right)^2 \simeq \frac{2 \times 10^{14} G}{B}. \tag{3.6}$$

We can note that if $B > 2 \times 10^{13}$G the ratio $(\nu/\nu_B)^2$ starts to decrease as a consequence of the fact that the internal temperature does not increase anymore, due to neutrino losses.

At the same time if the magnetic field strength is higher than 10^{13}G, then the temperature in the accretion column becomes $kT_{in} \geq m_e c^2$, and the Klein-Nishina scattering cross-section should be taken into account. As a consequence of this, the decrease of the scattering cross-section let to a significant increase of the maximum luminosity L^{**}.

3.3 Lyubarskii & Syunyaev model

Lyubarskii & Sunyaev (1988) [Lyubarskii & Syunyaev(1988)] extended the model of Basko & Sunyaev, computing the shape of the column in two dimensions, so analysing the trend of the radiation pressure gradient not only along the column but also across it. Finding, indeed, not a column with a cylindrical wall, but a column with a triangular vertical cross-section.

3.3.1 Formation of the accretion column

For both models (Basko & Syunyaev (1976) and Lyubarskii & Syunyaev (1988)) the starting point is the accretion of plasma particles towards the magnetic poles of the star, moving along the surface of a cylindrical segment formed by the field lines. Defining the critical accretion rate:

$$\dot{M}^* = 2\frac{lc}{\kappa}, \tag{3.7}$$

where l is the cylinder base length and κ the opacity, if the accretion rate is greater than the one in the equation (3.7), then the radiation produced would

be such intense that its pressure could halt the infall of material: when $\dot{M} \sim \dot{M}^*$ the plasma flow will be braked by a radiative shock that forms above the stellar surface, and that shock could rise above the star surface if the rate $\dot{M} \gg \dot{M}^*$. For such conditions, the gas decelerated by the shock will gradually settle downwards in an accretion column, radiating its stored energy by the sides of the latter. The transverse radiative flux emitted by the column largely exceeds the vertical one, this because along the radial direction, the gravitational force inside the column is completely balanced by the radiation pressure, so the vertical radiative flux is given by the Eddington value

$$Q_{\parallel} = \frac{GM}{R^2}\frac{c}{\kappa}, \tag{3.8}$$

where M and R are the mass and radius of the neutron star. Instead, since the column thickness d is much smaller than its height H, the transverse component of the radiative flux is

$$Q_{\perp} = \frac{H}{d}Q_{\parallel} = \frac{H}{d}\frac{GM}{R^2}\frac{c}{\kappa}. \tag{3.9}$$

thus, higher than the vertical component. Supposing that the height of the column could reach values comparable to the neutron star radius $H \sim R$, the corresponding X-ray maximum luminosity that they found is of the order:

$$L^{**} = 2\frac{l}{d}GM\frac{c}{\kappa} = 10^{39}\left(\frac{l/d}{50}\right)\left(\frac{M}{M_{\odot}}\right)\text{erg/s}. \tag{3.10}$$

Also in this case, from the equation (3.10), it can be seen that the maximum luminosity highly depends on the accretion column geometry, since if the ratio l/d is higher enough, the luminosity can exceed the Eddington limit.

3.3.2 Shape of the accretion column

Lyubarskii & Syunyaev (1988) showed that the shape of the column is different from the one predicted by Basko & Syunyaev (1976), since its height depends on the distance from the column axis. As a consequence, the infalling particles are decelerated by the shock at different heights along the horizontal column cross-section, and the radiation pressure which supports the column will fall sharply towards the edges of the emitting layer. The resulting shape of the vertical column section is a sort of triangle, instead of a rectangle, as in [Basko & Sunyaev(1976)] (see figure 3.2).

The radiation seen by the observer is not that directly emitted by the column: plasma is opaque to scattering, so it will intercept the radiation coming from the column, re-emitting it towards the neutron star surface. Thus, the observer will see the radiation reflected by the surface of the star, heated by the radiation re-emitted by the plasma.

For simplicity, in their model, Lyubarskii & Syunyaev adopted, as scattering cross-section, the Thomson one with an associated opacity: $\kappa = \sigma_T/m_p$.

The proof for that shape for the accretion channel was given starting from the equation (3.9), which indicates that at optical depth τ the radiative energy density is

$$\varepsilon = \frac{3Q_{\perp}\tau}{c} = \frac{3H}{\kappa d}\frac{GM}{R^2}\tau. \tag{3.11}$$

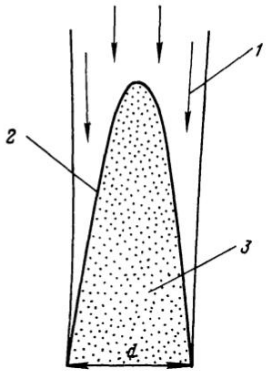

Figure 3.2: Cross-section of the accretion column: 1) free-falling plasma; 2) the deceleration zone; 3) gradual settling [Lyubarskii & Syunyaev(1988)].

Then one has to consider that the radiation pressure needs to balance the weight of the material above the accretion column:

$$\frac{3H}{\kappa d}\frac{GM}{R^2}\tau = \frac{GM}{R^2}\rho h, \tag{3.12}$$

where ρ is the matter density and h is the column height corresponding to the optical depth τ, measured from the lateral surface. From equations (3.11) and (3.12) we obtain

$$h = \frac{H\tau}{\kappa\rho d} \tag{3.13}$$

remembering that H is the column height along the central axis. Let us define a dimensionless mass accretion rate $\dot{m}$:

$$\dot{m} = \frac{GM}{R}\frac{\dot{M}}{L^{**}} = \frac{\kappa\dot{M}d}{2Rlc}, \tag{3.14}$$

from this equation and the continuity one:

$$\dot{M} = 2\rho v d l, \tag{3.15}$$

we can express the density in terms of $\dot{m}$ and the speed v, from which

$$h = \frac{1}{\dot{m}}\frac{H}{R}\frac{v}{c}\tau d. \tag{3.16}$$

Since at the column boundary ($\tau \sim 1$) $H \sim \dot{m}R$, one has:

$$h \sim d \ll H. \tag{3.17}$$

The radiative energy density decreases sharply toward the edges of the column, so the peripheral height is negligible, and this proves that the shock height is not constant along the base of the column. Essentially, what happens is that particle infalling along the column central plane will be decelerated by the shock at height H, settling then gradually, and radiating their energy by the sides. Is then this radiation that decelerates particles coming in along the column's edge.

3.4 More recent developments

From the models of Basko & Sunyaev (1976), and Lyubarskii & Syunyaev (1988), it can be seen that the configuration of the emitting region highly depends on the mass accretion rate $\dot{M}$. When the luminosity is low, the X-ray emission is produced by the hot spots at the stellar surface, and as the luminosity exceeds the critical value (which is $\sim 10^{37}$erg/s), a radiative shock starts to rise above the star surface, leading to the formation of an accretion column, and providing the possibility to exceed the Eddington luminosity.

Mushtukov et al. (2015) [Mushtukov et al.(2015)] reexamined the problem by taking into account the possible consequences of the presence of a strong magnetic field. It has been considered for the first time the exact Compton scattering cross-section in strong magnetic fields. They computed the structure of the accretion column, and an upper limit for the neutron star luminosity, which turns out to be close to 10^{40}erg/s. That value coincides with the location of a cut-off in the luminosity function of high mass X-ray binaries [Mineo et al.(2012)], indicating that a large fraction of those sources are probably accreting magnetized neutron stars. They also found that high mass accretion rates require a very high magnetic field strengths.

3.4.1 Multipolar magnetic field

Mushtukov et al. (2015) model does not take into account problems with the propeller effect in using pure dipole strong magnetic fields. In fact, for sources with a small spin period, such fields would place them in the propeller regime, halting the accretion of material onto the magnetic poles of the star, because of the transfer of angular momentum at the magnetospheric radius (as seen in chapter 1).

To overcome this problem it was proposed [Israel et al.(2017)] that the topology of the magnetic field should be changed from a pure dipole to a multipolar configuration, in which, a part from the dipole component, were taken into account also higher order multipole moments of the magnetic field. The practicality of such hypothesis was in the fact that higher order multipole moments decay with the radial distance from the NS more rapidly than the dipole component (which scales as $\sim 1/r^3$). As a consequence of this, the very high strength of the magnetic field is just local, on the stellar surface, because moving towards the magnetospheric radius it is only given by the dipole component, since other moments are zero.

In support of this hypothesis there are observational data from the magnetar SGR 0418+5729 [Tiengo et al.(2013)], the isolated neutron stars RX J0720.4-3125 and J1308.6+2127 ([Borghese et al.(2015)], [Borghese et al.(2017)]), and from the millisecond pulsar PSR J0030+0451 [Bilous et al.(2019)].

Based on this requirement, the previous model [Mushtukov et al.(2015)] was revised in the work of Brice et al. (2021) [Brice et al.(2021)], in which is used a multipolar magnetic field, more precisely they used the octupole moment. In this way the problem due to the propeller effect is avoided, and the strength of the magnetic field on the surface is high enough to allow for a sufficient opacity reduction, which in turn leads to the release of a substantial amount of energy.

3.4.2 Accretion column

We start considering the model of Basko & Sunyaev (1976)[Basko & Sunyaev(1976)], in which free plasma particles are efficiently decelerated by a radiative shock above the NS surface, and below it particles slowly sinks towards the surface, releasing their gravitational potential energy in the form of X-ray radiation. This region is identify as the sinking region.

Basic equations

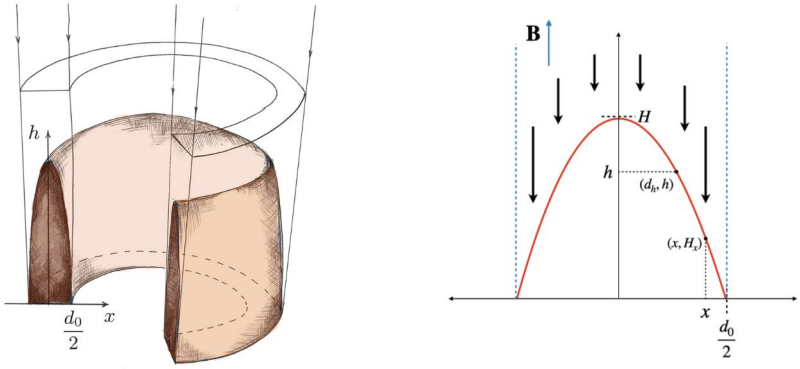

(a) (b)

Figure 3.3: Accretion column structure. Panel (a) shows the base of the column, i.e. an annular arc with thickness d_0 and length l_0, the height of the radiation-dominated shock is not constant, but varies across the base, and the maximum height achieved by the column (i.e. the settling flow) is in the center ($x = 0$) [Mushtukov et al.(2015)]. Panel (b) illustrates a vertical cross section of the column [Brice et al.(2021)].

In order to describe the structure and geometry of the accretion column, we adopt an orthonormal coordinate system (x,h), where h is along the magnetic field lines, which have been approximated as straight lines (since near the magnetic poles the curvature is negligible), while x is orthogonal to h. The center of the accretion column is defined at $x = 0$, while $h = 0$ corresponds to the neutron star surface.

The column (or radiative shock) maximum height is indicated by H, its footprint is an annulus with arc length l_0 and width d_0 (see figure 3.3). More generally speaking H_x is the height of the shock corresponding to the width x on the base, and d_h is the width of the sinking region corresponding to a certain h above the surface; the area of the column base is given by $S_D = l_0 d_0$.

In the following we will introduce a number of simplifying assumptions which are required to make the problem tractable. Let us consider that inside the sinking region there is a steady state flow, with velocity directed along the magnetic field lines. We assume further that the radiation pressure, P_{rad}, dominates over the gas pressure, P_{gas}, and that, according to Mushtukov et al. (2015)[Mushtukov et al.(2015)], the density and velocity profiles are independent on x, coinciding with the center column profiles.

It is, finally, assumed that the energy flux is dominated by the radiative one, which is the sum of a component directed vertically along the field lines, $F_{\parallel}$, and another one perpendicular to them, $F_{\perp}$.

According to such assumptions one can introduce the equations of continuity, momentum and energy as follows:

$$\rho v = \frac{\dot{M}}{2S_D}, \tag{3.18}$$

$$v\frac{\partial v}{\partial h} + \frac{1}{\rho}\frac{\partial P_{rad}}{\partial h} + \frac{GM}{(R+h)^2} = 0, \tag{3.19}$$

$$\frac{\partial F_{\parallel}}{\partial h} + \frac{\partial F_{\perp}}{\partial x} = 0, \tag{3.20}$$

where ρ is the plasma density, v is the velocity of plasma particles, $\dot{M}$ is the mass accretion rate, M and R are the mass and the radius of the NS, respectively. The parallel and orthogonal component of the flux are expressed as

$$F_{\parallel} = -\frac{c}{\kappa_{\parallel}\rho}\frac{\partial P_{rad}}{\partial h} + P_{rad}v + uv + \rho v\left(\frac{v^2}{2} - \frac{GM}{R+h}\right), \tag{3.21}$$

$$F_{\perp} = -\frac{c}{\kappa_{\perp}\rho}\frac{\partial P_{rad}}{\partial x}, \tag{3.22}$$

where u is the radiation energy density, and $\kappa_{\parallel}$ and $\kappa_{\perp}$ are the angle and energy averaged Rosseland mean opacities, the first parallel to the magnetic field lines and the second orthogonal to them. Since in the sinking region (under the shock) the flow is decelerated up to a velocity which is much lower than the free-fall one,

$$\frac{\partial}{\partial h}\left(\frac{v^2}{2}\right) \ll -\frac{GM}{(R+h)^2}, \tag{3.23}$$

in the vertical direction the hydrostatic equilibrium can be assumed, and equation (3.19) simply becomes:

$$\frac{\partial P_{rad}}{\partial h} = -\rho\frac{GM}{(R+h)^2}. \tag{3.24}$$

Considering that the energy flux is dominated by the radiative one, equations (3.21) and (3.22) can be written as

$$\frac{\partial P_{rad}}{\partial h} = -\rho\kappa_{\parallel}\frac{F_{\parallel}}{c} \tag{3.25}$$

$$\frac{\partial P_{rad}}{\partial x} = -\rho\kappa_{\perp}\frac{F_{\perp}}{c}. \tag{3.26}$$

These last equations, upon integration, give the radiation pressure distribution within the sinking region, and hence its total structure. Recalling equation (3.24), we obtain:

$$F_{\parallel}(x,h) = \frac{c}{\kappa_{\parallel}}\frac{GM}{(R+h)^2}, \tag{3.27}$$

which is the local Eddington flux, $F_{Edd}(x,h)$. The perpendicular flux, instead, can be obtained integrating the equation (3.20) along x, assuming that $\partial F_{\parallel}/\partial h \approx$ constant in x. In this way we obtain:

$$F_{\perp} = F_{\perp,esc}(h)\frac{2x}{d_h}, \tag{3.28}$$

where $F_{\perp,esc}(h)$ is the perpendicular flux, corresponding to the height h, escaping from the sinking region. To obtain the previous expression we have taken into account the boundary conditions:

$$F_{\perp}(x=0,h)=0,\ F_{\perp}(x=d_h/2,h)=F_{\perp,esc}(x,h). \tag{3.29}$$

Now, we can integrate (3.25) and (3.26), along h the first, and along x the second:

$$P_{rad,\parallel}(x,h) = \int_h^{H_x}\rho\frac{GM}{(R+y)^2}dy + \frac{2}{3}\frac{F_{Edd}(H_x)}{c}, \tag{3.30}$$

$$P_{rad,\perp}(x,h) = \frac{F_{\perp,esc(x,h)}}{c}\left[\frac{2}{d_h}\int_x^{d_h/2}\rho\kappa_{\perp}zdz + \frac{2}{3}\right], \tag{3.31}$$

where $P_{rad,\parallel}$ and $P_{rad,\perp}$ are the radiation pressure obtained from the previous integration, in which we used the following boundary conditions:

$$P_{rad,\parallel}(x,h=H_x) = \frac{2}{3}\frac{F_{\parallel}(x,H_x)}{c} = \frac{2}{3}\frac{F_{Edd}(H_x)}{c}, \tag{3.32}$$

$$P_{rad,\perp}(x=d_h/2,h) = \frac{2}{3}\frac{F_{\perp,esc}(h)}{c}. \tag{3.33}$$

Density profile

Looking at the equations (3.30) and (3.31), it is clear that both depend on the density ρ. To obtain the density profile we can use the continuity equation (3.18), but only if the velocity profile is known. According to Mushtukov et al. (2015)[Mushtukov et al.(2015)], the velocity profile can be approximated as a power-law $v \propto h^{\xi}$, taking $\xi = 1$.

As mentioned above, it is assumed that the velocity profile does not change along x, so $v(x,h) = v(h)$, in addition, the plasma particles are greatly decelerated so that their velocity goes from the free-fall value (v_{ff}) above the shock (at height H) to a value $\sim v_{ff}/7$ below it (loosing everything except $\sim 1/50$ of their kinetic energy). Another additional condition is that the velocity vanishes at the surface of the neutron star. Thus, at an height h above the star surface, the velocity can be expressed as

$$v(h) = \frac{v_{ff}}{7}\left(\frac{h}{H}\right)^{\xi} \tag{3.34}$$

where $v_{ff} = \sqrt{2GM/(R+H)}$ above the shock. Now, we can derive the density profile, combining the continuity equation (3.18) and the velocity profile (3.34):

$$\rho(h) = \frac{L_{acc}}{2S_D}\left(\frac{GM}{R}\right)^{-3/2}\left(\frac{49}{2}\right)^{1/2}\left(1+\frac{H}{R}\right)^{1/2}\left(\frac{H}{R}\right)^{\xi}\left(\frac{h}{R}\right)^{-\xi}, \tag{3.35}$$

where L_{acc} was introduced before in equation (1.31). From eq. (3.35) we see that when $h = 0$ the density diverges, and the previous assumptions become unsuitable close to the stellar surface. Furthermore, the gas pressure, at some point, will start to dominate over the radiation one. To avoid this, the numerical calculations are truncated just above the surface, where $P_{rad} \approx P_{gas}$.

Geometrical parameters

Equations (3.30) and (3.31) present as extremes of integration H_x and d_h, while the expression for the density profile depends on S_D ($S_D = l_0 d_0$). All these parameters depend on the accretion column base geometry, that in turn depends on the details of the disk-magnetosphere interaction. One of the simplest models that describes such interaction is that of Ghosh & Lamb (1978)[Ghosh & Lamb(1978)], in which the disk is not definitely truncated at the magnetospheric radius, but matter can penetrate up to a certain distance, and the width of that boundary region is much smaller than the magnetospheric radius.

The crucial parameters entering in this disk-magnetosphere interaction model are two: the magnetospheric radius R_m, and the penetration depth P_m. The first is given by

$$R_m \approx 7 \times 10^7 \Lambda M^{1/7} R_6^{10/7} B_{d,12}^{4/7} L_{39}^{-2/7} \text{cm}, \tag{3.36}$$

where Λ is a dimensionless, which depends on the accretion mode, and its canonical value in this model is: $\Lambda = 0.5$. Then, R_6 is the radius of the NS expressed in units of 10^6cm, L_{39} the accretion luminosity expressed in units of 10^{39}erg s^{-1}, and $B_{d,12}$ the strength of the dipole component of the magnetic field on the stellar surface, expressed in units of 10^{12}G. We take into account just the dipole component, since at the distance at where the interaction between the disk and the magnetosphere occurs, the effects of higher order multipole components are negligible (it is $R_m = 100$R).

The penetration depth, P_m, should be of the order of the disk height for a geometrically thin disk [Ghosh & Lamb(1978)]. However in some cases the thin disk approximation could not be valid and a geometrically thick disk seems to work better. In this case, however, taking $P_m \approx$ the disc height implies that the former can be even greater than R_m, which is not physically possible. To avoid this issue, we introduce a dimensionless parameter, $\zeta \equiv P_m/R_m$, which must be lower than a maximum value ζ_{max}. In the actual calculations we took $\zeta_{max} = 0.2$.

Once the penetration depth is set, the accretion flow is constrained by the shape of the magnetic field lines, which determines the accretion base width d_0, and length l_0. The equation of the magnetic field lines cannot be expressed analytically for a general topology of the field, so it is computed numerically (see figure 3.4 for the result). The footprint of the magnetic field lines (passing through the disk-magnetosphere boundary region), on the NS surface,is given by an annulus with width d_0, centered on the magnetic axis, and length l_0.

The sinking region geometry, also, depends on the shape on the magnetic field lines in the region $0 \leq h \leq R$. It is important, especially when we want to compute the sinking region width d_h, and the accretion column area above the NS surface S_D.

To compute S_D, we start from the expressions of l and d, which are the length and the width of the accretion column above the surface at a given height h. In

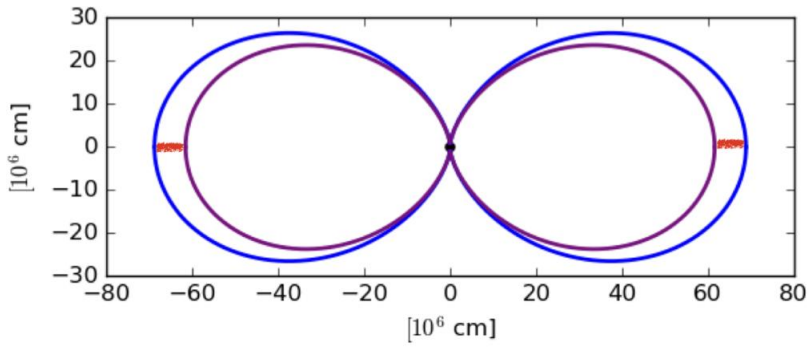

Figure 3.4: A 2D plot of the magnetic field lines, computed numerically. The blue lines cross the disk at the magnetospheric radius, while purple ones in the inner radius of the boundary region. The red segments show the part of the disk that penetrates the magnetosphere [Brice et al.(2021)].

case of dipole magnetic field:

$$d = d_0 \left(1 + \frac{h}{R}\right)^{3/2}, \; l = l_0 \left(1 + \frac{h}{R}\right)^{3/2}. \tag{3.37}$$

In the case of a multipolar magnetic field a numerical computation is needed, but we can still rely on this parametric formulas:

$$d = d_0 \left(1 + \frac{h}{R}\right)^{\alpha}, \; l = l_0 \left(1 + \frac{h}{R}\right)^{\beta}, \tag{3.38}$$

where α and β are two parameters which depends on the topology of the magnetic field, and differs considerably with respect to those in (3.37). At this point the area is given by

$$S_D = l_0 d_0 \left(1 + \frac{h}{R}\right)^{\alpha+\beta}. \tag{3.39}$$

Opacity

Another important dependence in the equations (3.30) and (3.31), is that on the Rosseland mean opacities: $\kappa_{\parallel}$, and $\kappa_{\perp}$. These are angle and frequency averaged opacities, the first parallel to the direction of the magnetic field lines, and the second perpendicular to it. Since we are dealing with a strongly magnetized plasma, we have to take into account that radiation is polarized in two different normal modes: the extraordinary (X) mode, and the ordinary (O) one, which present different polarization and opacity properties [Harding & Lai(2006)].

Let us consider a pure scattering medium, and compute the electron scattering opacities in the limit of strong magnetic fields and in the Thomson approximation. First, we assume that the plasma in the sinking region is cold ($k_B T \ll mc^2$, where m is the mass and T the temperature of the electrons). Second, we refer to a fully ionized solar mix plasma, with a mean molecular

weight $\mu_e = 1.17$, using the expressions for the frequency and angle dependent electron scattering opacities of the two modes ([Kaminker et al.(1982)], [Zane et al.(2000)]).

The Rosseland mean opacities parallel and perpendicular are:

$$\frac{1}{\kappa^1_{\parallel}} = \frac{\int_0^\infty \frac{\partial B_E(T)}{\partial T} dE \int_0^1 d\mu 3\mu^2 \frac{1}{k^i(E,\mu)}}{\int_0^\infty \frac{\partial B_E(T)}{\partial T} dE}, \tag{3.40}$$

$$\frac{1}{\kappa^1_{\perp}} = \frac{\int_0^\infty \frac{\partial B_E(T)}{\partial T} dE \int_0^\pi d\phi \int_0^1 d\mu_\perp \frac{3}{\pi}\mu_\perp^2 \frac{1}{k^i(E,\mu)}}{\int_0^\infty \frac{\partial B_E(T)}{\partial T} dE}. \tag{3.41}$$

$k^i(E,\mu)$ is the electron scattering opacity integrated all over the possible directions of outgoing photons (index i indicates the polarization mode, $i = 1$ for the X-mode, $i = 2$ for the O-mode), $B_E(T)$ is the Planck function, E is the energy of the photon, μ is the cosine of the angle between the photon propagation direction and the magnetic field lines, and $\mu_\perp$ is the cosine of the angle between the photon propagation direction and the direction perpendicular to the magnetic field lines.

For mixed polarization modes the effective opacity is

$$\frac{1}{\kappa} = \frac{f}{\kappa^1} + \frac{1-f}{\kappa^2}, \tag{3.42}$$

where f is the fraction of X-mode photons, and in the following we assume only X-mode photons ($f = 1$).

It is important to note that both opacities (3.40) and (3.41) are dependent on the plasma temperature. To obtain the latter, since the sinking region is optically thick, we can first assume that the plasma is in thermal equilibrium with the radiation field, and then using the Eddington approximation and the blackbody approximation we can link the temperature with the radiation pressure:

$$P_{rad} \approx \frac{aT^4}{3} \tag{3.43}$$

where a is the blackbody constant. So we can compute the Rosseland mean opacities only if the radiation pressure is known.

These calculations, for the Rosseland mean opacity, hold until the approximation of cold plasma works (i.e. the thermal motions of electrons is negligible with respect to the phase velocity of the wave).

Final estimates

Taking a constant density profile $\rho(h) = \rho$, and a constant parallel and perpendicular opacities, we can obtain an analytical expression of the radiation pressure:

$$P_{rad,\parallel}(x,h) = \rho\frac{GM}{R}\left[\frac{H_x/R - h/R}{(1+h/R)(1+H_x/R)} + \frac{2}{3}\frac{1}{\rho R\kappa_\parallel}\frac{1}{(1+H_x/R)^2}\right] \tag{3.44}$$

$$P_{rad,\perp}(x,h) = \frac{F_{\perp,esc}(h)}{c}\left[\rho\kappa_\perp d_h/4(1-(2x/d_h)^2) + 2/3\right], \tag{3.45}$$

where only H_x and d_h are to be determined. The quantity $\rho\kappa_\parallel R$ is approximately the vertical optical depth in the sinking region, instead $\rho\kappa_\perp d_h/2$ is the horizontal one at a certain height h. From equations (3.44) and (3.45), we compute their values at $x = 0$ and $h = 0$, and equating them the expression for the normalized escaping flux can be derived:

$$\frac{F_{\perp,esc}(h=0)}{c} = \rho\frac{GM}{R}\left[\frac{\frac{H/R}{(1+H/R)} + \frac{2}{3}\frac{1}{\rho R\kappa_\parallel}\frac{1}{(1+H/R)^2}}{\rho\kappa_\perp d_h/4 + 2/3}\right] \tag{3.46}$$

For the shape, once we have obtained the radiation pressure (parallel and perpendicular), we use $P_{rad,\parallel}(x, h = 0) = P_{rad,\perp}(x, h = 0)$, assuming that $H_x/R \ll 1$, to obtain

$$\frac{H_x}{R} \propto -x^2. \tag{3.47}$$

In this simplified case, the shape of the shock results to be nearly quadratic close to the NS surface, becoming less quadratic close to the top.

Integrating the escaping flux we obtain, finally, the luminosity of the column, which is

$$L = 4l_0\int_0^H \left(1+\frac{h}{R}\right)^\beta F_{\perp,esc}(h)dh, \tag{3.48}$$

because of the presence of d_h in $F_{\perp,esc}(h)$, which depends on h, the integral is not solvable analytically, but it is possible to derive a lower limit, imposing $d_h \approx d$, i.e. approximating the accretion column horizontal optical depth with its maximum value. Recalling that the column is optically thick ($\rho\kappa_\parallel R \gg 1$ and $\rho\kappa_\perp d_h \gg 1$) the lower limit turns out to be:

$$L \geq \frac{4}{\pi}\left(\frac{l_0}{d_0}\right)\left(\frac{\kappa_T}{\kappa_\perp}\right) f\left(\frac{H}{R}\right) L_{Edd}, \tag{3.49}$$

where the function $f(H/R)$ is

$$f\left(\frac{H}{R}\right) = \frac{1}{1+H/R}[(1+H/R)\log(1+H/R) - H/R]. \tag{3.50}$$

The function f grows logarithmically for large H/R ratios, and quadratically if $H \ll R$; this means that the luminosity of the column increases slowly for higher H [Mushtukov et al.(2015)].

It is important to stress that equation (3.49) resembles that of Basko & Sunyaev (1976) (3.4), in which we found a dependence on the geometrical parameters l_0 and d_0, and on the ratio between the Thomson scattering cross-section and the real scattering cross-section in the column. In this case (3.49), instead of the cross-sections, the dependence is on the ratio between the Thomson scattering opacity and the orthogonal opacity $\kappa_T/\kappa_\perp$, and because of the strong magnetic field, the opacity inside the accretion column is significantly reduced, so the ratio increases, allowing the luminosity to exceed by many orders of magnitude the Eddington value. Exceeding the value found by Basko & Sunyaev.

As stated before, the radiation pressure equations (3.30) and (3.31) depends on the opacities $\kappa_\parallel$ and $\kappa_\perp$, that in turn depend on the temperature, which depends (see equation (3.43)) on the radiation pressure. Hence, for the non-linearity of the radiation pressure equations, the only way to compute P_{rad} is through an iterative method.

3.4.3 Results: effects of the magnetic field strength and topology

The aim of the model is to be able to explain the higher luminosities of PULXs. After having derived a lower limit for the luminosity, let us now focus on the dependencies of this on the column geometry (length and width), the opacity, and the column height. In particular, let us now explore how variations in the magnetic filed strength and topology can affect such quantities.

Variations in the column base variables

As mentioned above, the magnetic field used in this model is not a pure dipole field but it presents also a multiple moment, the octupole one. In order to separate the changes in opacity from those in the column geometry, the octupolar component strength has been made to vary, keeping fixed the value of l_0 and d_0 to those computed for a pure dipole field, and neglecting the curvature of magnetic field lines.

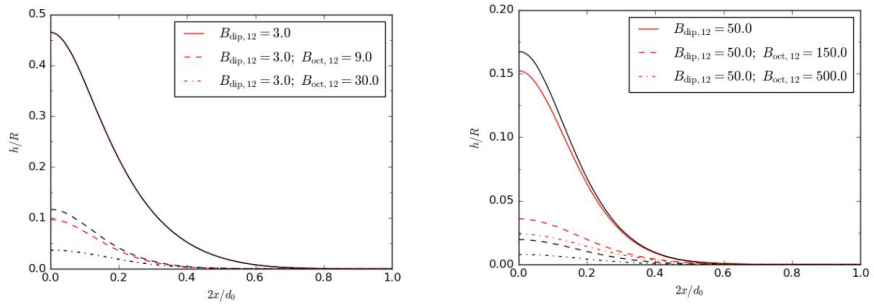

(a) (b)

Figure 3.5: Vertical cross section variation. In the two panels we can see how varies the shape of the vertical cross section of the sinking region (it is showed only a half for symmetry). In the left panel it is used a $L_{39} = 1$, and column base variables of: $l_0 = 7.6 \times 10^5$cm, and $d_0 = 1.4 \times 10^4$cm. Values that correspond to a dipole field strength of 3×10^{12}G. In the right panel, $L_{39} = 10.0$, and the values for the column base variables are: $d_0 = 4.5 \times 10^4$cm, and $l_0 = 4.7 \times 10^5$cm. Corresponding to a dipole field with strength 5×10^{13}G [Brice et al.(2021)].

Numerical results for models with fixed values for l_0 and d_0 are shown in the figure 3.5 in black, for a particular accretion luminosity and a power-law index $\xi = 1$ for the velocity profile. Numerical results for models in which l_0 and d_0 varies (in which also the curvature of the magnetic field lines have been taken into account), as a consequence of multipolar magnetic fileds, are instead showed in red. As we can see, the shape seems to coincide in the panel (a), for a dipolar field $B_{dip} = 3 \times 10^{12}$G, for both red and black results, while in the panel (b), $B_{dip} = 5 \times 10^{13}$G, we can see more discrepancy. In particular, red results predict a lower column height than black ones. In general, in case of a multipolar magnetic field, the length and width of the column base can be reduced by several factors, this will affects the plasma density, the internal temperature, the escaping flux and the maximum shock height.

Comparing the two models (with fixed base geometry in black, and variable base geometry in red), it is not easy to understand the cause for the variations between black and red results. This because the change in the base geometry (it decreases with increasing the magnetic field strength) causes the squeezing of the accretion column area, while the curvature of the field lines results in the opposite effect. Despite these effects, the accretion column properties remain quite the same.

Still in figure 3.5, the shape of the shock is clearly not quadratic in x, instead, the accretion column is narrowner than the shape predicted, and the height of the shock drops to zero at a width $\tilde{x} \leq d_0/2$, where $\tilde{x}$ is the width at which the radiation pressure, at the base of the column, equates the the Eddington flux one. Thus, for $x > \tilde{x}$, the radiation pressure at the base is smaller than the Eddington one, so no shock can be sustained.

Maximum height

In the figure 3.5 it is shown how the maximum column height H varies. The higher is the strength of the magnetic field, the lower is the maximum height of the shock. This is a consequence of the strong reduction of the opacity for X-mode photons, because in this way the escaping flux increases, so radiation easily escapes from the sides of the column, making the radiation pressure no longer be able to sustain an high column.

Internal and effective temperature

Since the shock height H decreases if the magnetic field strength increases, particles are dramatically decelerated at a point near to the NS surface. Mass conservation implies that the density in the sinking region is lower, and in the same way as the internal radiation temperature. So the internal temperature, like the opacity, shows an anti-correlation with the strength of the magnetic field (see figure 3.6).

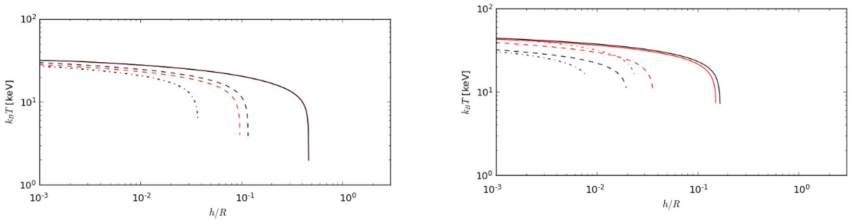

(a) (b)

Figure 3.6: Internal radiation temperature variations. Panels (a) and (b) correspond to the models shown in figue 3.5. The trend shows how the internal radiation temperature decreases increasing the magnetic field strength. [Brice et al.(2021)].

For what concerns the effective temperature, however, shows a completely opposite behavior with respect to the one of the internal temperature. The effective temperature is obtained from the escaping flux using $F_{\perp,esc} = \sigma T_{eff}^4$.

In figure 3.7 it can be seen that T_{eff} increases increasing the height above the

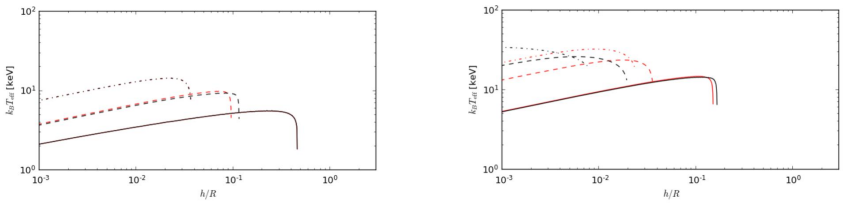

(a) (b)

Figure 3.7: Panels (a) and (b) correspond to the models shown in figure 3.5. The trend shows that the effective temperature increases with the increase of the magnetic field strength [Brice et al.(2021)].

neutron star surface, dropping then to zero at the top of the column. This is due to the fact that, at the bottom of the accretion column, both the density ρ and the geometrical thickness d_h are quite large, and translates into a large horizontal optical depth, which prevents radiation from escaping in that direction. Moving towards the top of the column, the optical depth decreases, so the escaping flux increases, and so does the effective temperature. In particular, the peak in the effective temperature profile indicates the altitude at which the outgoing flux is maximum. This, in addition, depends on the adopted density profile: for a velocity index $\xi = 1$, the effective temperature peak is close to the maximum column height, while for $\xi < 1$ the peak is at a lower height.

From the two plots, it is also clear that, the internal temperature (red lines fig. 3.6), is higher for a given column height with respect to that for models with a fixed base geometry. This is because, as said before, the same amount of energy is produced in a smaller area of the column. Still for the reduction of the column area, also the density in the sinking region increases, so for the radiation is more difficult to escape, and this results into a lower effective temperature.

Reduction of opacities

The Rosseland mean opacity, $\kappa_\perp$, is calculated in the central plane of the sinking region ($x = 0$), depending on both the total magnetic field strength, and temperature, in the column. Generally, a lower temperature, and a higher magnetic filed strength, reduce the perpendicular Rosseland mean opacity. In the figure 3.8 the trend of the normalized scattering opacity is shown. Thus, the ratio $\kappa_T/\kappa_\perp$ decreases slowly towards the top of the column, and when the top is reached, the ratio drops sharply to zero.

Results with different velocity indexes

Another important aspects to examine is the variation of the shock shape, varying the velocity index ξ. In the figure 3.9 the results obtained in different models with different ξ values are reported [Brice et al.(2021)]. It can be seen that increasing the velocity index ξ, the shape of the sinking region becomes narrower and lower, because particles are efficiently decelerated in the lower layers of the

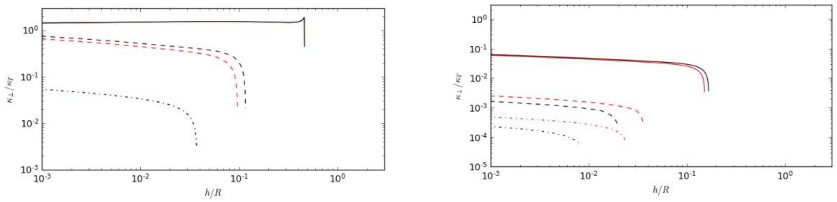

(a) (b)

Figure 3.8: Opacity trend. Panels (a) and (b) correspond to the models shown in figue 3.5. The trend shows that increasing the magnetic field strength the ratio $\kappa_\perp/\kappa_T$ decreases. Moreover the sattering opacity drops practically to zero at the top of the accretion column [Brice et al.(2021)].

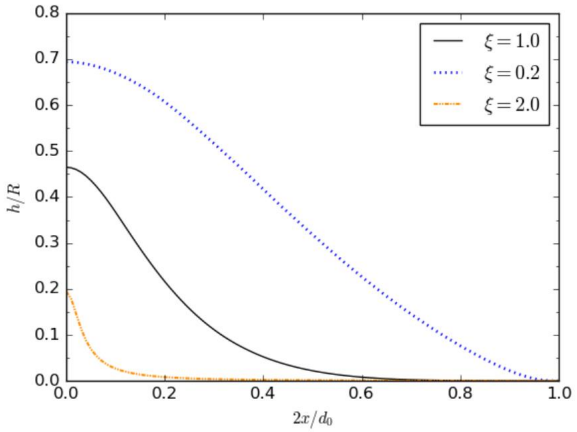

(a)

Figure 3.9: Variation of the column shape varying the velocity index. Half vertical cross section of the sinking region for models with $L_{39} = 1.0$, $B_{dip} = 3 \times 10^{12}$G, and $B_{oct} = 0$. The black solid line correspond to a power-law index $\xi = 1$, the blue dotted line to a $\xi = 0.2$, and the orange dot-dashed line to a $\xi = 2$ [Brice et al.(2021)].

column, concentrating in that region the radiation energy released, decreasing the column height.

3.4.4 Results for mixed polarization

In the model it has been assumed that the radiation is made by X-mode photons, imposing a polarization fraction $f = 1$. Nevertheless, a more detailed and realistic description of the radiation field requires also the presence of O-mode photons, and scattering that can convert X into O mode photons and vice versa. In order to understand if the emission of a super-Eddington luminosity is possible; also considering O-mode photons, solutions with different f values have been built up [Brice et al.(2021)].

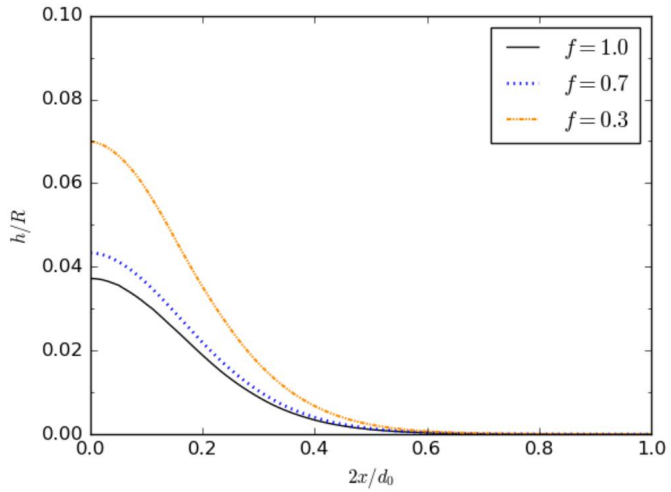

Figure 3.10: Vertical cross-section for various f values. In the figure is illustrated half of the column vertical cross-section, for a magnetic field $B_{dip} = 3 \times 10^{12}$G, $B_{oct} = 3 \times 10^{13}$G, and $L = 10^{39}$erg s^{-1}. The colored curves correspond to different values of f [Brice et al.(2021)].

Since a strong magnetic field affects the scattering cross-section of the X-mode photons, reducing the opacity, when we include in the radiation field also O-mode ones, the total opacity increases, since for the latter the scattering cross-section is not affected. Looking at the results predicted by the model, as expected, including O-mode photons, in an accretion column with a certain magnetic field strength and accretion luminosity, the total opacity increases, but the value of the scattering cross-section remains well below the Thomson one. This increase in the opacity results then into an increase of the column height, because the amount of radiation that can escape from the column side is decreased, so the radiation pressure is able to sustain an higher accretion column. In particular, to understand better the effects in changing the X-mode polarization fraction, three values were used: $f = 1, 0.7, 0.3$ (see figure 3.10). Another consequence of this, is the increase of the internal temperature and the decrease of the effective one (see figure 3.11), for the reasons already mentioned.

3.4.5 Results: disk-magnetosphere interaction

In the previous section, we stressed that the base geometrical variables (l_0 and d_0) depends on the disk-interaction model, which in turn is based on two principal parameters: the magnetospheric radius R_m, and the penetration depth P_m. But, as it can be seen from equation (3.36), the estimate of R_m requires the knowledge of the input parameter Λ, while for P_m it is required a prescription for ζ. Both the exact values of Λ and ζ are poorly known. Thus, analogously for the case of the X-mode polarization fraction, we can investigate the solidity of the model changing the values of this two parameters, comparing at the end the results.

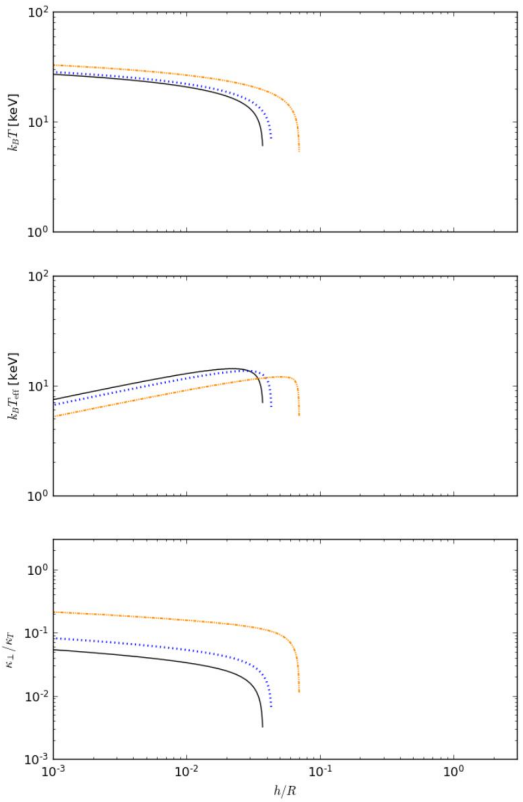

Figure 3.11: The accretion column properties for the same set of models as in figure 3.10. From top to bottom, the plots show the central internal temperature profile, the effective temperature profile, and the perpendicular mean opacity [Brice et al.(2021)].

As regards the parameter Λ, we used the canonical value of 0.5 [Ghosh & Lamb(1978)], but its exact value depends on how much is extended the region on which the NS magnetic field crosses the accretion disk; it was suggested that Λ should vary between $0.3 - 1$ [Dall'Osso et al.(2016)], and repeating calculations for l_0, varying Λ in that range, it turns out that there is no significant variation of the column base length, thus the global properties of the accretion column are not as sensitive to variations in Λ.

The parameter ζ, which was defined as the ratio P_m/R_m, is related to the variation of the column base width, and we assumed that the penetration depth was proportional to the disk height at R_m [Mushtukov et al.(2015)]. According to this, ζ can be given by

$$\zeta = \frac{\kappa_T}{c}\frac{3}{8\pi}\frac{\dot{M}}{R_m} \approx 0.2 L_{39}^{9/7} B_{d,12}^{-4/7}. \tag{3.51}$$

But from this equation it becomes clear that the value of ζ is close or in excess of 1, having to deal with higher accretion luminosity and low dipole field ($L_{39} \sim 10\text{erg s}^{-1}$, $B_{d,12} \sim 1$). From those values, we end up with the disk that penetrates through the entire magnetosphere, and this is unphysical. For this reason it was introduced by hand a maximum value for ζ. Another way to find the correct value for ζ is to use another type of prescription for P_m, based on a given set of physical principles. But this would then require an extension of the disk-magnetosphere interaction considering a geometrically thick disk. Alternatively, as already done for Λ, we can vary the value of ζ and see how d_0 is sensitive to its changes, without specify any particular disk-magnetosphere configuration. Varying ζ in the rage $(0 - 1)$, fixing the accretion luminosity $L = 10^{39}\text{erg s}^{-1}$, the dipole magnetic component $B_{dip} = 3 \times 10^{12}\text{G}$, and using different magnetic field strengths for the octupole component, it can be seen that d_0, differently from l_0, changes by one or more orders of magnitude (see figure 3.12). Since $F_{\perp,esc} \propto d_0^{-1}$, this time the luminosity is sensitive to variation in ζ.

3.4.6 Results for the maximum luminosity

Besides the results already showed, the main one is the value of the maximum luminosity (L_{max}). As stated at the beginning, we want to understand which is achievable maximum luminosity that a highly magnetized neutron star can reach, in order to compare it with the observed ones.

To compute the maximum luminosity, we have first to compute the maximum L_{acc} for each given set of model parameters, fixing the maximum shock height at $H = R$. We chose R as maximum height, because for higher values the luminosity grows slowly, and the curvature of the magnetic field lines has to be considered, since, affecting equation (3.19) for the vertical pressure balance, would make our approximations invalid. After having fixed $\xi = 1, f = 1, \zeta = 0.2$, the maximum luminosity is calculated for different magnetic field configurations: pure dipole field, a field with the octupolar component $B_{oct} = 3B_{dip}$, and then with the octupole $B_{oct} = 10B_{dip}$.

Results (see figure 3.13) show that, the value for the maximum luminosity is mostly fixed by the accretion column geometry when $B < 10^{13}\text{G}$. Since in this case the reduction of the opacities does not play an important role, and in

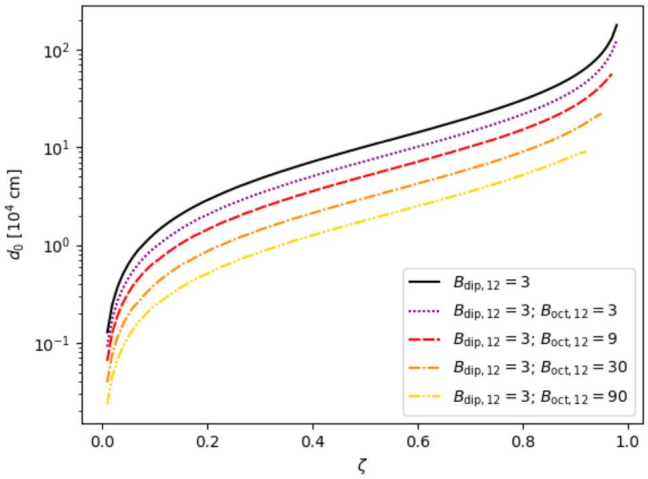

Figure 3.12: Changes of the column base width d_0, in units of 10^4cm, for a given ζ. All the profiles correspond to a $L_{39} = 1.0$, $M = 1.4M_\odot$, and $R = 10^6$cm [Brice et al.(2021)].

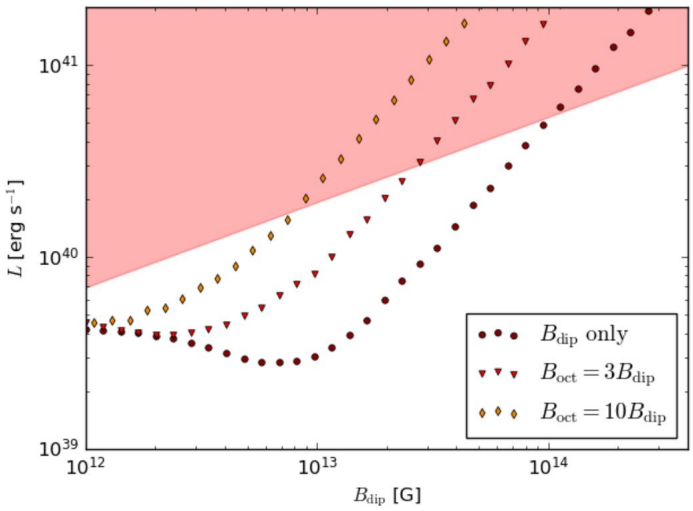

Figure 3.13: Variations in the maximum luminosity profile as function of the surface dipole field strength. The red shaded region are those in which the luminosity exceeds the neutron star Eddington one at the magnetospheric boundary (thus when the accretion flow is super-Eddington). The different markers (circles, triangles, and diamond) show the maximum luminosity computed for a pure dipole, an octupole $B_{oct} = 3B_{dip}$, and a $B_{oct} = 10B_{dip}$, respectively [Brice et al.(2021)].

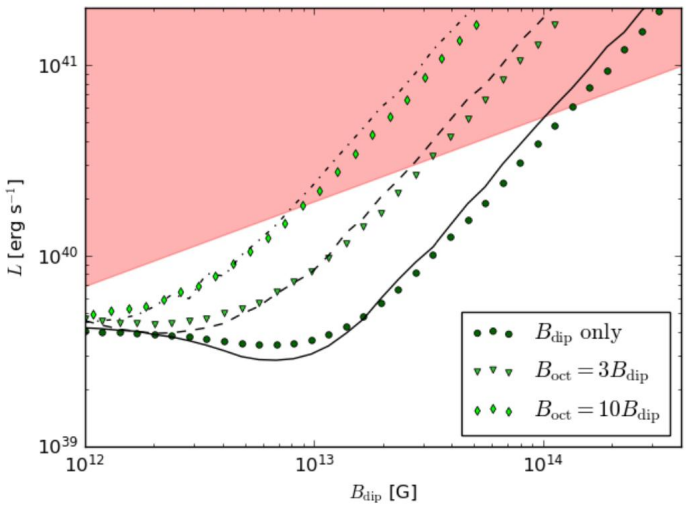

Figure 3.14: Same plot of fig. 3.13, using models with different f. The markers (circles, triangles, and diamonds) are computed using $f = 0.7$, and assuming a pure dipole, an octupole $B_{oct} = 3B_{dip}$, and a $B_{oct} = 10B_{dip}$, respectively. The lines (solid, dashed, and dot-dashed) shows the same configurations but with $f = 1$ [Brice et al.(2021)].

addition the photons energies are above the cyclotron energy, $E > E_{cycl}$, due to the typical internal temperature of the accretion column. Instead, in case of high magnetic field strengths, $B > 10^{13}$G, the scattering opacity of the X-mode photons is dramatically reduced with respect to the Thomson one κ_T, and this translates into a constraint on the maximum luminosity.

From figure 3.13 it can be seen that for a pure dipole field, the maximum luminosity profile shows a decrease up to a magnetic field strength of 10^{13}G. This can be explained taking into account that, as stated above, the accretion column becomes thinner as the magnetic field strengths increase, thus the internal temperature increases, and also the overall scattering opacity, so the radiation escapes from the column with more difficoulty. The variation of L_{max} tends to rapidly increase in case of a multipolar magnetic field, and the slope of such trend matches that obtained for a simple dipole field only when the magnetic strength is the same.

The previous profiles have been obtained considering only X-mode photons, but for a more realistic treatment we should take into account also O-mode ones. In figure 3.14 it can be seen the comparison between the profiles of the previous case, and those obtained with the same magnetic field configurations but taking a polarization fraction $f = 0.7$. Including also O-mode photons, the maximum shock height is increased, and for magnetic fields up to $\sim 10^{13}$G the maximum luminosity is lower than the case with $f = 1$. This trend is reversed for lower values of the magnetic field strength, when a fraction of O-mode photons is considered, since the average Rosseland mean opacity is decreased. This occurs when a large portion of the photons have energy of the order or higher than the electron cyclotron energy $E_{cycl} \sim 11.6 B_{12}$ keV.

In addition, looking to the plots in the figure 3.14, the trends obtained with the model with $f = 0.7$; have a shallower slope with respect to those obtained with $f = 1$, but the deviation is not significant. This is a consequence of the fact that most of the photons which supports the column are X-mode photons, so the effective opacity, computed in the Rosseland approximation, is dominated by X-mode one. Hence, at the end the difference in the overall opacity is small.

3.4.7 Comparison with previous model results

Taking the maximum luminosity from the model of Mushtukov et al. (2015) [Mushtukov et al.(2015)], we can compare it with that obtaind by Brice et al. (2021) [Brice et al.(2021)], in which are used a different method to calculate the scattering opacity, and a different model for the disk-magnetosphere interaction. In figure 3.15, the curves that represents the maximum luminosity obtained using this two models are shown. The difference in the maximum luminosities is only a few factors, which is an indication of proper agreement between the two codes.

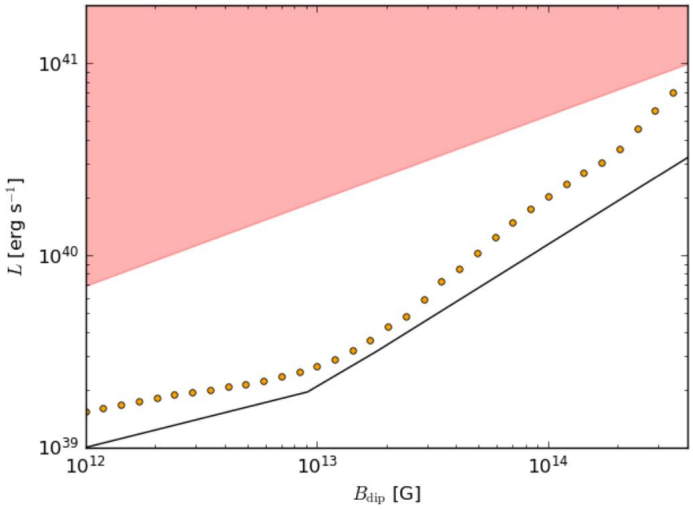

Figure 3.15: Same plot as in figure 3.13, but for models adopting a different disk model. The orange circles show the maximum luminosity for a pure dipole magnetic field strength on the surface, and with $\zeta_{max} \sim 1$. The black line shows the maximum luminosity according to the relation of Mushtukov et al. (2015) [Brice et al.(2021)].

CHAPTER

FOUR

NUMERICAL CODES

In this chapter we describe in some detail the two numerical codes which we used to derive the results presented in the next chapter. These are based on the accretion process around a NS described in the previous model. The first is for the visibility of the source, made by the torus (the region of the source limited by the magnetic field lines, of a dipolar field, that reach a certain maximum distance, R_{max}, from the star) and the disk, basically, determines what is the part in view of the object, for a certain configuration (thus for certain values of the parameters: R_{max}, R_{disk}, angles χ and ξ), giving the area of the regions which emit towards the observer. The second computes the flux as a function of the phase and of the energy, and it is implemented with the script of the visibility code, in order to consider only the part in view. the ray-tracer outputs are then exploited to produce the light curve and the spectrum of the source.

4.1 Visibility code

The first code establishes the region in view of the source (torus and disk), once fixed the inclinations of the magnetic axis, and the LOS with respect to the spin axis, and of the disc with respect to the direction of the magnetic one. The star will be considered totally hidden by the matter which is accreting along the field lines, towards the magnetic poles. To compute the part in view, the code takes into account the self-shadowing of the torus, given the particular non spherical shape of the torus itself, the shadow of the torus on the disk, and the shadow of the disk on the torus.

Let us now see how the code works. The code requires a number of input parameters:

1. R_{max}, the maximum distance from the star that the field lines which delineate the torus area can reach. Basically the radius of the magnetosphere;

2. χ, the angle between the rotational axis of the neutron star and the observer's line-of-sight (LOS);

3. ξ, the angle between the rotational axis and the star magnetic axis;

4. γ, the rotational phase angle.

The code calculates the part in view at each value of the phase rotation angle γ (counted from the projection of the LOS on the plane perpendicular to the spin axis). It is possible to produce several snapshots of the source at different stages (between 0 and 2π) or limit the output to only one phase value at a time.

4.1.1 Visibility of the torus

The first step is to determine the part in view of the torus. The code starts to compute the cartesian coordinates of the LOS unit vector, $\boldsymbol{l}$, in the reference frame of the star magnetic axis ($\boldsymbol{b_{dip}}$), in which the vertical axis coincides with the magnetic one. Still in the same reference frame, the code computes the cartesian coordinates of each point of the field lines, and the components of the unit normal vector $\boldsymbol{n}$ to the torus surface at each point.

The first condition to be fulfilled, in order to consider a point as in view, is:

$$\boldsymbol{l} \cdot \boldsymbol{n} \geq 0. \tag{4.1}$$

Given the complicated shape of the torus, the condition (4.1), alone, does not allow to distinguish if a given point on its surface is actually in view or covered by a region of the torus itself, interposed with respect to the observer (see figure 4.1).

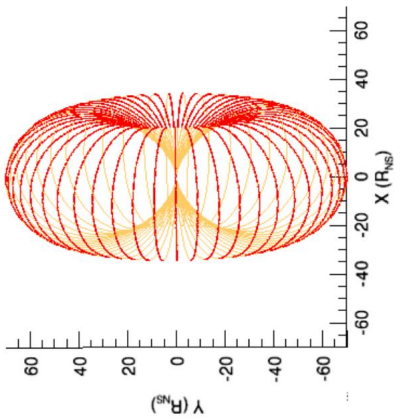

Figure 4.1: Part in view of the torus with $R_{max} = 70R_{NS}$, $\xi = 1°$, and $\chi = 80°$. The objects is seen in the LOS reference frame.

In order to exclude these points, and consider the self-shadow of the torus, the code proceeds as follows:

1. for each point selected by the previous condition (4.1) (characterized by the polar angles $\bar{\theta}$ and $\bar{\phi}$ in the $\boldsymbol{b_{dip}}$ frame), the code computes the intersections between the straight line parallel to the LOS, which passes through the point itself, and the torus surface;
2. between these intersections, there is again the point through which passes the straight line; with coordinates ($\bar{\theta}$, $\bar{\phi}$), this will not be taken into account for the next step;

3. for all the other intersections, defined by $(\theta_{sol}, \phi_{sol})$ in the $\boldsymbol{b_{dip}}$ frame, the scalar product $\boldsymbol{l} \cdot \boldsymbol{n}$ is again evaluated;

4. then the code removes the intersections with $\boldsymbol{l} \cdot \boldsymbol{n} < 0$, already excluded by the condition (4.1);

5. for the remaining roots, the code computes the z cartesian coordinate in the LOS reference frame; then this z is compared with $\bar{z}$, still computed in the LOS frame, of the point with $(\bar{\theta}, \bar{\phi})$;

6. if $\bar{z}$ is greater than all the z of the other intersections, then the point $(\bar{\theta}, \bar{\phi})$ is not hidden by any other points, and it is **in view**;

7. if, instead, there is at least one of the intersection points which has $z > \bar{z}$, then the point $(\bar{\theta}, \bar{\phi})$ will be marked as **not in view**.

At the beginning we have assumed that the star surface is totally covered by the material accreting along the field lines, so we can neglect the star shadow on the torus. In first approximation, this assumption works when we are dealing with strong magnetic fields, which present very large magnetospheres (thus large values of R_{max}) that covers the star surface. Since in the model already described (chapter 3), the magnetic field is very strong, this assumption is reasonable. In the case of weak magnetic fields, instead, one should take into account also that the torus can be covered by the star shadow. As I said, this is what it can be assumed in first approximation, since, even with strong magnetic fields, there would be visible points of the stellar surface, for example if we look exactly along the direction of the magnetic axis. But the emission from these points could be difficult to treat, principally because it is unlikely that the emission that one would see from the magnetic poles is that from the surface of the star, there will be effects of acceleration at the poles, so, at the end, one would not know how to treat them anyway.

It is important to mention that, in the method already described, for the sake of simplicity the effects due to the General Relativity (GR) are neglected. Indeed, it is used a straight line to find the intersections. This method holds as long as we do not consider torus points close to the magnetic axis, where the gravitational field of the star is more intense, and such effects are stronger. In that case, we expect there could be a minimum correction for GR effects. But for the moment we are interested in the emission of points far from the star surface. Maybe such GR corrections could be introduced in a future work.

4.1.2 Analytical expressions

As stated above, the code first compute the scalar product, for each point of the torus, between the normal $\boldsymbol{n}$ to the torus surface, and the unit vector $\boldsymbol{l}$, parallel to the LOS.

Hence, one has to obtain the expression for the unit vector $\boldsymbol{n}$. We do this in the $\boldsymbol{b_{dip}}$ reference frame since it is easier. The starting point is defining the position vector $f(\theta, \phi)$, which gives the position of the points on the surface of interest, in this case the torus surface. In polar coordinates it can be written as

$$f(\theta, \phi) = r \begin{pmatrix} \sin\theta\cos\phi \\ \sin\theta\sin\phi \\ \cos\theta \end{pmatrix}, \tag{4.2}$$

where θ and ϕ are the magnetic colatitude and azimuth, computed in the $\boldsymbol{b_{dip}}$ reference frame, while r is given by the parametric equation of the magnetic field lines (for a dipolar field, as we assumed):

$$r = R_{max} \sin\theta^2, \tag{4.3}$$

where R_{max} was defined above. Since only the part of the field lines outside the star is considered, because we can only receive the emission from the points outside, we have to take into account that the magnetic colatitude θ has a lower and an upper limit, thus it ranges in $[\theta_{min}, \theta_{max}]$. These two limiting values are given by the condition:

$$R_{max} \sin^2\theta = R_{NS} \quad \longrightarrow \quad \theta = \arcsin\left(\sqrt{\frac{R_{NS}}{R_{max}}}\right), \tag{4.4}$$

from this one obtain:

$$\theta_{min} = \arcsin\left(\sqrt{\frac{R_{NS}}{R_{max}}}\right) \quad , \quad \theta_{max} = \pi - \theta_{min}. \tag{4.5}$$

Once the equation (4.3) have been substituted into the (4.2), one can derive the two partial derivatives of $f(\theta, \phi)$: f_θ and f_ϕ, with respect to the colatitude θ, and the azimuth ϕ, respectively. $\boldsymbol{n}$ is then given by

$$\boldsymbol{n} = \frac{f_\theta \times f_\phi}{|f_\theta \times f_\phi|}. \tag{4.6}$$

In the case of interest we obtain

$$\boldsymbol{n} = \frac{1}{\sqrt{1 + 3\cos\theta^3}} \begin{pmatrix} (1 - 3\cos\theta^2)\cos\phi \\ (1 - 3\cos\theta^2)\sin\phi \\ 3\sin\theta\cos\theta \end{pmatrix}. \tag{4.7}$$

To impose the condition (4.1), it is needed also the unit vector $\boldsymbol{l}$, the components of which should be computed into the $\boldsymbol{b_{dip}}$ reference frame, as the components of $\boldsymbol{n}$, in order to calculate their scalar product. Its expression is

$$\boldsymbol{l} = \begin{pmatrix} \sin\eta\cos\delta \\ \sin\eta\sin\delta \\ \cos\eta \end{pmatrix} \tag{4.8}$$

where we can indicate the three components as (l, m, n), η is the colatitude of the LOS with respect to $\boldsymbol{b_{dip}}$, its cosine is given by the expression

$$\cos\eta = \cos\chi\cos\xi + \sin\chi\sin\xi\cos\gamma, \tag{4.9}$$

in which γ is the phase angle. The angle δ is the azimuth of the LOS with respect to $\boldsymbol{b_{dip}}$, and its cosine can be calculated as the scalar product between the projection $\boldsymbol{l}_\perp$ of $\boldsymbol{l}$ perpendicular to $\boldsymbol{b_{dip}}$, and the unit vector along the x-axis in the $\boldsymbol{b_{dip}}$ frame (which is called $\boldsymbol{p}$, see figure 4.2). To compute the components of $\boldsymbol{l}$ are also needed $\sin\eta$ and $\sin\delta$, since η is a colatitude ranging in [0,π], once we have the $\cos\eta$ the $\sin\eta$ is simply $\sqrt{1 - \cos^2\eta}$, since it is always positive

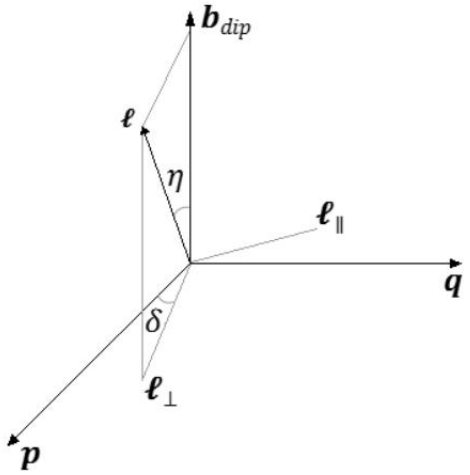

Figure 4.2: The line-of-sight in the $\boldsymbol{b_{dip}}$ reference frame.

between 0 and π. Instead, δ is an azimuth, which ranges in [0,2π], so knowing the $\cos\delta$ is not enough. One possibility is to evaluate the $\sin\delta$ taking the scalar product between $\boldsymbol{l}_{\parallel}$ and $\boldsymbol{p}$, exploiting the complementary angle to delta. Thus, to compute $\cos\delta$, one has to compute the scalar product $\boldsymbol{l}_{\perp}\cdot\boldsymbol{p}$. Since this scalar product is rotation-invariant (so it can be computed in any reference frame), and since we can easily obtain the expression of the unit vectors in the LOS frame, what one can do is to evaluate such product in the LOS reference frame, instead of the $\boldsymbol{b_{dip}}$ frame, expressing in it all the vectors. Hence, the components of the $\boldsymbol{b_{dip}}$ unit vector, in the LOS frame, are:

$$\boldsymbol{b_{dip}} = \begin{pmatrix} \sin\chi\cos\xi - \cos\chi\sin\xi\cos\gamma \\ \sin\xi\sin\gamma \\ \cos\chi\cos\xi + \sin\chi\sin\xi\cos\gamma \end{pmatrix}. \tag{4.10}$$

For the unit vector along the x-axis of the $\boldsymbol{b_{dip}}$ frame, $\boldsymbol{p}$, in order to express it in the reference frame of the LOS, the code follows the conventions used in [Taverna et al.(2015)], in which the expression for the unit vector is

$$\boldsymbol{p} = \begin{pmatrix} -\sin\chi\sin\xi - \cos\chi\cos\xi\cos\gamma \\ \cos\xi\sin\gamma \\ \sin\chi\cos\xi\cos\gamma - \cos\chi\sin\xi \end{pmatrix}. \tag{4.11}$$

Now, one can compute the unit vector $\boldsymbol{l}_{\perp}$, to obtain $\cos\delta$ ($\cos\delta = \boldsymbol{l}_{\perp}\cdot\boldsymbol{p}$). To determine the sign of δ, as said above, it is needed the scalar product between $\boldsymbol{p}$ and $\boldsymbol{l}_{\parallel}$. Which can be obtained by

$$\boldsymbol{l}_{\parallel} = \boldsymbol{b_{dip}}\times\boldsymbol{l}_{\perp}. \tag{4.12}$$

If the scalar product $\boldsymbol{l}_{\parallel}\cdot\boldsymbol{p}$ is positive, $\sin\delta$ is negative, this because the scalar product gives the cosine of the angle between $\boldsymbol{l}_{\parallel}$ and the positive direction of $\boldsymbol{p}$,

so the angle $\pi/2 + \delta$. Thus if the scalar product is positive, then the sign of δ is negative (and vice versa).

At this point, we have all the quantities, $\cos\delta$ and $\sin\delta$, and $\cos\eta$ and $\sin\eta$. These can be substituted into (4.8), to obtain the unit vector $\boldsymbol{l}$, and the scalar product between $\boldsymbol{l}$ and $\boldsymbol{n}$ can be evaluated. This allows one for a first selection of the torus points in view.

Deleting the part of the torus surface covered by the torus itself

We mentioned that it has to be considered the self-shadowing of the torus, since closer to the magnetic poles of the star, the torus can cover part of its own surface.

To delete the self-covered points of the torus, as stated above, one can make use of a straight line parallel to the LOS, and passing, each time, through each point "in view" selected by (4.1). What is needed is to find the intersections between this line, and the torus. Then one has to evaluate for each intersection the scalar product $\boldsymbol{l} \cdot \boldsymbol{n}$, select the points for which the latter is positive, and compare the z coordinates, in the LOS frame, of those points to select which of them are really in view.

The simplest way to do this, is starting doing calculations in the $\boldsymbol{b_{dip}}$ reference frame, using spherical coordinates. Let us start from a point of the torus for which $\boldsymbol{l} \cdot \boldsymbol{n} \geq 0$. It is characterized by the angles $(\bar{\theta}, \bar{\phi})$, in the $\boldsymbol{b_{dip}}$ frame, and its corresponding cartesian coordinates are given by equation (4.2):

$$\begin{pmatrix} \bar{x} \\ \bar{y} \\ \bar{z} \end{pmatrix} = R_{max} \begin{pmatrix} \sin\bar{\theta}^3 \cos\bar{\phi} \\ \sin\bar{\theta}^3 \sin\bar{\phi} \\ \sin\bar{\theta}^2 \cos\theta \end{pmatrix}, \tag{4.13}$$

while the LOS unit vector, in the $\boldsymbol{b_{dip}}$ frame, is still given by the equation (4.8). To find the intersections between the torus and the straight line (parallel to the LOS, and passing through this point) its equation is needed. In the three dimensional space, the equation of of a line passing through $(\bar{x}, \bar{y}, \bar{z})$ and parallel to (l, m, n), in the $\boldsymbol{b_{dip}}$ frame is

$$\begin{cases} \dfrac{x - \bar{x}}{l} = \dfrac{y - \bar{y}}{m} \\ \dfrac{y - \bar{y}}{m} = \dfrac{z - \bar{z}}{n} \end{cases}, \tag{4.14}$$

where (l, m, n) are the coordinates of the unit vector $\boldsymbol{l}$ in the $\boldsymbol{b_{dip}}$ frame. This form holds in the case $l, m, n \neq 0$. However, the components of the LOS, in the $\boldsymbol{b_{dip}}$ frame, depend on the angle η and δ, which in turn depend on χ, ξ and γ. Thus, any variation in these parameters can change the components of the LOS unit vector. Hence a complete overview of all the possible cases is

$$\begin{cases} x = \bar{x} \\ \dfrac{y - \bar{y}}{m} = \dfrac{z - \bar{z}}{n} \end{cases} \qquad (l = 0; m, n \neq 0); \tag{4.15}$$

$$\begin{cases} \dfrac{x - \bar{x}}{l} = \dfrac{z - \bar{z}}{n} \\ y = \bar{y} \end{cases} \qquad (m = 0; l, n \neq 0); \tag{4.16}$$

$$\begin{cases} \dfrac{x-\bar{x}}{l} = \dfrac{y-\bar{y}}{m} \\ z = \bar{z} \end{cases} \qquad (n=0; l, m \neq 0); \tag{4.17}$$

$$\begin{cases} x = \bar{x} \\ y = \bar{y} \end{cases} \qquad (l, m = 0; n \neq 0); \tag{4.18}$$

$$\begin{cases} x = \bar{x} \\ z = \bar{z} \end{cases} \qquad (l, n = 0; m \neq 0); \tag{4.19}$$

$$\begin{cases} y = \bar{y} \\ z = \bar{z} \end{cases} \qquad (m, n = 0; l \neq 0). \tag{4.20}$$

The intersections between the line, given by the previous systems, and the torus can be obtained by assuming that x, y, z coordinates are given by the equation of the torus (4.2), with polar angle θ_{sol} and ϕ_{sol}, at variance with the coordinates of the point $(\bar{x}, \bar{y}, \bar{z})$ where the polar angle are $\bar{\theta}$ and $\bar{\phi}$. The resulting solution will be different depending on the values of the components of the LOS, and so also the expression for the straight line.

Let us analyse the solution in the case: $\boldsymbol{l, m, n} \neq 0$. To solve the system (4.14) let us write it using polar coordinates (we will indicate θ_{sol} and ϕ_{sol} just with θ and ϕ, for the ease of notation):

$$\begin{cases} \frac{\sin^3\theta\cos\phi - \sin^3\bar{\theta}\cos\bar{\phi}}{l} = \frac{\sin^2\theta\cos\theta - \sin^2\bar{\theta}\cos\bar{\theta}}{n} \\ \frac{\sin^3\theta\sin\phi - \sin^3\bar{\theta}\sin\bar{\phi}}{m} = \frac{\sin^2\theta\cos\theta - \sin^2\bar{\theta}\cos\bar{\theta}}{n}. \end{cases} \tag{4.21}$$

The first equation can be solved for $\cos\phi$, obtaining the following solution

$$\cos\phi = \frac{\alpha\sin^2\theta\cos\theta + A}{\sin^3\theta}, \tag{4.22}$$

where $\alpha \equiv l/n$ and $A \equiv \sin^3\bar{\theta}\cos\bar{\phi} - \alpha\sin^2\bar{\theta}\cos\bar{\theta}$. In the same way, the second equation can be solved for $\sin\phi$, obtaining

$$\sin\phi = \frac{\beta\sin^2\theta\cos\theta + B}{\sin^3\theta}, \tag{4.23}$$

where $\beta \equiv m/n$, and $B \equiv \sin^3\bar{\theta}\sin\bar{\phi} - \beta\sin^2\bar{\theta}\cos\bar{\theta}$. Imposing $\cos^2\phi + \sin^2\phi = 1$, and writing the resulting equation in terms of $t \equiv \tan\theta/2$, one gets the final equation

$$\begin{aligned} C + 2(3C + 4\varepsilon)t^2 + (15C + 16\gamma + 16\varepsilon)t^4 + 4(5C - 8\gamma - 16)t^6 \\ +(15C + 16\gamma - 16\varepsilon)t^8 + 2(3C - 4\varepsilon)t^{10} + Ct^{12} = 0 \end{aligned} \tag{4.24}$$

where the quantities C, γ and ε are defined as

$$\begin{aligned} C &\equiv A^2 + B^2 \\ \gamma &\equiv \alpha^2 + \beta^2 \\ \varepsilon &\equiv \alpha A + \beta B. \end{aligned} \tag{4.25}$$

The solution of equation (4.24) can be found numerically using the routine `FZ_ROOT` in `IDL`, choosing only the real roots, since $\theta \in [0, \pi]$, only the roots

with positive real part are good solutions. In fact, one has $(\theta/2) = \arctan(t) \in [0, \pi/2]$, so $\theta = 2\arctan(t) \in [0, \pi]$. Eventually the coordinates of the points can be expressed in cartesian coordinates using again the equation (4.2).

If one of both between l and m are zero, but $n \neq 0$ the situation does not change much. The step to follow are the same of the generic case $l, m, n \neq 0$, but this time turns out that:

- for $l = 0$ and $m, n \neq 0$, then $\alpha = 0$;
- for $m = 0$ and $l, n \neq 0$, then $\beta = 0$;
- for $l, m = 0$ and $n \neq 0$, then $\alpha, \beta = 0$.

Case in which $\boldsymbol{l, m \neq 0}$ and $\boldsymbol{n = 0}$. The situation is a bit different than the previous ones. The system to use is the (4.17); substituting the cartesian coordinates with the polar ones, from the second equation results:

$$\sin^2\theta\cos\theta = \sin^2\bar{\theta}\cos\bar{\theta}. \tag{4.26}$$

This can be easily written as an equation for $\cos\theta$ only

$$\cos^3\theta - \cos\theta + \sin^2\bar{\theta}\cos\bar{\theta} = 0. \tag{4.27}$$

The solutions are:

$$\begin{aligned} &\cos\theta = \cos\bar{\theta} \\ &\cos\theta = \frac{-\cos\bar{\theta} \pm \sqrt{1 + 3\sin^2\theta}}{2} \end{aligned} \tag{4.28}$$

and since θ can assume values only in the first and second quadrants, $\cos\theta$ is sufficient to fully determine θ. For the azimuth, instead, let us take the first equation (4.17), written in polar coordinates, and defining:

$$\begin{aligned} &\zeta \equiv \frac{l}{m} \\ &D \equiv \sin^3\bar{\theta}\cos\bar{\phi} - \zeta\sin^3\bar{\theta}\sin\bar{\phi} \end{aligned} \tag{4.29}$$

we get

$$\cos\phi - \zeta\sin\phi = \frac{D}{\sin^3\theta}. \tag{4.30}$$

Finally, the solutions are given by

$$\phi = 2\arctan\left(\frac{-\zeta \pm \sqrt{\zeta^2 - (D^2/\sin^6\theta) + 1}}{(D/\sin^3\theta) + 1}\right) \tag{4.31}$$

What remains is the case: $\boldsymbol{n = 0}$ and one between $\boldsymbol{l}$ and $\boldsymbol{m}$ equal to 0. In this case the systems are (4.20) and (4.19). The steps for the θ solution are the same of the previous case, but this time, from the first equations in both the systems, the relations that came out for $\cos\phi$ and $\sin\phi$ are simpler to solve.

- if $l, n = 0$ and $m \neq 0$, it turns out that:

$$\sin^3\theta\cos\phi = \sin^3\bar{\theta}\cos\bar{\phi}, \tag{4.32}$$

  and the solution is

$$\cos\phi = \frac{\sin^3\bar{\phi}\cos\bar{\phi}}{\sin^3\theta} = \frac{A}{\sin^3\theta} \tag{4.33}$$

- if $m, n = 0$ and $l \neq 0$:

$$\sin^3\theta \sin\phi = \sin^3\bar{\theta}\sin\bar{\phi}, \tag{4.34}$$

the solution this time is

$$\sin\phi = \frac{\sin^3\bar{\phi}\sin\bar{\phi}}{\sin^3\theta} = \frac{B}{\sin^3\theta} \tag{4.35}$$

Attention must be taken in using the correct values of $\cos\phi$ and $\sin\phi$ in the coordinates of equation (4.2). This is due to the fact that, giving the value of $\cos\phi$ ($\sin\phi$) the $\sin\phi$ ($\cos\phi$) is expressed as $\sqrt{1-\cos^2\phi}$ ($\sqrt{1-\sin^2\phi}$), and since ϕ ranges in $[0, 2\pi]$, it is important to take into account the sign of both the solutions (i.e. $\sin\phi = \pm\sqrt{1-\cos^2\phi}$, in the case $l, n = 0$ and $m \neq 0$, while $\cos\phi = \pm\sqrt{1-\sin^2\phi}$, in the case $m, n = 0$ and $l \neq 0$).

4.1.3 Visibility of the torus adding a thin disk

In the previous section we have described the steps through which the code determines the points of the torus that are really in view, given certain values for the input parameters. Now we consider also a thin disc in addition, perfectly planar, with vanishing thickness.

The procedure consists of two steps:

1. find the equation of the disk plane
2. determine which points of the disk are in view, taking into account the presence of the torus.

The equation of the disk plane can be obtained once defined the normal to the plane itself. The calculations are made in the $\boldsymbol{b_{dip}}$ frame, and once θ_p and ϕ_p are defined, which are the angles identifying the normal in the $\boldsymbol{b_{dip}}$ frame, the vector is given by:

$$n_p = \begin{pmatrix} \sin\theta_p\cos\phi_p \\ \sin\theta_p\sin\phi_p \\ \cos\theta_p \end{pmatrix}. \tag{4.36}$$

To find the equation of the disk plane, we take a generic vector belonging to the plane, and then, recalling that the plane is orthogonal to $\boldsymbol{n_p}$, we require that the scalar product between the normal $\boldsymbol{n_p}$ and the plane vector is zero. Since the disk should pass through the center of the star O, which is also the center of the $\boldsymbol{b_{dip}}$ frame, we can take as plane vector OP, where $P = (x, y, z)$ is a generic point in the disk plane.

Imposing the following condition:

$$OP \cdot \boldsymbol{n_p} = 0 \tag{4.37}$$

we end up with

$$x\sin\theta_p\cos\phi_p + y\sin\theta_p\sin\phi_p + z\cos\theta_p = 0, \tag{4.38}$$

which is the disk plane equation.

Now, in order to understand which part of the torus remains in view once the disk is added, let us distinguish two cases: if the disk is infinitely extended, and if instead it is limited. If the disk is an infinite plane, then the visibility of the torus would depend on what side of the disk is visible, given a certain direction of the LOS. In particular:

- the disk is seen from above if $\boldsymbol{l} \cdot \boldsymbol{n_p} > 0$;
- the disk is seen from below if $\boldsymbol{l} \cdot \boldsymbol{n_p} < 0$.

The terms "above" and "below" are defined with respect to direction of the magnetic axis, so if we are looking at the disk from "above", we will see the northern part of the torus, if we are looking at the disk from "below", we will see the southern part of the torus. For this distinction, the normal $\boldsymbol{n_p}$ is chosen in such a way that θ_p ranges in $[0,\pi/2]$. Taking a generic field line of the torus, characterized by the azimuthal angle $\bar{\phi}$ in the $\boldsymbol{b_{dip}}$ frame, the intersection with the disk will be in a point at $\theta_{intersect}$. To find this angle we solve the system made by the equation of the disk plane (4.38) and the coordinate of a generic torus point:

$$\begin{pmatrix} x \\ y \\ z \end{pmatrix} = R_{max} \begin{pmatrix} \sin^3\theta\cos\phi \\ \sin^3\theta\sin\phi \\ \sin^2\theta\cos\theta \end{pmatrix} \tag{4.39}$$

Substituting equation (4.39) into (4.38) we obtain:

$$\sin^3\theta\cos\phi\sin\theta_p\cos\phi_p + \sin^3\theta\sin\phi\sin\theta_p\sin\phi_p + \sin^2\theta\cos\theta\cos\theta_p = 0. \tag{4.40}$$

Once $\bar{\phi}$ is fixed, from this equation we can get θ. The two solutions are:

$$t_{1,2} = \frac{\cos\bar{\phi}n_p^x + \sin\bar{\phi}n_p^y \pm \sqrt{(\cos\bar{\phi}n_p^x + \sin\bar{\phi}n_p^y)^2 + n_p^{2z}}}{n_p^z} \tag{4.41}$$

The solution with the minus sign can be rejected, because, as said before, θ can assume values only in the first and second quadrant, so the only possible solution is the positive one. At the end, the solution for $\theta_{intersect}$ is

$$\theta_{intersect} = 2\arctan\left(\frac{\cos\bar{\phi}n_p^x + \sin\bar{\phi}n_p^y \pm \sqrt{(\cos\bar{\phi}n_p^x + \sin\bar{\phi}n_p^y)^2 + n_p^{2z}}}{n_p^z}\right) \tag{4.42}$$

Once we have the value for $\theta_{intersect}$ for each $\bar{\phi}$, the visibility condition for the torus will be:

- if the plane is seen from above, $\boldsymbol{l} \cdot \boldsymbol{n_p} > 0$, the points in view will be those with $\theta \in [\theta_{min}, \theta_{intersect}]$;
- if the plane is seen from below, $\boldsymbol{l} \cdot \boldsymbol{n_p} < 0$, the points in view will be those with $\theta \in [\theta_{intersect}, \theta_{max}]$.

One has to remember that these conditions hold in the hypothesis of infinite disk, where the only part of the torus that can be seen is that in the side in view of the disk plane. If, as said before, the disk, instead, has a finite extent, and we select certain values for the angles ξ and χ, we would see also a little

part of the torus in the side not in view of the disk plane. Hence, the conditions above can be used if the radius of the disk is extremely large.

In order to take into account also the emerging part of the torus from the side not in view of the disk, we should understand which points of that part of the torus are covered by the shadow of the disk, and to do so we project the latter on the torus. Important to stress is the the fact that we assume circular the disk. A simple way to do it is to use a straight line parallel to the LOS, intersecting the disk, and passing through the torus surface, which emerges from the side not in view of the disk plane. Thus, the straight line passes through those points with, once $\bar{\phi}$ is fixed, the angle $\theta \in [\theta_{intersect}, \theta_{max}]$ if the side in view is that with $\boldsymbol{l} \cdot \boldsymbol{n_p} > 0$, or $\theta \in [\theta_{min}, \theta_{intersect}]$ if the part in view is that with $\boldsymbol{l} \cdot \boldsymbol{n_p} < 0$.

To find the intersection between the straight line, passing through the torus, and the disk, we have to solve different systems of equations, depending on the coordinates of the LOS unit vector $\boldsymbol{l}$. This is analogous to the previous case, when we have searched for the intersections between the torus and the straight line. Again, the easiest way is performing calculations in the $\boldsymbol{b_{dip}}$ reference frame, and we will distinguish different cases, depending on the coordinates of $\boldsymbol{l}$ in this reference frame. We start, as bafore, with the case: $\boldsymbol{l, m, n \neq 0}$. Now the system to be solved, in order to find the intersections is

$$\begin{cases} \frac{x-\bar{x}}{l} = \frac{y-\bar{y}}{m} \\ \frac{y-\bar{y}}{m} = \frac{z-\bar{z}}{n} \\ x n_p^x + y n_p^y + z n_p^z = 0 \end{cases}, \tag{4.43}$$

where the coordinates

$$\begin{pmatrix} \bar{x} \\ \bar{y} \\ \bar{z} \end{pmatrix} = R_{max} \begin{pmatrix} \sin^3\bar{\theta}\cos\bar{\phi} \\ \sin^3\bar{\theta}\sin\bar{\phi} \\ \sin^2\bar{\theta}\cos\bar{\theta} \end{pmatrix} \tag{4.44}$$

are those of the selected point of the torus, with $\theta \in [\theta_{intersect}, \theta_{max}]$ ($[\theta_{min}, \theta_{intersect}]$) for $\boldsymbol{l} \cdot \boldsymbol{n_p} > 0$ ($\boldsymbol{l} \cdot \boldsymbol{n_p} < 0$), and $\bar{\phi} \in [0, 2\pi]$. In the system (4.43) the coordinates (x, y, z) are those of the intersection point between the straight line parallel to the LOS, passing through the torus point $(\bar{x}, \bar{y}, \bar{z})$, and the disk plane. In the calculations we are still assuming that the disk has an infinite extent.

To solve the system, we can first rewrite the first two equations, explicitating x and z as functions of y:

$$\begin{aligned} x &= \frac{l}{m}(y - \bar{y}) + \bar{x} \\ z &= \frac{n}{m}(y - \bar{y}) + \bar{z} \end{aligned} \tag{4.45}$$

then, substituting them into the third equation of the system we can find the solution for y:

$$y = \frac{(l/m)n_p^x\bar{y} - n_p^x\bar{x} + (n/m)n_p^z\bar{y} - n_p^z\bar{z}}{(l/m)n_p^x + n_p^y + (n/m)n_p^z}. \tag{4.46}$$

At this point, to understand if the intersection on the disk plane belongs to the disk, covering the torus, it can be imposed the following condition: $x^2+y^2+z^2 \leq r$, where r is the radius of the disk. If the point belongs to the disk, the torus

point $(\bar{x}, \bar{y}, \bar{z})$ is covered by it, otherwise no intersection is found, and the torus point is in view.

Following the same reasoning, the solutions for the other cases are:

- $\boldsymbol{m \neq 0}$, and one or both $\boldsymbol{l}$ and/or $\boldsymbol{n}$ are zero. If $\boldsymbol{l = 0}$

$$y = \frac{(n/m)n_p^z \bar{y} - n_p^x \bar{x} + n_p^z \bar{z}}{n_p^y + (n/m)n_p^z}, \tag{4.47}$$

if $\boldsymbol{n = 0}$

$$y = \frac{(n/m)n_p^x \bar{y} - n_p^x \bar{x} - n_p^z \bar{z}}{(l/m)n_p^x + n_p^y}, \tag{4.48}$$

if $\boldsymbol{l, n = 0}$

$$y = \frac{-n_p^x \bar{x} - n_p^z \bar{z}}{n_p^y} \tag{4.49}$$

- $\boldsymbol{m = 0}$. If $\boldsymbol{l, n \neq 0}$, solving this time for z

$$z = \frac{(l/m)n_p^x \bar{z} - n_p^x \bar{x} - n_p^y \bar{y}}{(l/m)n_p^x + n_p^z}, \tag{4.50}$$

if $\boldsymbol{m, l = 0}$ and $\boldsymbol{n \neq 0}$

$$z = \frac{(-n_p^x \bar{x} - n_p^y \bar{y})}{n_p^z}, \tag{4.51}$$

if $\boldsymbol{m, n = 0}$, but $\boldsymbol{l \neq 0}$, solving for x

$$x = \frac{-n_p^y \bar{y} - n_p^z \bar{z}}{n_p^x}. \tag{4.52}$$

Deleting the part of the disk hidden by the torus

Much as the disk may shadow a part of the torus, the torus may be hidden by the disk. In order to see how this works, first of all we have to define the disk points, in the $\boldsymbol{b_{dip}}$ reference frame, using a grid of radial distance ρ and azimuthal angles ϕ. For convenience it is better if the azimuthal grid of the disk is the same used for the torus field lines (with $\phi \in [0, 2\pi]$). Since, once we have computed the intersection points between the torus and the disk, for each field lines characterized by the azimuth ϕ, then we have the colatitude $\theta_{intersect}$ for each point of the disk with azimuth $\phi \in [0, 2\pi]$. So each of those points would be associated to the colatitude $\theta_{intersect}(\phi)$.

Thus, the disk points will have the following coordinates

$$\begin{pmatrix} x_d \\ y_d \\ z_d \end{pmatrix} = \rho \begin{pmatrix} \sin\theta_{intersect}(\phi)\cos\phi \\ \sin\theta_{intersect}(\phi)\sin\phi \\ \cos\theta_{intersect}(\phi) \end{pmatrix}, \tag{4.53}$$

where the radial distance ρ ranges in principle between 0 (center of the star) and r (radius of the disk). The points of the disk close to the star are not in view because the torus hides them, and in particular for each azimuth ϕ there

is a minimum radius below which the disk points are not in view. Knowing the intersection points, it is easy to find this minimum radius, given by

$$r_{min}(\phi) = R_{max} \sin(\theta_{intersect}(\phi))^2, \tag{4.54}$$

which is the equation for the magnetic field lines (those that reach the maximum distance R_{max}). Hence, the correct range in which the radial distance, ρ, can vary, in the $\boldsymbol{b_{dip}}$ frame, is $[r_{min}(\phi), r]$. Now, one has to understand how those points hidden by the torus can be deleted. The procedure is the following:

1. start selecting one by one all the disk points;
2. write down the equation of the straight line parallel to the LOS and passing through each point of the disk;
3. find the intersections between the straight line and the field lines of the torus
4. if there are intersections, thus field lines between the disk points and the observer, then disk points are not in view, because covered by the torus, and they have to be removed from the points in view;
5. if there are no intersections, then the disk points are not hidden by any field lines, so they can be considered in view.

Trying to simplify the calculations, one can think to implement the procedure taking only the points of the disk with a negative z coordinate, as measured in the LOS frame. This is because all the disk points ahead of the torus are expected to have positive z coordinate in the LOS frame. However, there could exist cases in which, due to the particular geometry, there are points of the disk with positive z coordinate but still covered by the torus. This means that for a better treatment we should take into account all the disk points.

Analogously to the previous case, computations for the intersections between the torus and the straight line are different depending on the components of the LOS in the $\boldsymbol{b_{dip}}$ frame.

If all the cartesian components of the LOS are different from zero, $\boldsymbol{l, m, n \neq 0}$, then the straight line parallel to the LOS and passing through the disk point (x_d, y_d, z_d) is

$$\begin{cases} \frac{x-x_d}{l} = \frac{y-y_d}{m} \\ \frac{y-y_d}{m} = \frac{z-z_d}{n} \end{cases} \tag{4.55}$$

The intersection point between the torus and the straight line can be written in terms of θ and ϕ, through equation (4.39), and then, following a procedure similar to the one seen before (expliciting x and y as functions of z), we obtain the following expressions for θ and ϕ of the intersection point:

$$\begin{aligned} \cos\phi &= \frac{R_{max}(l/n)\sin\theta^2\cos\theta - (l/n)z_d + x_d}{R_{max}\sin\theta^3} \\ \sin\phi &= \frac{R_{max}(m/n)\sin\theta^2\cos\theta - (m/n)z_d + y_d}{R_{max}\sin\theta^3}. \end{aligned} \tag{4.56}$$

Defining:

$$\alpha_d \equiv \frac{l}{m} \quad , \qquad \beta_d \equiv \frac{m}{n} \quad , \qquad A_d \equiv \frac{x_d - \alpha_d z_d}{R_{max}} \quad , \qquad B_d \equiv \frac{y_d - \beta_d z_d}{R_{max}} \tag{4.57}$$

the equations (4.56) can be rewritten in terms of these quantities:

$$\begin{aligned} \cos\phi &= \frac{\alpha_d \sin^2\theta\cos\theta + A_d}{\sin^3\theta} \\ \sin\phi &= \frac{\beta_d \sin^2\theta\cos\theta + B_d}{\sin^3\theta}. \end{aligned} \tag{4.58}$$

The solution can be expressed once we define also:

$$\begin{aligned} C_d &\equiv A_d^2 + B_d^2 \\ \gamma_d &\equiv \alpha_d^2 + \beta_d^2 \\ \epsilon_d &\equiv \alpha_d A_d + \beta_d B_d \end{aligned} \tag{4.59}$$

The solution is found numerically. If $l = 0, m \neq 0$, the solution can be obtained putting $\alpha_d = 0$, if, instead, we are in the case $l \neq 0, m = 0$, we get the solution putting $\beta_d = 0$. Finally, if both $l, m = 0$, to find the solution $\alpha_d, \beta_d = 0$.

In the case in which $n = 0$, the system (4.55) will be rewritten, and as before we substitute (x, y, z) using (4.39). Then, once we have the two expressions for θ and ϕ, they would be solved numerically through the `IDL` procedure, `FZ_ROOT`, the same used for the previous cases.

Once the intersections between the straight line parallel to the LOS, passing through the disk points, and the torus have been determined, we have to select the points of the disk that are in view from those that are not. Let us follow these steps:

1. looking at the equations for θ, if there are no real solutions, or (if $l, m, n \neq 0$) the real ones are such that $\tan(\theta/2) < 0$, then there will be no intersection, thus the point of the disk is no hidden by any field line, so it is in view;

2. if, instead, there are real solutions for $\theta \in [0, \pi]$, then the disk point is covered by the torus;

3. if there are no good solutions for ϕ (e.g. $\sin\phi, \cos\phi > 1$ or < -1), then there are no intersections, and the disk point is in view;

4. if, on the contrary, there is at least one good solution for ϕ, there is at least an intersection, so the point is covered by the torus.

Particular cases exist, with particular geometries, in which the intersection between the straight line and the disk is behind the disk point itself, instead to be between the disk and the observer. When this happen, the disk point is in view, thus the code must exclude these intersections. To do this it is necessary to compute, in the LOS frame, the z coordinates, of the intersection points (z_{LOS}), and compare them with the z coordinate of the disk point ($z_{LOS,d}$), still computed in the same frame:

- if for all the intersections holds $z_{LOS} < z_{LOS,d}$, then the intersections are behind the point, with respect to the observer. Thus, the disk point is in view;

- if, instead, there is at least one intersection for which holds $z_{LOS} > z_{LOS,d}$, then the disk point is covered.

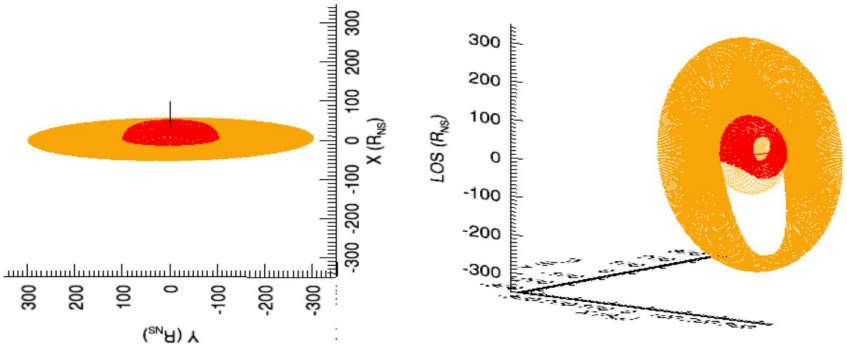

(a) (b)

Figure 4.3: 3D Plot of the part in view of the system. Panel (a): the source seen along the LOS, thus it can be seen only the part in view of the source, composed by the torus (in red), and the disk (in orange). Panel (b): the source seen along a direction different from that of the LOS. There are both the part in view and that not in view of the source. The part not in view is that transparent. Both the images have been obtained for a $R_{max} = 100R_{NS}$, $R_{disk} = 300R_{NS}, \chi = 80°, \xi = 1°$, and $\gamma = 45°$.

Figure 4.3 shows the output of the code for a typical input configuration.

The source is seen from two different points of view. To be more precise, looking at it from the observer point of view (panel (a), along the LOS), the source is seen nearly edge-on ($\chi = 80°, \xi = 1°$), and what is shown is only the part in view. To better visualize the parts which are in view or are hidden, the same configuration is shown again in panel (b), this time as seen from a different direction. In this case the southern hemisphere of the torus is totally hidden, because of the disk, the part of the torus near the magnetic pole is hidden because of the self-shadowing of the torus itself, and the missing part of the disk, instead, is due to the torus shadow.

4.2 Ray-tracer code

The second code is the `ray-tracer`, it has already been used in other works ([Taverna et al.(2015)], [Zane & Turolla(2006)]), but the version used in this thesis has been implemented (as mentioned) with the visibility code script. This code gives the flux, integrated all over the part in view, at each phase and energy. From this output can be obtained subsequently the spectrum and the light curve of the source (torus and disk), given a particular configuration (angles ξ, χ, and values for R_{max} and R_{disk}).

4.2.1 Functionality

To understand how the ray-tracer works, let us start considering the source surface as a collection of emitting points. The code, first, selects which of these

are visible, depending on the choice of the angles χ and ξ (working in the LOS frame), and on the orientation of the disk with respect to the spin axis.

Once the points in view have been selected, the code assigns to each of them a blackbody emission, which clearly depends on the temperature. Such temperatures, for the torus, are read from an external file, which is in turn the output of the code of Brice et al. (2021)[Brice et al.(2021)], based on the previous work of Mushtukov et al. (2017)[Mushtukov et al.(2017)]. As regards the disk, the emission (if required) is still that of a blackbody, but for the temperature at which the disk points emit we have two possible choices. The code can describe the disk emission using or a constant temperature profile, or a different one as the Shakura-Sunyaev temperature profile. The last should be the most reliable. In this thesis, however, the code exploits a constant temperature profile, which is easier and a good approximation. The reason why is that, in using a Shakura-Sunyaev temperature profile, it should be created a file with a certain number of radii (distances between the center of the star and the disk points) and the corresponding temperatures; then the ray-tracer should read also this file, and once it selects a point on the disk, maybe at a distance that could not match the grid points in radius of the file just created, it should interpolate between the nearest radii to give at the end the total emission from the disk. Thus the constant profile avoids such interpolation. Moreover, the Shakura-Sunyaev temperature profile requires parameters that the code for the temperature outputs does not give.

Important to stress is that, as in the visibility code, the GR effects are switched off. The code is defined in order to take into account GR effects like those on the magnetic field, and the ray-bending. But we will not take them into account, since we want the emission from points on the torus which are, in general, quite far away from the star, where such effects should not be relevant. Moreover, in this code we do not consider the emission from the column, thus from points near to the magnetic axis, since the calculations for those points would be too difficult. But maybe in future works these corrections will be taken into account.

Once at each point (torus and eventually disk) has been assigned a blackbody emission with a certain temperature, the code computes the flux, all across the part in view, as a function of the energy and of the phase. Basically what we have is a matrix with the flux values for each energy and phase, and then one can decide how to use such outputs. In this case, as it will be discussed later, we will use them to reproduce the light curves and the spectra of the source.

4.2.2 Inputs

As regards the inputs to give to the code, the first are

1. the polar magnetic field strength B; we explored the range 10^{12}G - 10^{13}G;
2. the maximum radius R_{max}, expressed in units of R_{NS};
3. the angle ξ, expressed in degrees.

Then mass of the neutron star, the star radius, and the minimum and maximum magnetic colatitude (θ_{min} and θ_{max}, see the previous section), are already defined in the code script. The code requires also the insertion of a value for the angle χ.

Other inputs are those for the disk:

- if it is orthogonal to the spin axis;
- its radius.

We chose always the disk orthogonal to the spin axis of the star. Then are required the values of the temperatures on the torus surface, and such values have been determined, as said before, by the code of [Brice et al.(2021)]. Since these temperatures are computed for a given choice of the first three parameters: B, R_{max} and ξ, the file with those temperatures cannot be chosen randomly, since at the beginning we gave certain values for the magnetic field strength, maximum radius, and ξ angle, thus those temperatures must be chosen consistently with that choice.

Finally the code asks for the disk emission, since it provides that the disk emits or not. If the disk emits, it has to be assumed again a blackbody emission (as said above), choosing then or for a constant temperature profile, or for a non constant one (e.g. Shakura-Sunyaev profile).

In the code are also defined parameters aimed to calculate also the polarization fraction and polarization angle for the emitted radiation, but we will neglect that part of the code, since in this thesis we are not interested in the polarization properties, and we will sum the flux of O-mode and X-mode photons.

4.2.3 Main program

It is initiated a big `do` loop, in which, for each phase angle γ, the code computes all the quantity needed to compute the outputs (the flux).

First, different unit vectors and angles are defined and computed, required for further calculations:

1. the spin axis unit vector in the LOS frame, which does not depend on the phase angle, and lies, for assumption, on the xz plane (in the sense that we define the x-axis of the LOS frame in order to have the star spin axis on the xz plane),
$$\boldsymbol{\Omega} = \begin{pmatrix} \sin\chi \\ 0 \\ \cos\chi \end{pmatrix};$$
2. the $\boldsymbol{b_{dip}}$ unit vector, directed along the magnetic field axis, in the LOS frame
$$\boldsymbol{b_{dip}} = \begin{pmatrix} \sin\chi\cos\xi - \cos\chi\sin\xi\cos\gamma \\ \sin\xi\sin\gamma \\ \cos\chi\cos\xi + \sin\chi\sin\xi\cos\gamma \end{pmatrix};$$
and also the x-axis $\boldsymbol{p}$, and y-axis $\boldsymbol{q}$ of the $\boldsymbol{b_{dip}}$ frame in the LOS one [Taverna et al.(2015)].

Then, two other loops are opened on the colatitude Θ, and the azimuth Φ. These are the colatitude and azimuth, respectively, of the emitting point in the LOS reference frame. Since we want the emission of the part in view of the source, the code is implemented with the script of the visibility one. All these steps, are repeated for each phase angle, in order to compute all the required quantities as function of the phase. Hence, all this part is inserted in a big `do` loop.

Light curves and spectra

At the end, the code, for each phase angle and energy, computes the flux integrated all over the part in view of the object. Indeed, we have alreay mentioned the fact that the outputs of the ray-tracer are the values of the flux as functions of the energy and of the phase.

Having these outputs, through the use of an `IDL` script, we can, for instance, compute the average flux for each phase, or for each energy. This in order to have the light curves and the spectra of the emitting object. In particular, for the light curve, the flux is first computed at each phase angle γ, and then it is averaged all over the energies. For the spectrum, instead, the total phase interval is first decomposed into several phase bins, and for each of them is computed the averaged phase flux, after is also computed the total averaged flux, all over the phase interval, remaining only a function of the energy.

CHAPTER

FIVE

RESULTS

In chapter 4, we presented two codes: the visibility code, and the ray-tracer. Now we present some preliminary results, mainly concerning the pulse profiles and the (phase-resolved) spectra which are derived from the model.

First of all, we focused on the shape of the light curve and on the spectrum, as the geometry in view changes, that is, the angle between the spin axis and the LOS.

As said above, to obtain our results a number of input parameters have to be fixed in advance: the magnetic field strength B, the maximum radius R_{max}, and the angle ξ, that between the spin and magnetic axes. In this case we consider a neutron star with a mass of $1.4M_{\odot}$, a radius of 10km, and let us show different light curves and spectra, for different χ angles, as computed for: $B = 10^{12}$G, $R_{max} = 26.8R_{NS}$, $R_{disk} = 100R_{NS}$, and $\xi = 3°$.

For the sake of clarity, we report in figure 5.1 an illustration of the part in view of the source at different viewing inclinations χ, frozen at a phase angle $\gamma = 45°$. As it can be seen , the change in the inclination allows the observer to see different regions of the torus and of the disk.

In the following we present three cases, taking into account both the spectrum and the light curve.

As a testbed of our calculation, we start considering the case shown in figure 5.1 (a), in which the LOS is nearly parallel to both the spin axis and magnetic axis ($\chi = 2°$, $\xi = 3°$), so the object is a nearly aligned rotator seen from above. This means that during a complete rotation of the NS, the part in view will not change so much, and we expect to see an almost flat pulsed profile (no change in the flux with phase), and roughly the same spectral shape at each phase. This is, in fact, what we see in figure 5.2. The light curve remains almost flat, and there is little variation between the light curves in the different energy bands. Because the part in view of the source is more or less always the same as the phase changes, so we can expect the flux, in different energy bands, to be more or less the same as the phase changes. The same reasoning can be applied to the spectrum. The colored lines refer to the spectrum obtained for different phase bins: the total phase interval is divided into several bins, and in each of them is calculated the spectrum, averaged on the phases of the single bin. As

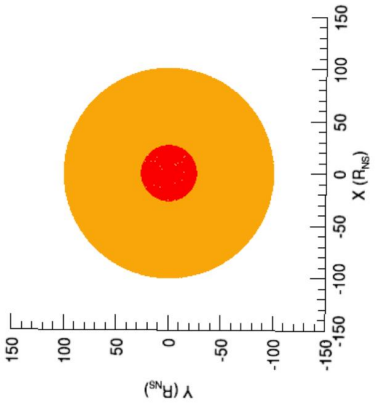

(a)

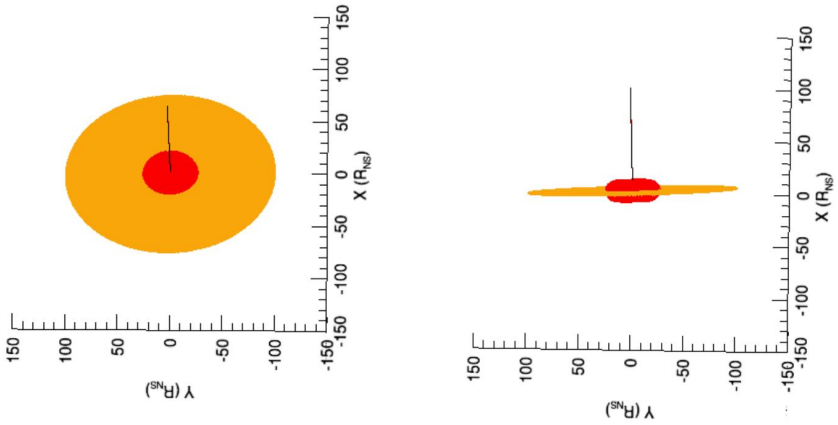

(b) (c)

Figure 5.1: Different geometries of view of the source, made by the torus (red) and the disk (orange). In all the three panel the object is seen along the LOS direction. In panel (a) the source is seen with $\chi = 2°$, thus in a face-on configuration. In panel (b) $\chi = 44°$; and in panel (c) $\chi = 89°$, the source is nearly along the edge of the disk. All the three plots have been obtained for $B = 10^{12}$G, $R_{max} = 26R_{NS}$, $\xi = 3°$, $R_{disk} = 100R_{NS}$, and $\gamma = 45°$.

expected by the light curve, the spectra at the various phases appear mostly superimposed. Defining the pulsed fraction (PF)

$$\mathrm{PF} = \frac{max(F(E)) - min(F(E))}{max(F(E) + min(F(E))} \tag{5.1}$$

where $max(F(E))$ and $min(F(E))$ are the maximum and minimum value of $F(E)$, which is the flux, integrated in a given energy band, all over the phase interval, its value for this specific configuration ranges between $\sim 0.09\%$ and $\sim 0.7\%$, for the different bands considered (see Figure 5.2a). Not surprisingly,

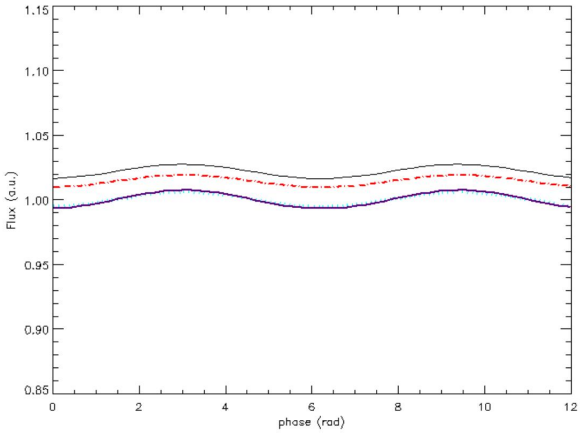

(a)

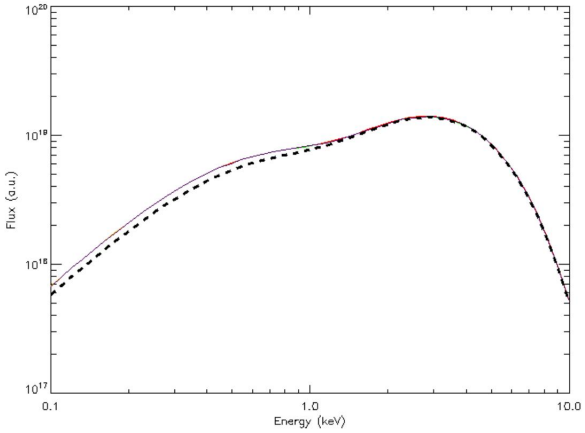

(b)

Figure 5.2: Light curve and spectrum for the configuration with $\chi = 2°$, and $\xi = 3°$. Panel (a): the pulse profile of the source, different colors are related to different energy bands: 0.1-10 keV black,, 0.3-0.8 keV violet, 0.3-1 keV blue, 1-3 keV red, 3-5 keV cyan, 5-8 keV purple. Panel (b): the spectrum, the dashed thick black line is the total phase averaged flux, while the colored lines are the spectra obtained in different phase bins. For the disk component we adopted a constant temperature profile, with a temperature $T_d = 0.2$ keV. Here it is $B = 10^{12}$G, and $R_{max} = 26R_{NS}$.

there is no difference between the spectra at different phases, the pulsed fraction being very small.

Moving to the second configuration (panel (b) in figure 5.1), the only difference is the angle $\chi = 44°$, while the other parameters were being unchanged. This time, the LOS is not aligned with the spin axis, and so during a complete rotation the part in view changes, and the emitting regions are different at each phase. Hence, what we expect to see is a more pronounced pulsed profile, and a more evident variation also in the spectra for each phase bin.

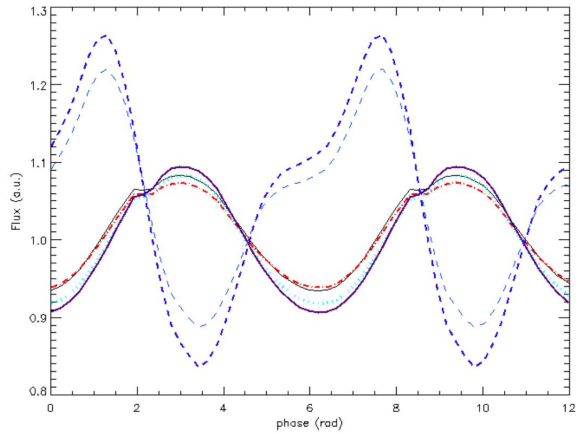

(a)

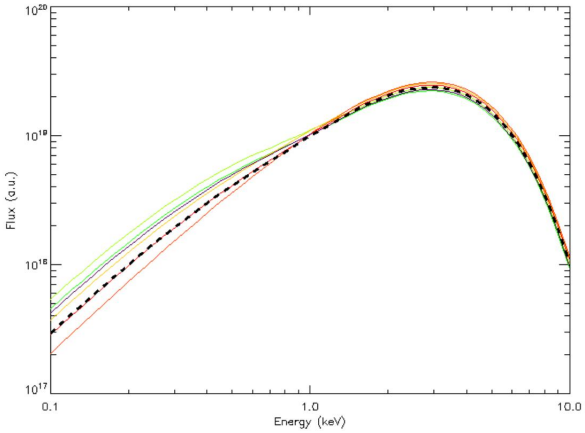

(b)

Figure 5.3: Light curve and spectrum for the configuration with $\chi = 44°$. The pulse profiles are shown in panel (a), while the spectra in panel (b). The color code and the value of the parameters are the same for fig. 5.2.

In fact, at variance with the case shown in fig. 5.2, now the pulsation is more pronounced (fig. 5.3), since the regions in view of the torus and the disk are different for different phase angles. In particular are clearly visible sharp peaks at low energies (blue and violet fig. 5.3(a)).

In order to understand why it is so, let us consider that in the simulations taken into account, the temperature of the disk is typically lower than the temperature of the various regions of the torus. One can therefore expect that the emission of the disk is localized at lower energies, while that of the torus to higher energies. In the figure 5.3(a), the light curves in the lower energy bands are those in the 0.3-1 keV band (blue), and 0.3-0.8 keV band (violet). From those light curves we see that, at a certain phase, the flux decreases a lot, and this can be a consequence of the torus shadow on the disk. In that geometrical configuration both the torus and the disk are quite well visible,

but during the rotation the torus covers part of the inner region of the disk, decreasing its emission. As further evidence of this, we produced another plot, with the pulse profile and the spectrum for the same configuration ($\chi = 44°$, $\xi = 3°$), but without the disk emission (see figure 5.4). In this way, the disk does not emit but it is still present, covering the parts of the torus which covered before. In the figure 5.4, the net peaks at lower energies disappeared, all the

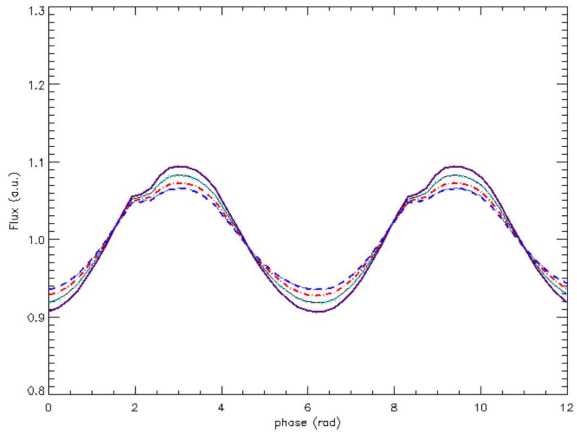

(a)

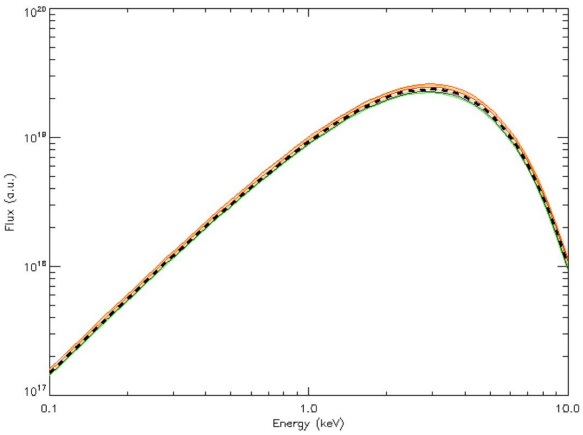

(b)

Figure 5.4: Light curve and spectrum for the configuration with $\chi = 44°$, without the disk emission.

light curves follow nearly the same trend, and in the spectrum all the lines are quite superimposed, proving that the emitting area of the torus does not change much. This proves that the previous sharp variations in the flux were due to the disk, and not maybe to the self-shadowing of the torus.

Moreover, the pulsed fraction corresponding to the situation in figure 5.3 varies between $\sim$ 7% and $\sim$ 20%, the highest occurring in the lower energy band (violet curve), without the disk emission (fig. 5.4) the PF varies between $\sim 0.7\%$ (at lower energies) and $\sim 0.9\%$, as expected.

Now we focus on the spectra, returning to the configuration with the disk emission. As a consequence of the LOS inclination, the spectra show more variability, since the area of the emitting regions changes more at each phase bin. This variation in the spectral shape is more evident for the disk (as for the light curves), since, again, such evident displacement between the colored spectra are visible at lower energies (for reasons mentioned above). Still focusing on the disk spectral component, this is more visible in the configuration with $\chi = 2°$, since in that case one can see a larger emitting area of the disk.

The third and last configuration shown in the figure 5.1, is that with $\chi = 89°$. The LOS is nearly orthogonal to the spin and magnetic axis, and, as in the first case, the part in view remains the same at each phase, so we should not expect a peaked light curve, or a noticeable variation in the spectrum. In fact, in the

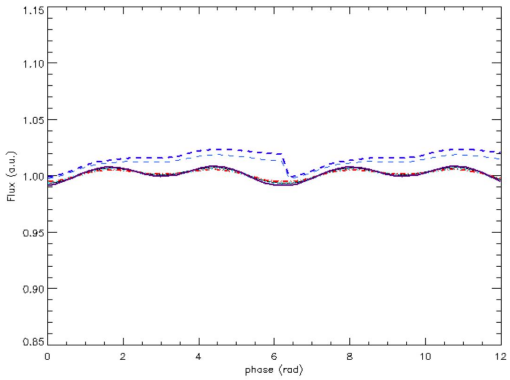

(a)

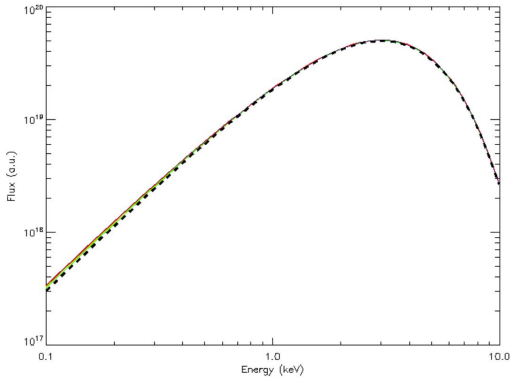

(b)

Figure 5.5: Light curve and spectrum for the configuration with $\chi = 89°$. The light curve is shown in panel (a) and the spectrum in panel (b). The color code and the values of the parameters are the same as in fig.5.2.

figure 5.5, the light curve is again nearly flat, with a very small variation in the flux for all the energy bands, and the spectrum is only due to the torus emission, since, for $\chi = 89°$, the thin disk is virtually invisible. To be more precise, in the light curve, at a phase of 2π, is visible a sharp decrease of the flux, in the lower energy bands. This could be due to two possible reasons: at that phase we see

the disk completely edge-on, thus its emission suddenly vanishes, or there are numerical irregularities in the code of Brice et al. (2021) [Brice et al.(2021)].

The PF ranges between $\sim$ 0.6% and $\sim$ 1.2%. The higher values are still those in the lower energy bands, and referring to the panel (c) of figure 5.1, the disk plane is not exactly parallel to the LOS, so (linking us to what was just said) the only little variation in the emission should be from that component.

Comparison with observations

The purpose of the model discussed in this thesis is to reproduce the data obtained from observations, for the spectrum, and the pulsed profiles (especially the PF). In chapter 2, we have presented six PULXs. Here we present such comparison making reference with the light curves and pulsed fractions of NGC 7793 P13 [Fürst et al.(2016)], the second PULX that has been discovered.

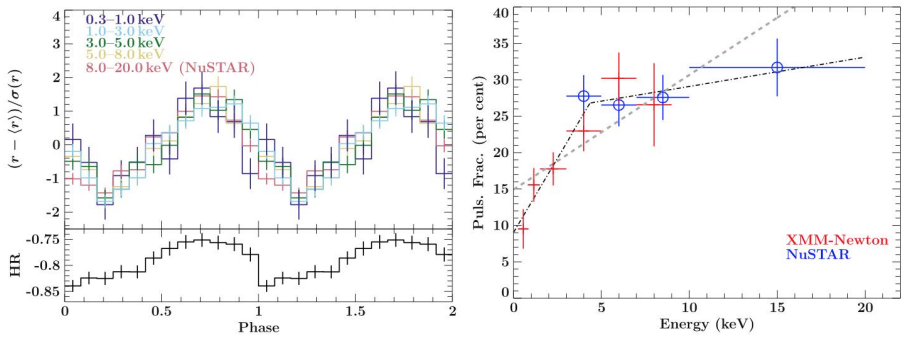

Figure 5.6: The light curve and the pulsed fraction variation for the PULX NGC 7793 P13. The top left panel displays the light curve in different energy bands, 0.3–1.0, 1–3, 3–5, and 5–8 keV obtained from XMM-Newton data, and 8-20 keV obtained with NuSTAR data. On the right there is the variation of the pulsed fraction as a function of energy, blu data are those from NuSTAR, red data are from XMM-Newton. The bottom left panel reports the hardness ratio. See [Fürst et al.(2016)].

In the right panel of figure 5.6, we see how the pulsed fraction changes with energy, in the data obtained with XMM-Newton (red), and NuSTAR (blu). While the XMM-Newton data describe a rapidly growing trend with a pulsed fraction ranging from the ≈8% to just above the ≈30%, between 0.3 and 8 keV, the NuSTAR data lie all between the ∼25% and ∼35%, in the energy range 5-15 keV.

Another example, in which the increase of the PF with the energy is quite evident, is that of the PULX NGC 300 ULX1 [Carpano et al.(2018)] (see figure 5.7). In addition, the pulse profile of NGC 300 ULX1 shows narrower and higher peaks with respect to the profile of NGC 7793 P13. Moreover the pulsed fraction is higher, if we look at the EPIC-pn data (0.2-10 keV), which cover almost the same total energy band (0.3-8 keV) as for NGC 7793 P13. The PF of NGC 300 ULX1 goes from $\sim$ 40% to just above $\sim$ 75%.

On a qualitative ground, we can compare these data with those we get from our code. From the spin up of the PULX NGC 7793 P13 [Fürst et al.(2016)],

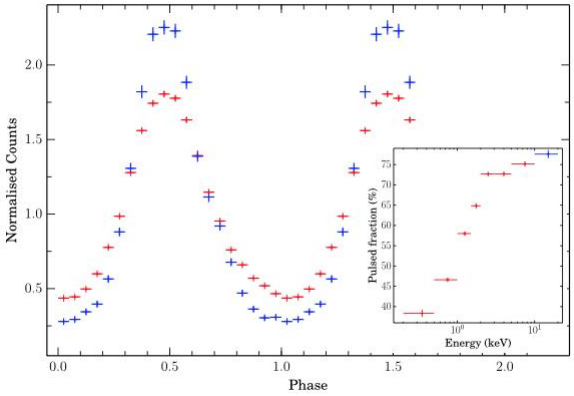

Figure 5.7: Light curve and energy-dependent pulsed fraction of NGC 300 ULX1. The pulse profile is obtained from the 0.2–10 keV EPIC-pn data (red), and the 3–20 keV NuSTAR data (blue). In both the profiles the background has been subtracted, and are corrected for the pulsar spin-up. The inset shows the pulsed fraction as function of energy, with colours as in the light curve plot. See [Carpano et al.(2018)].

it has been inferred a magnetic field strength of $B \sim 1.5 \times 10^{12}$G. Assuming as input parameters: $B = 10^{12}$G, $R_{max} = 26N_{NS}$, $R_{disk} = 150R_{NS}$, $\xi = 10°$, and $\chi = 43°$, we obtain the following output (see figure 5.8). The pulsed fraction

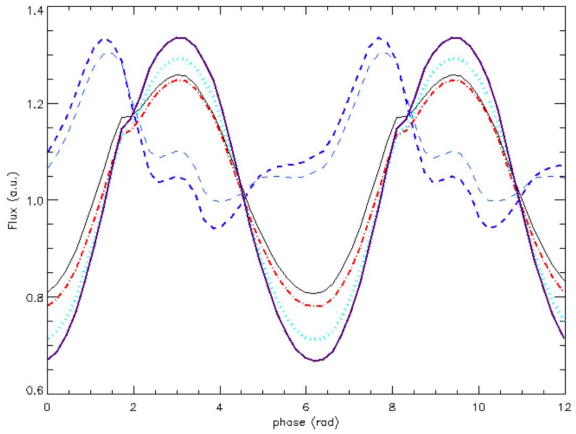

Figure 5.8: Light curves for values compatible for NGC 7793 P13. The color code is the same as in figure 5.2. The input parameters are: $B = 10^{12}$G, $R_{max} = 26N_{NS}$, $R_{disk} = 150R_{NS}$, $\xi = 10°$, and $\chi = 43°$.

predicted by the code for this configuration goes from a minimum of $\sim 11\%$ in the energy range 0.3-1 keV (blue dashed line), to a maximum of $\sim 32\%$ in the range 5-8 keV (purple solid line). Which is compatible with the variations in the XMM-Newton data in the energy band 0.2-8 keV.

For what concerns the second PULX mentioned before, NGC 300 ULX1

[Carpano et al.(2018)], its magnetic field has been derived using two different approaches: with the standard disc accretion model of [Ghosh & Lamb(1979)], and knowing that the equilibrium spin period is between 8.5s and 14s. The first method provides a value of $B \sim 3 \times 10^{12}$G, while the second one gives B in between $B \sim 1 \times 10^{13}$G and $B \sim 2 \times 10^{13}$G. Hence, we run the code choosing as input parameters: $B = 10^{13}$G, $R_{max} = 71 N_{NS}$, $R_{disk} = 200 R_{NS}$, $\xi = 10°$, and $\chi = 47°$, obtaining the output in figure 5.9. The pulsed fraction predicted

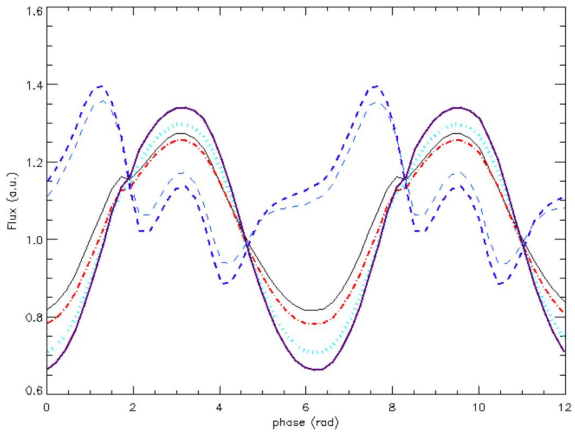

Figure 5.9: Light curves for values compatible for NGC 300 ULX1. The color code is the same as in Figure 5.2. The input parameters are:$B = 10^{13}$G, $R_{max} = 71 N_{NS}$, $R_{disk} = 200 R_{NS}$, $\xi = 10°$, and $\chi = 47°$.

in this case by the code goes from a minimum of $\sim$ 18% in the energy range 0.3-1 keV (blue dashed line), to a maximum of $\sim$ 34% in the range 5-8 keV (purple solid line). The results in the figures 5.8 and 5.9 are quite closer to each other, and to the PF variation shown in figure 5.6, although, both show lower PFs with respect to those reported by [Carpano et al.(2018)]. One possible explanation for this discrepancy could be the fact that, in the current code, the model is very simplified, being a blackbody emission for both the torus and the disk. In fact, for the spectrum, we cannot make a complete comparison with the observations. Let us consider again the PULX NGC 300 X1, and its spectra obtained with XMM-Newton and NuSTAR observations (figure 5.10). Neglecting the variation of the spectral shape in the observations of 2010 and 2016, the spectrum seems to be described by a two-component model, a power-law with photon index $\sim$ 1.6, which dominates at higher energies (non-thermal component), and a softer blackbody emission for temperatures $kT \sim 0.18$ keV. The code, however, is written to be able to reproduce a thermal spectrum, albeit at a different temperature distribution between the torus and the disk. Focusing only on the thermal component of the spectra in figure 5.10, one can see that the emission is peaked in the energy range 0.5-1 keV, which may be compatible with that produced by an accretion disk with a temperature of about $\sim 0.2-0.3$ keV. To prove this, we reproduced the spectrum in figure 5.11, obtained with $B = 4 \times 10^{12}$G, $R_{max} = 26 R_{NS}$, $R_{disk} = 100$, $\xi = 10°$, and $\chi = 30°$ (this configurations produces the same values of the PF as the last configuration used). In figure 5.11, one can see the contribution of the disk between the

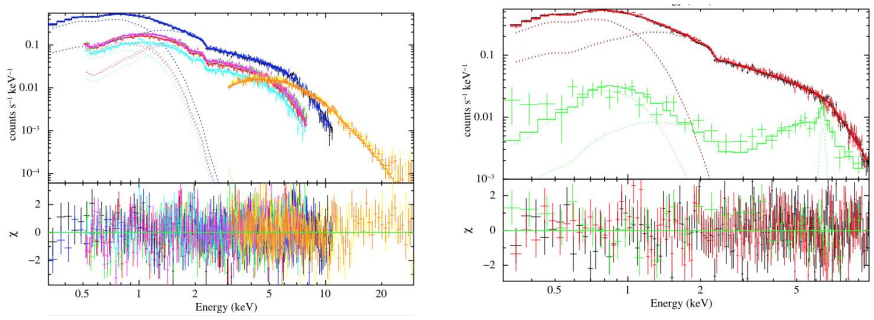

(a) (b)

Figure 5.10: XMM-Newton and NuSTAR spectra of NGC 300 X1. On the top of both panels the broad-band spectral fit of NGC 300 ULX1 is shown, exploiting the XMM–Newton and NuSTAR spectra. XMM-Newton data: EPIC-pn in black and blue, MOS in red, green, magenta and cyan. NuSTAR: FPMA and FPMB in yellow and orange. The panels on the bottom display the residuals for the best-fitting model [Carpano et al.(2018)].

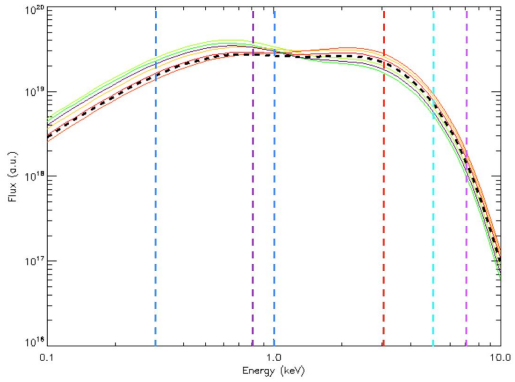

Figure 5.11: Simulated spectrum with a thermal disk component compatible with that of NGC 300 X1. The different colors show the phase averaged spectrum in different phase bins. The total averaged phase spectrum is represented by the dashed thick black line. The vertical colored dashed lines highlight the different energy bands used for the light curves. Here it is with $B = 4 \times 10^{12}$G, $R_{max} = 26 R_{NS}$, $R_{disk} = 100$, $\xi = 10°$, and $\chi = 30°$.

energies 0.3-1 keV, in the image are inserted six vertical colored dashed lines that are related with the colors used for the different energy bands of the light curves: 0.3-0.8 keV violet, 0.3-1 keV blue, 1-3 keV red, 3-5 keV cian, and 5-8 keV purple.

CHAPTER

SIX

CONCLUSIONS

In this thesis we presented a model to account for the observed properties of pulsating ULXs, based on the accretion process onto a highly magnetized NS.The model provides a description of the thermal emission from the envelope, which forms around the accreting NS, made by the accretion disc and a torus shaped by the field lines that reach the magnetospheric radius. The model also provides the description of the accretion column and its main characteristics as the magnetic field strength varies. The variation in the magnetic field strength has direct consequences on the reduction of the scattering cross-section of X-mode photons, and hence the opacity associated to this mode is drastically reduced. This reduction has, in turn, consequences on the column height, on the internal and effective temperature, but principally, on the amount of flux that can escape from the sides of the column. As already mentioned, if the magnetic field strength is high enough, then the amount of flux which escapes can explain the high luminosity, in the X-rays, observed for the PULXs. Such luminosities, as said at the beginning, can reach values up to $L \sim 10^{40}$erg s^{-1}.

The codes developed for the numerical simulations are focused on the accretion processes around the star, so on the formation and the emission of an accretion thin disk, which is truncated at the Alfvén radius, where matter start to accrete along the magnetic field lines leading to the formation of a torus. For the sake of simplicity, the torus is modeled by the lines of a purely dipolar magnetic field, and the disk is assumed as a thin disk.

The first code solves the problem of the visibility of the source, that is determines the part in view of the torus and of the disk at a given phase, once the values of the parameters have been fixed, which are the radius of the disk and its inclination with respect to the spin axis, the magnetospheric radius, and the inclinations of the LOS and the magnetic axis with respect to the spin axis. Exploiting the results of the visibility code, the ray-tracing code computes the total flux coming from the source summing over the part in view at each rotational phase.

The complexity of the emitting region (formed by the torus and the disk) and the selection of the part in view distinguish the version of the ray-tracing code used in this work from those used in previous ones ([Zane & Turolla(2006)],

[Taverna et al.(2015)], and [Taverna & Turolla(2017)]). Moreover, in this version, the temperature profile of the disk is constant, while that of the torus derives from the code of Brice et al.(2021) [Brice et al.(2021)]. From the ray-tracer outputs we could we could extract the light curve of the source and its spectrum (using an post-production `IDL` script to plot these results).

We then first compared the numerical results obtained for three different geometries of view of the source, obtained for fixed values of B, R_{max}, ξ, and γ, and changing only the LOS inclination with respect to the spin axis of the NS (χ). This allowed us to check that the code works correctly. In fact, as seen in figures 5.2, 5.3, and 5.5, there are no big variations in the light curves of different energy bands, and in the spectra, when the part in view is always the same at each phase, thus in the face-on and edge-on cases. This is because the emission which arrives to the observer comes always from the same emitting area. Hence, the light curve is nearly flat, and the spectra obtained for different phase bins are quite overlapped each other, as well as with the total phase averaged spectrum. The only different case is that with $\chi = 44°$, where the part in view changes with the rotation of the source, thus at each phase the emission from the part in view is not the same, and so observing in different energy bands, the emitting area changes. This time the light curve presents two evident peaks, and the spectra at each phase bin are more displaced among themselves. Thus, as expected, when the source is seen in such a geometrical view, we have evident changes in the emission both at each phase and in each energy band.

We have then compared the code light curves with those collected in two past observations, NGC 7793 P13 [Fürst et al.(2016)], and NGC 300 ULX1 [Carpano et al.(2018)]. Using two different sets of input parameters ($B = 10^{12}$G, $R_{max} = 26N_{NS}$, $R_{disk} = 150R_{NS}$, $\xi = 10°$, $\chi = 43°$, and $B = 10^{13}$G, $R_{max} = 71N_{NS}$, $R_{disk} = 200R_{NS}$, $\xi = 10°$, $\chi = 47°$) we obtained two different light curve profiles to be compared with those observed. It turns out that our numerical simulations are indeed able to reproduce pulsations, with also the observed increasing trend of the pulsed fraction, as a function of energy. But while the PFs of the first configuration ($B = 10^{12}$G, $R_{max} = 26N_{NS}$, $R_{disk} = 150R_{NS}$, $\xi = 10°$, $\chi = 43°$), are quite in agreement with the observed data of NGC 7793 P13, those of the second ($B = 10^{13}$G, $R_{max} = 71N_{NS}$, $R_{disk} = 200R_{NS}$, $\xi = 10°$, $\chi = 47°$) are systematically lower than what observed in NGC 300 ULX1. Maybe an explanation could be the presence of a more extended magnetosphere and disk, or the fact that the model used in our code is very simplified, since takes into account only a blackbody emission for both the torus and the disk. In fact, in the spectra only the disk thermal component at low energy is compatible with the soft thermal emission of observed ones.

For what concerns the spectrum, taking into account that observed for NGC 300 ULX1, we comcluded that a proper comparison cannot be done, since the observed spectra seem to be described by a two-component model, one thermal at lower energies $kT \sim 0.18$keV (blackbody emission), and the other non thermal (power-law) at higher energies. Since the code simulate only a thermal emission, we considered just the thermal component, seeing that the spectrum results compatible with that of the code for energies between 0.3-1 keV, which is produced by the blackbody emission of the disk at a temperature of 0.2keV.

In conclusion, the broad agreement we found between the results of our code

and the observation can be satisfactory, taking into account all the simplified assumption we made in this first work.

BIBLIOGRAPHY

[Atapin(2018)] Atapin, K. (2018). Ultraluminous x-ray sources. *arXiv preprint arXiv:1812.02516*.

[Bachetti et al.(2014)] Bachetti, et al. (2014). An ultraluminous x-ray source powered by an accreting neutron star. *Nature*, *514*(7521), 202–204.

[Bachetti et al.(2013)] Bachetti, M., et al. (2013). The ultraluminous x-ray sources ngc 1313 x-1 and x-2: a broadband study with nustar and xmm-newton. *The Astrophysical Journal*, *778*(2), 163.

[Basko & Sunyaev(1976)] Basko, M., & Sunyaev, R. A. (1976). The limiting luminosity of accreting neutron stars with magnetic fields. *Monthly Notices of the Royal Astronomical Society*, *175*(2), 395–417.

[Bilous et al.(2019)] Bilous, A. V., et al. (2019). A nicer view of psr j0030+ 0451: evidence for a global-scale multipolar magnetic field. *The Astrophysical Journal Letters*, *887*(1), L23.

[Binder et al.(2011)] Binder, B., et al. (2011). Chandra detection of sn 2010da four months after outburst: Evidence for a high-mass x-ray binary in ngc 300. *The Astrophysical Journal Letters*, *739*(2), L51.

[Binder et al.(2016)] Binder, B., et al. (2016). Recurring x-ray outbursts in the supernova impostor sn 2010da in ngc 300. *Monthly Notices of the Royal Astronomical Society*, *457*(2), 1636–1643.

[Borghese et al.(2015)] Borghese, A., et al. (2015). Discovery of a strongly phase-variable spectral feature in the isolated neutron star rx j0720. 4–3125. *The Astrophysical Journal Letters*, *807*(1), L20.

[Borghese et al.(2017)] Borghese, A., et al. (2017). Narrow phase-dependent features in x-ray dim isolated neutron stars: a new detection and upper limits. *Monthly Notices of the Royal Astronomical Society*, *468*(3), 2975–2983.

[Brice et al.(2021)] Brice, N., et al. (2021). Super-eddington emission from accreting, highly magnetized neutron stars with a multipolar magnetic field. *Monthly Notices of the Royal Astronomical Society*, *504*(1), 701–715.

[Carpano et al.(2005)] Carpano, S., et al. (2005). X-ray properties of ngc 300-i. global properties of x-ray point sources and their optical counterparts. *Astronomy & Astrophysics*, *443*(1), 103–114.

[Carpano et al.(2007)] Carpano, S., et al. (2007). A wolf-rayet/black-hole x-ray binary candidate in ngc 300. *Astronomy & Astrophysics*, *461*(1), L9–L12.

[Carpano et al.(2018)] Carpano, S., et al. (2018). Discovery of pulsations from ngc 300 ulx1 and its fast period evolution. *Monthly Notices of the Royal Astronomical Society: Letters*, *476*(1), L45–L49.

[Castillo et al.(2020)] Castillo, G. R., et al. (2020). Discovery of a 2.8 s pulsar in a 2 day orbit high-mass x-ray binary powering the ultraluminous x-ray source ulx-7 in m51. *The Astrophysical Journal*, *895*(1), 60.

[Colbert & Ptak(2002)] Colbert, E., & Ptak, A. (2002). A catalog of candidate intermediate-luminosity x-ray objects. *The Astrophysical Journal Supplement Series*, *143*(1), 25.

[Colbert & Mushotzky(1999)] Colbert, E. J., & Mushotzky, R. F. (1999). The nature of accreting black holes in nearby galaxy nuclei. *The Astrophysical Journal*, *519*(1), 89.

[Colbert et al.(2004)] Colbert, E. J., et al. (2004). Old and young x-ray point source populations in nearby galaxies. *The Astrophysical Journal*, *602*(1), 231.

[Dall'Osso et al.(2016)] Dall'Osso, S., et al. (2016). The accretion regimes of a highly magnetized ns: the unique case of nustar j095551+ 6940.8. *Monthly Notices of the Royal Astronomical Society*, *457*(3), 3076–3083.

[Fabbiano(1989)] Fabbiano, G. (1989). X rays from normal galaxies. *Annual review of astronomy and astrophysics*, *27*, 87–138.

[Fabrika(1997)] Fabrika, S. (1997). The supercritical accretion disk of ss 433. *Astrophysics and space science*, *252*(1), 439–450.

[Fabrika(2006)] Fabrika, S. (2006). The jets and and supercritical accretion disk in ss433. *arXiv preprint astro-ph/0603390*.

[Fabrika & Mescheryakov(2001)] Fabrika, S., & Mescheryakov, A. (2001). Face-on ss 433 stars as a possible new type of extragalactic x-ray sources. In *Symposium-International Astronomical Union*, vol. 205, (pp. 268–269). Cambridge University Press.

[Feng & Kaaret(2005)] Feng, H., & Kaaret, P. (2005). Xmm-newton observations of ultraluminous x-ray sources in nearby galaxies. *The Astrophysical Journal*, *633*(2), 1052.

[Feng & Kaaret(2006)] Feng, H., & Kaaret, P. (2006). A comparison of ultraluminous x-ray sources in ngc 1399 and the antennae galaxies (ngc 4038/4039). *The Astrophysical Journal*, *653*(1), 536.

[Feng & Kaaret(2007a)] Feng, H., & Kaaret, P. (2007a). Origin of the x-ray quasi-periodic oscillations and identification of a transient ultraluminous x-ray source in m82. *The Astrophysical Journal*, *668*(2), 941.

[Feng & Kaaret(2007b)] Feng, H., & Kaaret, P. (2007b). Spectral evolution of ngc 1313 x-2: Evidence against the cool disk model. *The Astrophysical Journal*, *660*(2), L113.

[Feng & Kaaret(2009)] Feng, H., & Kaaret, P. (2009). Spectral states and evolution of ultraluminous x-ray sources. *The Astrophysical Journal*, *696*(2), 1712.

[Foschini et al.(2002)] Foschini, L., et al. (2002). Xmm–newton observations of ultraluminous x–ray sources in nearby galaxies. *Astronomy & Astrophysics*, *392*(3), 817–825.

[Frank et al.(2002)] Frank, J., et al. (2002). *Accretion power in astrophysics*. Cambridge university press.

[Fürst et al.(2016)] Fürst, F., et al. (2016). Discovery of coherent pulsations from the ultraluminous x-ray source ngc 7793 p13. *The Astrophysical Journal Letters*, *831*(2), L14.

[Georganopoulos et al.(2002)] Georganopoulos, M., et al. (2002). External compton emission from relativistic jets in galactic black hole candidates and ultraluminous x-ray sources. *Astronomy & Astrophysics*, *388*(2), L25–L28.

[Ghosh & Lamb(1978)] Ghosh, P., & Lamb, F. (1978). Disk accretion by magnetic neutron stars. *The Astrophysical Journal*, *223*, L83–L87.

[Ghosh & Lamb(1979)] Ghosh, P., & Lamb, F. (1979). Accretion by rotating magnetic neutron stars. iii-accretion torques and period changes in pulsating x-ray sources. *The Astrophysical Journal*, *234*, 296–316.

[Gieren et al.(2005)] Gieren, W., et al. (2005). The araucaria project: Near-infrared photometry of cepheid variables in the sculptor galaxy ngc 300. *The Astrophysical Journal*, *628*(2), 695.

[Gierliński & Done(2004)] Gierliński, M., & Done, C. (2004). Black hole accretion discs: reality confronts theory. *Monthly Notices of the Royal Astronomical Society*, *347*(3), 885–894.

[Gilfanov(2004)] Gilfanov, M. (2004). X-ray binaries and ultra-luminoius x-ray sources in nearby and distant galaxies. *Progress of Theoretical Physics Supplement*, *155*, 49–58.

[Gladstone et al.(2009)] Gladstone, J. C., et al. (2009). The ultraluminous state. *Monthly Notices of the Royal Astronomical Society*, *397*(4), 1836–1851.

[Grimm et al.(2003)Grimm, Gilfanov, & Sunyaev] Grimm, H.-J., Gilfanov, M., & Sunyaev, R. (2003). High-mass x-ray binaries as a star formation rate indicator in distant galaxies. *Monthly Notices of the Royal Astronomical Society*, *339*(3), 793–809.

[Grisé et al.(2008)] Grisé, F., et al. (2008). The ultraluminous x-ray source ngc 1313 x-2-its optical counterpart and environment. *Astronomy & Astrophysics*, *486*(1), 151–163.

[Harding & Lai(2006)] Harding, A. K., & Lai, D. (2006). Physics of strongly magnetized neutron stars. *Reports on Progress in Physics*, *69*(9), 2631.

[Harrison et al.(2013)] Harrison, F. A., et al. (2013). The nuclear spectroscopic telescope array (nustar) high-energy x-ray mission. *The Astrophysical Journal*, *770*(2), 103.

[Hartle(2003)] Hartle, J. B. (2003). Gravity: an introduction to einstein's general relativity.

[Helfand(1984)] Helfand, D. J. (1984). Endpoints of stellar evolution: X-ray surveys of the local group. *Publications of the Astronomical Society of the Pacific*, *96*(586), 913.

[Humphrey et al.(2003)] Humphrey, P., et al. (2003). Ultraluminous x-ray source populations in normal galaxies: a preliminary survey with chandra. *Monthly Notices of the Royal Astronomical Society*, *344*(1), 134–148.

[Immler et al.(2010)] Immler, S., et al. (2010). Swift xrt detection of supernova 2010da in x-rays. *The Astronomer's Telegram*, *2639*, 1.

[Irwin et al.(2003)] Irwin, J. A., et al. (2003). X-ray spectral properties of low-mass x-ray binaries in nearby galaxies. *The Astrophysical Journal*, *587*(1), 356.

[Israel et al.(2017)] Israel, G. L., et al. (2017). An accreting pulsar with extreme properties drives an ultraluminous x-ray source in ngc 5907. *Science*, *355*(6327), 817–819.

[Kaaret et al.(2001)] Kaaret, P., et al. (2001). Chandra high-resolution camera observations of the luminous x-ray source in the starburst galaxy m82. *Monthly Notices of the Royal Astronomical Society*, *321*(2), L29–L32.

[Kajava & Poutanen(2009)] Kajava, J. J., & Poutanen, J. (2009). Spectral variability of ultraluminous x-ray sources. *Monthly Notices of the Royal Astronomical Society*, *398*(3), 1450–1460.

[Kalogera et al.(2004)] Kalogera, V., et al. (2004). An observational diagnostic for ultraluminous x-ray sources. *The Astrophysical Journal*, *603*(1), L41.

[Kaminker et al.(1982)] Kaminker, A., et al. (1982). Radiation from a strongly-magnetized plasma: The case of predominant scattering. *Astrophysics and Space Science*, *86*(2), 249–297.

[Kilgard et al.(2002)] Kilgard, R., et al. (2002). A minisurvey of x-ray point sources in starburst and nonstarburst galaxies. *The Astrophysical Journal*, *573*(1), 138.

[Kim & Fabbiano(2010)] Kim, D.-W., & Fabbiano, G. (2010). X-ray properties of young early-type galaxies. i. x-ray luminosity function of low-mass x-ray binaries. *The Astrophysical Journal*, *721*(2), 1523.

[King et al.(2001)] King, A. R., et al. (2001). Ultraluminous x-ray sources in external galaxies. *The Astrophysical Journal*, *552*(2), L109.

[Körding et al.(2002)] Körding, et al. (2002). Population x: Are the super-eddington x-ray sources beamed jets in microblazars or intermediate mass black holes? *Astronomy & Astrophysics*, *382*(3), L13–L16.

[Kubota et al.(2001)] Kubota, A., et al. (2001). Observational evidence for strong disk comptonization in gro j1655–40. *The Astrophysical Journal*, *560*(2), L147.

[Kubota et al.(2002)] Kubota, A., et al. (2002). Another interpretation of the power-law-type spectrum of an ultraluminous compact x-ray source in ic 342. *Monthly Notices of the Royal Astronomical Society*, *337*(3), L11–L15.

[Lau et al.(2016)] Lau, R. M., et al. (2016). Rising from the ashes: Mid-infrared re-brightening of the impostor sn 2010da in ngc 300. *The Astrophysical Journal*, *830*(2), 142.

[Long et al.(1983)] Long, et al. (1983). X-ray emission from normal galaxies. *Accretion-Driven Stellar X-Ray Sources*, (pp. 117–146).

[Lyubarskii & Syunyaev(1988)] Lyubarskii, Y. E., & Syunyaev, R. (1988). Accretion column structure. *Soviet Astronomy Letters*, *14*, 390.

[Madau & Rees(2001)] Madau, P., & Rees, M. J. (2001). Massive black holes as population iii remnants. *The Astrophysical Journal*, *551*(1), L27.

[Makishima et al.(2000)] Makishima, K., et al. (2000). The nature of ultraluminous compact x-ray sources in nearby spiral galaxies. *The Astrophysical Journal*, *535*(2), 632.

[McClintock & Remillard(2006)] McClintock, J. E., & Remillard, R. A. (2006). Black hole binaries. *Compact stellar X-ray sources*, *39*, 157–213.

[Middleton et al.(2015)] Middleton, M. J., et al. (2015). A spectral-timing model for ulxs in the supercritical regime. *Monthly Notices of the Royal Astronomical Society*, *447*(4), 3243–3263.

[Miller et al.(2013)] Miller, J., et al. (2013). Revisiting putative cool accretion disks in ultraluminous x-ray sources. *The Astrophysical Journal Letters*, *776*(2), L36.

[Mineo et al.(2012)] Mineo, S., et al. (2012). X-ray emission from star-forming galaxies–i. high-mass x-ray binaries. *Monthly Notices of the Royal Astronomical Society*, *419*(3), 2095–2115.

[Monard(2010)] Monard, L. (2010). 2010da in ngc 300. *Central Bureau Electronic Telegrams*, *2292*, 1.

[Mushtukov et al.(2015)] Mushtukov, A. A., et al. (2015). On the maximum accretion luminosity of magnetized neutron stars: connecting x-ray pulsars and ultraluminous x-ray sources. *Monthly Notices of the Royal Astronomical Society*, *454*(3), 2539–2548.

[Mushtukov et al.(2017)] Mushtukov, A. A., et al. (2017). Optically thick envelopes around ulxs powered by accreating neutron stars. *Monthly Notices of the Royal Astronomical Society*, *467*(1), 1202–1208.

[Pintore & Zampieri(2012)] Pintore, F., & Zampieri, L. (2012). X-ray spectral states and metallicity in the ultraluminous x-ray sources ngc 1313 x-1 and x-2. *Monthly Notices of the Royal Astronomical Society*, *420*(2), 1107–1114.

[Poutanen et al.(2007)] Poutanen, J., et al. (2007). Supercritically accreting stellar mass black holes as ultraluminous x-ray sources. *Monthly Notices of the Royal Astronomical Society*, *377*(3), 1187–1194.

[Read & Pietsch(2001)] Read, A., & Pietsch, W. (2001). X-ray emission from the sculptor galaxy ngc 300. *Astronomy & Astrophysics*, *373*(2), 473–484.

[Remillard & McClintock(2006)] Remillard, R. A., & McClintock, J. E. (2006). X-ray properties of black-hole binaries. *arXiv preprint astro-ph/0606352*.

[Roberts & Warwick(2000)] Roberts, T., & Warwick, R. (2000). A rosat high resolution imager survey of bright nearby galaxies. *Monthly Notices of the Royal Astronomical Society*, *315*(1), 98–114.

[Roberts et al.(2005)] Roberts, T., et al. (2005). Xmm—newton epic observations of the ultraluminous x-ray source ngc 5204 x-1. *Monthly Notices of the Royal Astronomical Society*, *357*(4), 1363–1369.

[Roberts et al.(2011)] Roberts, T., et al. (2011). (no) dynamical constraints on the mass of the black hole in two ulxs. *Astronomische Nachrichten*, *332*(4), 398–401.

[Sathyaprakash et al.(2019)] Sathyaprakash, R., et al. (2019). The discovery of weak coherent pulsations in the ultraluminous x-ray source ngc 1313 x-2. *Monthly Notices of the Royal Astronomical Society: Letters*, *488*(1), L35–L40.

[Stobbart et al.(2006)] Stobbart, A.-M., et al. (2006). Xmm–newton observations of the brightest ultraluminous x-ray sources. *Monthly Notices of the Royal Astronomical Society*, *368*(1), 397–413.

[Strüder et al.(2001)] Strüder, L., et al. (2001). The european photon imaging camera on xmm-newton: the pn-ccd camera. *Astronomy & Astrophysics*, *365*(1), L18–L26.

[Sutton et al.(2013)] Sutton, et al. (2013). The ultraluminous state revisited: fractional variability and spectral shape as diagnostics of super-eddington accretion. *Monthly Notices of the Royal Astronomical Society*, *435*(2), 1758–1775.

[Swartz et al.(2004)] Swartz, D. A., et al. (2004). The ultraluminous x-ray source population from the chandra archive of galaxies. *The Astrophysical Journal Supplement Series*, *154*(2), 519.

[Swartz et al.(2011)] Swartz, D. A., et al. (2011). A complete sample of ultraluminous x-ray source host galaxies. *The Astrophysical Journal*, *741*(1), 49.

[Taverna & Turolla(2017)] Taverna, R., & Turolla, R. (2017). On the spectrum and polarization of magnetar flare emission. *Monthly Notices of the Royal Astronomical Society*, *469*(3), 3610–3628.

[Taverna et al.(2015)] Taverna, R., et al. (2015). Polarization of neutron star surface emission: a systematic analysis. *Monthly Notices of the Royal Astronomical Society*, *454*(3), 3254–3266.

[Tiengo et al.(2013)] Tiengo, A., et al. (2013). A variable absorption feature in the x-ray spectrum of a magnetar. *Nature*, *500*(7462), 312–314.

[Treves et al.(2000)] Treves, A., et al. (2000). Isolated neutron stars: accretors and coolers. *Publications of the Astronomical Society of the Pacific*, *112*(769), 297.

[Tully et al.(2013)] Tully, R. B., et al. (2013). Cosmicflows-2: the data. *The Astronomical Journal*, *146*(4), 86.

[Turner et al.(2001)] Turner, M. J., et al. (2001). The european photon imaging camera on xmm-newton: the mos cameras. *Astronomy & Astrophysics*, *365*(1), L27–L35.

[Urquhart & Soria(2016)] Urquhart, R., & Soria, R. (2016). Optically thick outflows in ultraluminous supersoft sources. *Monthly Notices of the Royal Astronomical Society*, *456*(2), 1859–1880.

[Van Der Marel(2004)] Van Der Marel, R. P. (2004). in the universe: a review of formation theories and observational constraints. *Coevolution of Black Holes and Galaxies: Volume 1, Carnegie Observatories Astrophysics Series*, *1*, 37.

[Villar et al.(2016)] Villar, V. A., et al. (2016). The intermediate luminosity optical transient sn 2010da: The progenitor, eruption, and aftermath of a peculiar supergiant high-mass x-ray binary. *The Astrophysical Journal*, *830*(1), 11.

[Wang(1999)] Wang, Q. D. (1999). Detection of x-ray-emitting hypernova remnants in m101. *The Astrophysical Journal*, *517*(1), L27.

[Zane & Turolla(2006)] Zane, S., & Turolla, R. (2006). Unveiling the thermal and magnetic map of neutron star surfaces though their x-ray emission: method and light-curve analysis. *Monthly Notices of the Royal Astronomical Society*, *366*(3), 727–738.

[Zane et al.(2000)] Zane, S., et al. (2000). Magnetized atmospheres around neutron stars accreting at low rates. *The Astrophysical Journal*, *537*(1), 387.